THE
PHYSICAL
SOCIETY

MEMOIRS

OF THE

COLLEGE OF SCIENCE

UNIVERSITY OF KYOTO

SERIES A

VOL. XXIX, No. 3

September, 1961

KYOTO

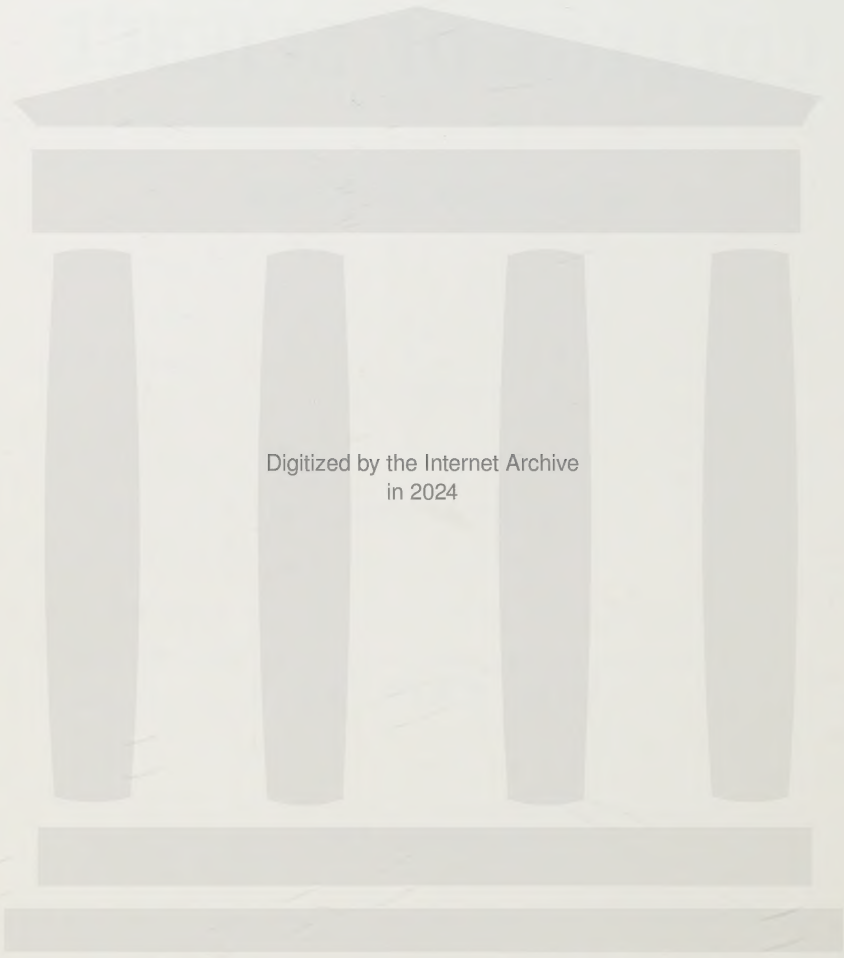
Digitized by the Internet Archive
in 2024

https://archive.org/details/memoirs-faculty-science-kyoto-phys-astro-geophys-chem_1961-09_29_3

Memoirs of the College of Science, University of Kyoto, Series A,
Vol. XXIX, No. 3, Article 1, 1961.

TEMPERATURE DEPENDENCE OF SPIN LATTICE RELAXATION TIME OF Cl^{35} IN PURE QUADRUPOLE RESONANCE*

BY

Akira HIRAI

(Received March 31, 1960)

ABSTRACT

The spin lattice relaxation time (T_1) of Cl^{35} nuclei between quadrupole resonance levels in para-dichlorobenzene and in sodium chlorate was measured at several temperatures by the use of the 90°–90° pulse method. To analyse the obtained data, two approaches were undertaken: the first was done by following Bayer's theory and the second by Van Kranendonk's and Yoshida-Moriya's theories. Although the approaches were bold and rough, and detailed interpretations were not possible, yet both gave fairly satisfactory explanation for the obtained data of temperature dependence of T_1. An experiment is proposed which would decide which approach is better.

1. Introduction

The quadrupolar relaxation is one of the most important relaxation mechanisms for nucleus whose spin number is greater than 1/2. A few systematic investigations have been carried out both theoretically (**1, 2, 3, 4**) and experimentally (**5, 6**) on quadrupolar relaxation in nuclear magnetic resonance (NMR). In pure quadrupole resonance (PQR), the relaxation mechanism is almost entirely quadrupolar. As to the quadrupolar relaxation in molecular crystal in PQR, Bayer's theory (**7**) is the only one as far as we know. Although some workers have measured T_1 in PQR (**8, 9, 10**), any systematic investigations, particularly on the temperature dependence of T_1 in PQR, which are the most convenient ways to study the mechanism, have not yet been made experimentally**. We have therefore measured the temperature dependence of T_1 of Cl^{35} in PQR on para-dichlorobenzene (p-$Cl_2\phi$) and on sodium chlorate ($NaClO_3$), which are standard samples in PQR, the former being a molecular crystal and the latter an ionic. To analyse

* A part of this paper has been published as a short note in J. Phys. Soc. Japan **15** (1960), 201.

** At the beginning of March, Dr. Tanttila kindly communicated that he and his co-workers made experiments of the same kind as ours, and that they analysed the obtained data following Chang's theory, of which any publication has not been accessible. The author expresses his thanks to Dr. Tanttila for sending a copy of the following article before publication.
P. A. Bender, D. A. Jennings and W. H. Tanttila: J. Chem. Phys. (in press).

the obtained data, two approaches were undertaken: the first was to follow directly Bayer's theory and the second was to apply Van Kranendonk's theory (**1**), Yoshida-Moriya's theory (**2**) and Kondo-Yamashita's theory (**3**) to our case, which were originally concerned with the quadrupolar relaxation in NMR in ionic crystals, particularly of NaCl and CsCl type. Though there is Khutsishvilli's theory (**4**) for the quadrupolar relaxation in NMR, which predicts $T_1 \propto T^{-4}$ at high temperatures, it does not fit some experiments in NMR (**6**) nor our results, so we shall not consider this theory. In the following sections, the experimental results and the analysis will be given.

2. Experimental method and results

In order to measure T_1 of Cl^{35} in PQR, a pulsed PQR apparatus operating near 30 Mc/sec was constructed. The 90°–90° pulse method was employed. The apparatus and the procedures were essentially the same as those we used for measuring T_1 in NMR (**11**). A few modifications were made as described below. (1) The pulsed oscillation was made to be initially at the low power level, and then amplified to the desired power level, for the purpose of increasing the stability of the apparatus. (2) The pulsed rf power was fed to the sample coil from a low impedance source, so that the sample coil was easily immersed in a refrigerant, while the input to the nuclear signal receiver was of high impedance type as before. (3) The straight nuclear signal receiver was replaced by the superheterodyne system, so that the apparatus was suitable for following the change of PQR resonance frequency (ν) by the change of sample and of temperature. The intermediate frequency was chosen to be 13.5 Mc/sec, and the frequency of local oscillator to be on the higher frequency side to avoid the direct power leakage of the local oscillation to the detector. Only the modified parts of the apparatus are shown schematically in Fig. 1.

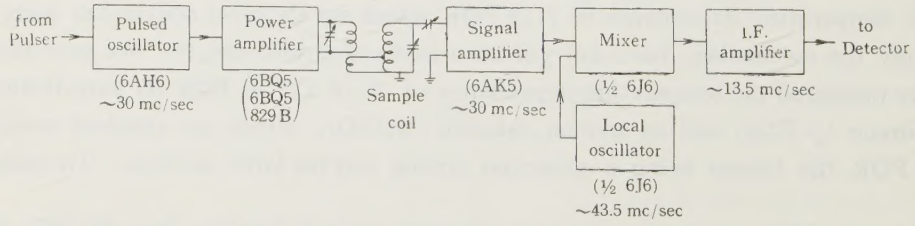

Fig. 1. Block diagram of only the modified parts of our experimental apparatus. For other parts, see reference **11**.

The sample used (p-$Cl_2\phi$ and $NaClO_3$) were polycrystals. The value of T_1 in PQR, which is of course determined by the quadrupolar relaxation, is independent

of whether the sample is single crystal or polycrystal, at least in our temperature region (**5**, **10**).

Because of the temperature dependence of PQR resonance frequency, we must use a cryostat which has the following characteristics: (1) The temperature inside the cryostat must be constant within about $\pm 0.1°K$ during one measurement, which takes about half an hour for a long T_1. (2) The temperature gradient through the sample must be smaller than about $\pm 0.1°K$. Up to the present, however, the author has not obtained such a cryostat, and therefore the sample was immersed in an appropriate refrigerant and T_1 was measured only at several temperatures.

The data thus obtained are tabulated in Table I below.

Table I. Measured values of T_1 of Cl^{35} at several temperatures.

T (°K)	T_1 (m sec) (on p-Cl_2 ϕ)	T (°K)	T_1 (m sec) (on $NaClO_3$)
77	560±50	77	1900±100
90	450±40	90	1450± 70
195	60± 5	195	137± 7
271	27± 3	286	50± 4
292	22± 2		
300	19± 2		

3. First approach—Analysis by Bayer's theory

The obtained data of T_1 on p-$Cl_2\phi$ sample was first analysed by Bayer's theory. This theory is based on the model that the energy of spin system relaxes to the energy of the torsional vibration of a molecule, and that the torsional vibration itself is disturbed by other motions in the crystal. The results of analysis were already reported (**12**), so that they will not be reproduced here in detail. We could not apply Bayer's theory to $NaClO_3$ sample, however, because the information necessary for analysis about the torsional vibrational frequency of this sample was lacking. The comparison between the theoretical curve and the experimental points is shown in Fig. 2 (cf. reference **12**), where one adjustable parameter, i.e. the average life-time in the excited states of the torsional vibration, was assumed to be 1.23×10^{-11} sec.

To sum up, Bayer's theory has the following characteristic features: (1) It stands on a relatively simple model and has only one adjustable parameter. (2) It explains the general feature of the temperature dependence of T_1. (3) It gives a reasonable value for the average life-time in the excited states of the torsional vibration. (4) In addition, it predicts the temperature dependence of the PQR

resonance frequency, and this prediction was almost correct for many substances, as already examined by many workers (**13**).

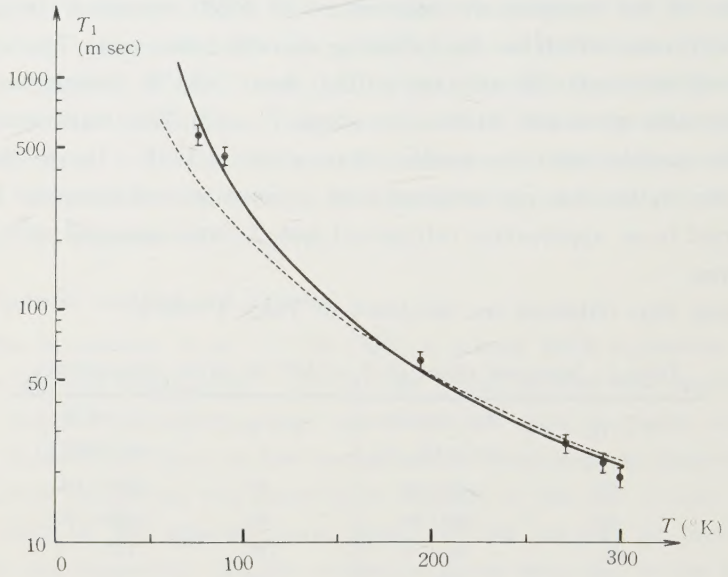

Fig. 2. Experimental points and the results of the two approaches for p-$Cl_2\phi$ sample. The dotted curve is due to the first approach (the same figure as that in reference **12**), and the solid-line curve to the second.

When we fix our attention on the form of the temperature dependence of T_1 but not on its absolute value, T_1 given by Bayer's theory can be expressed, to good accuracy, as $T_1 \propto T^{-2}$ in our temperature range. As we can easily see from Fig. 2, the experimental curve for the temperature dependence of T_1 is steeper than the theoretical one. It was impossible to explain this discrepancy by a simple modification of Bayer's theory, because the theory is too bold in its assumption to be modified easily. Thus, another approach will be considered in the next section.

4. Second approach—Analysis by Van Kranendonk's theory

As a second approach, we shall make use of Van Kranendonk's theory which was originally concerned with the quadrupolar relaxation in ionic crystals in NMR. Detailed calculation, particularly for the temperature dependence of T_1, was carried out for the NaCl type ionic crystal. Both Yoshida-Moriya's theory and Kondo-Yamashita's theory are modifications of this Van Kranendonk's theory.

In the detailed calculation, these three theories stand on the two fundamental assumptions: (1) The relaxation takes place as two-phonon Raman process,

namely, one phonon of the frequency ν_p is absorbed and another phonon of the frequency $\nu_p+\nu$ is emitted, when the energy of spin system relaxes to the energy of the lattice vibration. (2) The spectrum of phonon system (lattice vibration) is assumed to be of acoustical Debye type.

In Van Kranendonk's theory, it is assumed that the time-varying electric field gradient causing the relaxation in spin system is caused by the vibration of oppositely charged nearest neighbour ions. In Yoshida-Moriya's theory and in Kondo-Yamashita's theory, it is assumed to be caused respectively by the modulation of covalency and that of overlap by lattice vibration. But, the temperature dependence of T_1 is of the same form in all these theories, so far as they stand on the above two assumptions, and the concrete expression for the temperature dependence of T_1 is given by Van Kranendonk's paper.

There are many questions about the application of these theories to the relaxation phenomena in PQR, for it is natural to consider that in PQR the energy of spin system relaxes to the energy of the normal vibration modes of a molecule (p-$Cl_2\phi$) or of an ion (ClO_3^- ion) and then relaxes to the energy of lattice vibration. But, at present, such elegant theories as taking the above consideration into account are not available, so we try to analyse our data by Van Kranendonk's theory. In this case, however, we follow Yoshida-Moriya's or Kondo-Yamashita's theory for the interpretation of the time-varying electric field gradient. At any rate, if we accept the above two assumptions, we do not think it so unnatural to apply these theories to T_1 in PQR, *at least for the temperature dependence*. Of the above assumptions, the first assumption (1) would be plausible in our case. But there remain many questions about the second assumption (2). Plausible excuses to approve this second assumption are that though there would be many complicated vibration modes in samples used for PQR, these vibration modes are averaged to an acoustical Debye mode and that the value of T_1 is the quantity which is averaged over all the lattice vibration modes, and, in general, such averaged quantities are insensitive to the detail of the lattice vibration spectrum (**14**).

In these theories, the transition probability from m state to $(m+\mu)$ state is given by

$$P(m,\ m+\mu) = C'|Q_{\mu,m}|^2 T^{*2} E(T^*) E_\mu(\infty)\ ,$$

where C' is considered to be an adjustable parameter (which includes the Sternheimer antishielding coefficient in Van Kranendonk's theory and the degree of covalency in Yoshida-Moriya's theory, $T^*=T/T_D$ (T_D being the Debye temperature), $Q_{\mu,m}$ is the matrix element for the quadrupole operator between states m and $m+\mu$, $E(T^*)$ is a numerical function given by Van Kranendonk, and $E_\mu(\infty)$

is a numerical constant of the order of 100 given by Van Kranendonk.

In our case, there are only two energy levels, where T_1 is given by

$$T_1 = \left[2\left\{P\left(\frac{1}{2}, \frac{3}{2}\right) + P\left(\frac{1}{2}, -\frac{3}{2}\right)\right\}\right]^{-1}.$$

So we assume roughly that, at least concerned with the temperature dependence, T_1 is given by

$$T_1 = \frac{C}{E(T^*)T^{*2}},$$

where both C and T_D are adjustable parameters.

Using the above formulas, we can determine T_D and then C from the observed data, obtaining

$$T_D = 280°\mathrm{K}, \quad C = 0.024 \text{ sec for } p\text{–}Cl_2\phi\ ,$$
$$T_D = 380°\mathrm{K}, \quad C = 0.028 \text{ sec for } NaClO_3\ .$$

The curve thus obtained and the experimental points are shown in Figs. 2 and 3. In the determination of T_D and C, the values of T_D are not so critical and the deviation of about $\pm 10\%$ from the above value does not change the general feature of the curve, when a suitable change of the value of C is made.

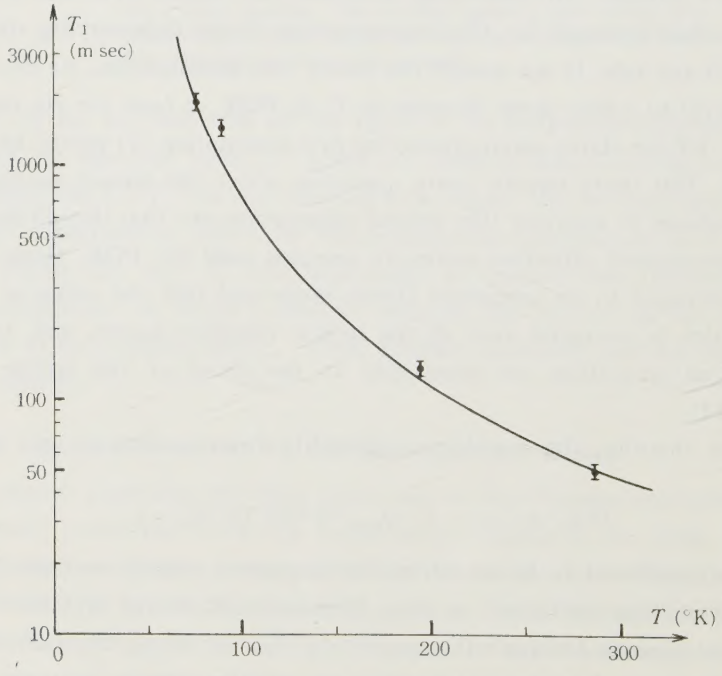

Fig. 3. Experimental points and the results of the second approach for $NaClO_3$ sample.

This approach, which has two adjustable parameters (T_D and C), gives more satisfactory agreement than the first approach, but the two deduced values of adjustable parameters could hardly be related to the other physical quantities. For T_D, we might consider that among many vibrational modes in the crystal, the modes with frequencies smaller than ν_D ($=kT_D/h$), which is equal to 194 cm^{-1} for p-$Cl_2\phi$ and to 264 cm^{-1} for $NaClO_3$, are effective in the quadrupolar relaxation. About C, we have nothing to say. Rather we should consider the above formulas semi-empirical.

At any rate, Bayer's theory gives $T_1 \propto T^{-2}$ in our temperature range, while Van Kranendonk's theory gives $T_1 \propto T^{-2}$ in the temperature range defined by $E(T^*) \approx 1$, and Van Kranendonk's function $E(T^*)$ describes the deviation from the T^{-2}-law for $T < T_D$. And this deviation is favourably compared with experiments.

5. Discussions

Since the mechanism of quadrupolar relaxation in PQR is very complicated, that is, since we must consider the electronic structure of the sample, while we have only to consider the magnetic moment in the nuclear magnetic relaxation, it is very difficult to construct an excellent theory to give a satisfactory agreement with the experimental data. In the preceding sections, the obtained data were analysed by two different theories, each of which corresponds respectively to Einstein's and Debye's model in the theory of specific heat. Of course, we think these analyses are only of rough approximations, because in the first approach the process of calculation was too simplified and in the second the model on which the theories stand was too simple for the relaxation phenomena in PQR. But, both explained the general feature of the experimental data, though detailed interpretations were not possible. This would be due to the fact that the value of T_1 is insensitive to the detail of the lattice vibration spectrum. In fact, the temperature dependences of T_1 by both Bayer's and Van Kranendonk's theories are nearly the same, that is, $T_1 \propto T^{-2}$ at high temperatures, and also it should be emphasized that the temperature dependences of T_1 for both samples (p-$Cl_2\phi$ and $NaClO_3$) were nearly the same.

However, it is interesting to clarify, by experiments, which approach is better. Though there might be many kinds of experiments to solve this question, the following is proposed as an example. In Bayer's theory, the $|\Delta m| = 2$ transition is more effective by the order of one or two than the $|\Delta m| = 1$ transition in relaxation mechanism, but in Van Kranendonk's theory, these are comparable in the order. We shall try to examine this point.

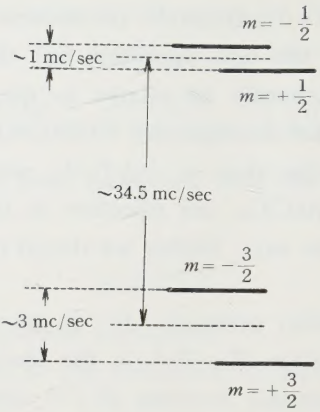

Fig. 4. Energy level diagram in the proposed experiment, where external magnetic field (about 2,500 gauss) is parallel to the symmetry axis of the electric field gradient at Cl^{35} nuclei in p-$Cl_2\phi$ sample.

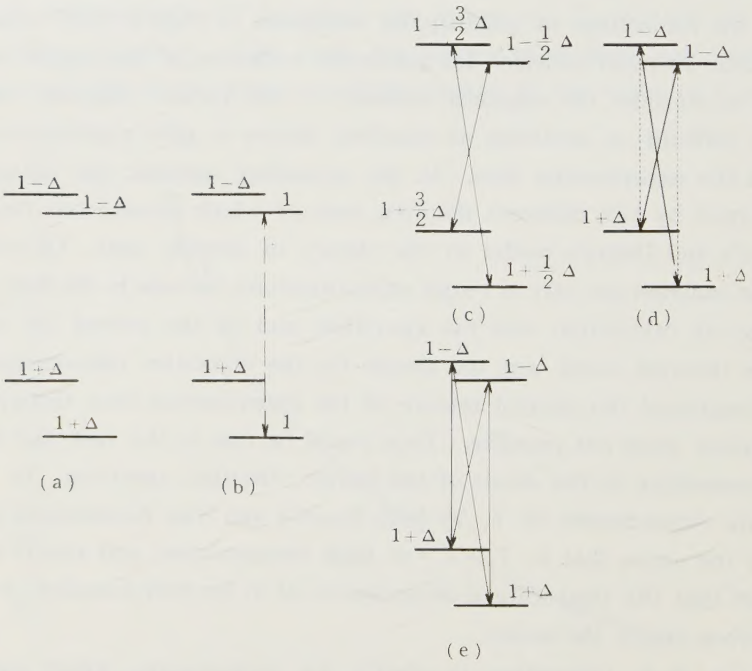

Fig. 5. Relative spin populations at each level, illustrating the proposed experiment ($\Delta=h\nu/2kT$), (a) at thermal equilibrium; (b) just after the first 90° pulse applied between 1/2 and 3/2 levels; (c) after a time interval of the order of T_1, according to Bayer's theory; (d) after a time interval of the order of 100 T_1, according to Bayer's theory; (e) after a time interval of the order of T_1, according to Van Kranendonk's theory. The difference between (c) and (e) would be easily detected.

Take a single crystal sample, in which the electric field gradient at Cl nuclei is, exactly or nearly, axially symmetric (e.g. p-$Cl_2\phi$), and place it in a magnetic field (e.g. of about a few thousand gauss), whose direction is parallel to the symmetry axis of the electric field gradient. In this case, $\pm 1/2$ levels are not mixed. The energy levels are shown schematically in Fig. 4. Here, for simplicity, the effect of the existence of symmetry axes of different directions in a single crystal (there being two in the case of p-$Cl_2\phi$ (**15**)) is neglected.

We pay attention only to the population difference between 1/2 and 3/2 levels. A 90° pulse (circularly polarized rf pulse inducing only $\Delta m = -1$ transition being favourable) is applied between 3/2 and 1/2 levels. After a time interval τ, the population difference between 1 2 and 3/2 levels is searched for by a second 90° pulse. Then, (1) according to Bayer's theory, the population difference would approach to half of the original value with a time constant of the order of T_1, which is the spin lattice relaxation time measured in our experiments, and then it would approach to the original value with a time constant one hundred times as large as T_1 in the order, and (2) according to Van Kranendonk's theory, it would approach to the original value with a time constant of the order of T_1, though the approach would not be of a single exponential type in this case (cf. Fig. 5).

It is considered that this difference might be easily detected experimentally. Such an experiment may become complicated owing to the situations that there are some different directions of the symmetry axis of the electric field gradient in a single crystal, but it would not be difficult to pick up the desired resonance by using a suitable sample and an appropriate value of magnetic field.

Acknowledgments

The author would like to express his sincere thanks to Prof. I. Takahashi and Prof. T. Hashi for their continual guidance and discussions. His thanks are also due to Mr. K. Sugibuchi and other members in our laboratory for their assistances, and to Dr. K. Yoshida and Dr. K. Mochizuki at Osaka University, and Prof. K. Tomita and members of his laboratory for their discussions.

REFERENCES

1. J. Van Kranendonk: Physica **20** (1954), 781.
2. K. Yoshida and T. Moriya: J. Phys. Soc. Japan **11** (1956), 33.
3. J. Kondo and J. Yamashita: J. Phys. Chem. Solids **10** (1959), 285.
4. G. R. Khutsishvilli: Sov. Phys. JETP **4** (1957), 382.
5. C. V. Briscoe and C. F. Squire: Phys. Rev. **112** (1958), 1540.
6. R. L. Mieher: Phys. Rev. Letters **4** (1960), 57.
7. H. Bayer: ZS f. Phys. **130** (1951), 227.
8. W. G. Proctor and W. H. Tanttila: Phys. Rev. **101** (1956), 1757.

9. D. E. Woessner and H. S. Gutowsky: J. Chem. Phys. **27** (1957), 1072.
10. T. Hashi: J. Phys. Soc. Japan **13** (1958), 911.
11. T. Hashi, A. Hirai, M. Sasaki and T. Kawai: Memoirs of the College of Science, Univ. of Kyoto, A **29** (1959), 205.
12. A. Hirai: J. Phys. Soc. Japan **15** (1960), 201.
13. For example, see, T. P. Das and E. L. Hahn: *Nuclear Quadrupole Resonance Spectroscopy* (Academic Press, New York, 1958), p. 39 ff.
14. M. Born and K. Huang: *Dynamical Theory of Crystal Lattice* (Clarendon Press, Oxford, 1954).
15. U. Croatto, S. Bezzi and E. Bua: Acta Cryst. **5** (1952), 201; also, reference **13**, p. 114 ff.

Memoirs of the College of Science, University of Kyoto, Series A,
Vol. XXIX, No. 3, Article 2, 1961.

NUMERICAL DIFFERENTIAL CROSS SECTIONS OF THE (p, α) REACTIONS ON Al^{27}, Mn^{55} AND Co^{59}

BY

Hiroshi OGATA, Hidehiko ITOH, Yoshiko MASUDA, Kunio TAKAMATSU, Maumi KAWASHIMA, Akira MASAIKE and **Isao KUMABE**

(*Received September 15, 1960*)

We have measured the angular distributions of the reactions $Al^{27}(p, \alpha)Mg^{24}$, $Mn^{55}(p, \alpha)Cr^{52}$ and $Co^{59}(p, \alpha)Fe^{56}$ resulting in the ground and first excited states of the residual nuclei at 10.5～14.5 Mev, 7.6～12.9 Mev and 7.7～14.1 Mev, respectively. The results have been published in the Journal of the Physical Society of Japan **1**, **2** . The results were represented graphically but the numerical data were not. The numerical dada are, however, necessary for exact comparison with theoretical calculations and with experimental results at other laboratories.

Since some people required us the numerical data, and since the data obtained are rather numerous, we decided to submit these numerical data to this Memoirs.

The details of experimental procedures and discussions have been given in the original articles (**1**, **2**).

REFERENCES

1. H. Ogata, H. Itoh, Y. Masuda, K. Takamatsu, M. Kawashima, A. Masaike and I. Kumabe: J. Phys. Soc. Japan, **15** (1960), 1719.
2. H. Ogata, H. Itoh, Y. Masuda, K. Takamatsu, M. Kawashima, A. Masaike and I. Kumabe: J. Phys. Soc. Japan, **15** (1960), 1726.

Table I (i). Differential cross sections of the reaction $Al^{27}(p, \alpha_0)Mg^{24}$ resulting in the ground state of Mg^{24}.

$\left(\frac{d\sigma}{d\Omega}\right)_{c.m.}$ (μb/sterad)

$\theta_{c.m.}$ (deg) \ E_p (Mev)	10.65	10.83	10.99	11.11
21.4	298.6 (12.1)	546.4 (10.5)	613.6 (24.7)	433.5 (14.3)
32.1	198.3 (7.0)	525.5 (9.4)	536.2 (23.2)	317.6 (8.7)
42.7	171.6 (6.5)	439.0 (10.2)	392.7 (20.0)	214.8 (7.2)
53.2	137.7 (5.9)	396.3 (8.1)	388.1 (14.2)	274.7 (8.1)
63.6	152.4 (8.1)	306.5 (7.4)	470.2 (22.3)	348.6 (12.0)
73.9	200.6 (6.6)	214.9 (5.8)	492.5 (23.0)	346.9 (8.6)
84.1	236.9 (7.3)	160.7 (5.9)	476.1 (23.0)	255.1 (7.5)
94.2	197.7 (7.1)	125.8 (4.4)	458.1 (16.1)	352.3 (8.8)
104.1	277.7 (8.1)	180.0 (5.3)	389.5 (21.3)	434.6 (10.0)
113.9	279.9 (8.2)	158.8 (5.5)	404.0 (22.0)	454.4 (10.3)
123.6	303.1 (8.6)	159.4 (5.5)	332.6 (20.2)	375.7 (13.3)
133.2	324.9 (9.1)	197.6 (5.7)	294.4 (17.2)	231.8 (7.6)
142.7	322.7 (10.0)	260.7 (7.3)	329.4 (20.5)	206.2 (7.9)
152.1	294.8 (9.6)	352.7 (9.3)	268.2 (18.7)	159.4 (7.0)
161.4	244.9 (8.9)	498.7 (11.2)	207.0 (16.5)	206.8 (10.1)
170.7	274.3 (9.4)	652.7 (11.6)	125.6 (11.5)	227.3 (8.4)

E_p=mean incident proton energy at the center of target, in laboratory system.
In bracket, the probable error is given.

Table I (ii)

$\theta_{c.m.}$ (deg) \ E_p (Mev)	11.22	11.25	11.41	11.45
21.4	669.1 (14.5)	694.2 (13.4)	607.0 (13.5)	602.6 (13.7)
32.1	323.0 (9.0)	335.1 (8.7)	369.4 (9.2)	354.2 (9.1)
42.7	251.0 (7.6)	227.0 (5.7)	228.1 (5.3)	171.5 (6.4)
53.2	269.7 (8.0)	270.8 (8.0)	283.4 (8.2)	156.5 (6.2)
63.6	277.9 (9.7)	283.1 (8.8)	276.6 (9.3)	299.9 (10.0)
74.0	207.5 (7.5)	231.6 (7.6)	268.4 (8.1)	399.6 (10.1)
84.1	273.0 (8.3)	270.2 (6.5)	310.7 (8.8)	443.6 (10.8)
94.2	416.5 (10.4)	442.2 (10.7)	353.6 (9.5)	374.5 (10.0)
104.1	578.7 (12.4)	652.9 (13.2)	398.5 (10.2)	347.9 (10.0)
114.0	631.2 (13.1)	666.6 (13.5)	503.2 (11.7)	356.3 (10.0)
123.6	517.4 (12.0)	562.0 (12.3)	544.2 (12.2)	372.2 (10.3)
133.2	391.6 (10.5)	395.9 (10.6)	586.1 (12.7)	346.4 (10.1)
142.7	277.3 (9.0)	336.8 (9.9)	530.5 (12.4)	288.1 (9.3)
152.1	231.0 (8.2)	304.8 (9.5)	420.9 (11.1)	192.9 (7.7)
161.4	256.5 (8.7)	262.7 (8.8)	282.8 (9.1)	108.0 (5.8)
170.7	284.5 (9.2)	262.7 (8.9)	154.9 (6.7)	71.2 (4.7)

Table I (iii)

$\theta_{c.m.}$ (deg) \ E_p (Mev)	11.53	11.70	11.80	11.91
21.4	562.0 (10.6)	618.4 (14.6)	543.1 (13.7)	748.8 (15.8)
32.1	485.0 (10.7)	671.2 (15.5)	486.6 (13.0)	429.6 (10.7)
42.7	350.4 (9.5)	563.9 (14.3)	383.4 (11.7)	196.8 (8.5)
53.2	244.1 (8.0)	371.8 (11.7)	259.7 (9.5)	104.9 (6.3)
63.6	247.7 (7.3)	232.3 (8.4)	185.3 (7.6)	84.4 (5.0)
74.0	299.9 (8.7)	203.8 (7.9)	156.6 (7.0)	149.9 (7.0)
84.2	369.7 (10.0)	208.9 (8.3)	128.0 (6.4)	156.9 (7.2)
94.2	425.9 (11.0)	153.1 (7.2)	102.3 (5.7)	80.7 (5.3)
104.1	440.8 (11.4)	148.5 (6.6)	87.7 (5.5)	59.0 (4.6)
114.0	392.8 (10.7)	193.8 (8.3)	132.6 (6.7)	191.1 (8.3)
123.7	358.7 (10.5)	208.9 (8.5)	208.7 (8.6)	358.9 (11.6)
133.2	275.4 (9.2)	190.6 (8.4)	293.0 (10.2)	369.7 (11.9)
142.7	245.0 (8.9)	251.5 (9.9)	285.9 (11.3)	265.5 (11.1)
152.1	228.8 (8.5)	377.6 (13.1)	305.4 (11.7)	251.0 (10.9)
161.4	189.9 (7.9)	538.0 (22.4)	480.4 (14.8)	292.0 (11.8)
170.7	124.4 (6.3)	701.9 (18.2)	687.9 (17.7)	422.6 (14.3)

Table I (iv)

$\theta_{c.m.}$ (deg) \ E_p (Mev)	12.08	12.17	12.25	12.37
21.4	517.9 (13.5)	392.9 (11.8)	454.4 (10.0)	370.1 (12.0)
32.1	482.7 (13.0)	352.2 (11.3)	261.5 (5.8)	286.9 (10.0)
42.7	410.9 (12.3)	324.5 (10.7)	155.3 (5.9)	203.1 (8.4)
53.2	318.1 (10.8)	297.3 (10.4)	107.3 (6.1)	145.4 (7.2)
63.7	237.6 (8.6)	250.6 (8.8)	106.4 (4.6)	158.2 (6.9)
74.0	274.4 (9.3)	186.2 (7.6)	122.8 (3.9)	133.4 (6.4)
84.2	260.4 (9.1)	166.7 (7.3)	72.4 (4.7)	100.0 (5.6)
94.2	202.7 (8.3)	136.9 (6.7)	60.4 (4.3)	78.0 (5.1)
104.2	146.4 (5.9)	143.3 (7.0)	69.2 (4.6)	89.4 (5.5)
114.0	171.2 (7.7)	151.9 (7.3)	101.7 (5.8)	112.6 (6.2)
123.7	194.9 (8.0)	179.1 (8.1)	133.4 (6.4)	127.7 (6.7)
133.2	183.8 (6.6)	183.1 (8.2)	122.4 (6.5)	105.7 (6.2)
142.7	139.6 (6.6)	206.2 (9.7)	113.1 (6.7)	58.4 (5.1)
152.1	147.9 (8.3)	240.6 (10.3)	125.1 (7.4)	110.7 (7.0)
161.4	202.9 (9.1)	256.6 (10.8)	178.3 (8.6)	216.4 (9.9)
170.7	272.7 (9 3)	282.1 (11.6)	173.1 (8.7)	366.8 (12.9)

Table I (v)

$\theta_{c.m.}$ (deg) \ E_p (Mev)	12.50	12.58	12.67	12.78
21.4	534.4 (13.4)	330.0 (10.3)	308.0 (10.3)	512.3 (13.3)
32.1	387.9 (11.4)	166.8 (7.5)	124.3 (6.3)	201.3 (8.4)
42.7	270.1 (9.7)	106.7 (6.0)	123.4 (6.5)	185.5 (8.1)
53.2	163.4 (7.6)	99.0 (5.8)	186.8 (8.2)	215.2 (8.6)
63.7	96.4 (3.8)	112.9 (4.8)	192.6 (7.6)	196.8 (7.8)
74.0	67.2 (4.5)	82.6 (5.0)	160.1 (7.1)	211.7 (8.1)
84.2	66.5 (4.6)	59.9 (4.3)	93.5 (5.4)	211.2 (11.6)
94.2	95.3 (5.6)	69.4 (4.7)	65.7 (4.6)	176.8 (7.4)
104.2	128.5 (5.3)	108.8 (5.9)	80.5 (5.2)	115.4 (5.9)
114.0	161.0 (7.4)	144.1 (6.9)	147.7 (7.1)	109.5 (8.7)
123.7	159.9 (7.9)	162.5 (7.4)	189.1 (8.2)	139.7 (7.0)
133.2	188.9 (11.6)	229.0 (12.5)	187.0 (11.6)	150.8 (8.9)
142.7	210.9 (7.9)	215.3 (9.6)	141.8 (7.9)	110.2 (6.6)
152.1	196.6 (8.8)	288.2 (11.2)	161.3 (8.5)	66.1 (5.1)
161.4	161.0 (12.0)	300.9 (11.5)	273.2 (11.1)	95.1 (6.6)
170.7	86.4 (6.2)	241.9 (10.1)	466.3 (20.6)	133.6 (7.8)

Table I (vi)

$\theta_{c.m.}$ (deg) \ E_p (Mev)	12.85	12.94	13.05	13.16
21.4	523.8 (16.1)	543.6 (14.0)	653.0 (12.0)	447.8 (11.4)
32.1	340.2 (11.0)	315.0 (10.8)	232.8 (8.8)	172.1 (7.1)
42.7	229.8 (9.1)	168.7 (7.9)	81.3 (4.2)	98.0 (5.4)
53.2	174.7 (8.0)	122.9 (6.8)	87.2 (5.5)	116.6 (5.9)
63.7	151.5 (6.9)	112.4 (6.0)	128.0 (5.0)	122.2 (5.6)
74.0	136.1 (6.6)	105.7 (5.9)	150.1 (6.6)	140.0 (6.0)
84.2	159.0 (7.2)	105.4 (6.0)	128.2 (5.1)	142.2 (6.2)
94.2	175.9 (7.7)	98.4 (5.8)	86.5 (5.2)	144.0 (6.3)
104.2	156.6 (7.3)	78.0 (5.3)	55.8 (4.2)	111.4 (5.5)
114.0	115.4 (6.4)	64.8 (4.9)	48.6 (4.0)	81.9 (4.0)
123.7	129.1 (6.8)	79.8 (5.5)	127.5 (6.5)	151.5 (6.6)
133.3	125.8 (6.8)	110.4 (6.5)	210.9 (8.5)	263.1 (8.9)
142.7	100.9 (6.7)	111.9 (7.2)	238.0 (9.9)	346.0 (15.7)
152.1	101.4 (6.8)	117.9 (7.5)	229.0 (9.9)	288.1 (10.4)
161.4	107.7 (7.1)	73.8 (5.9)	180.6 (8.8)	168.0 (8.0)
170.7	91.8 (6.5)	62.3 (5.5)	108.5 (6.9)	71.0 (5.2)

Table I (vii)

E_p (Mev) / $\theta_{c.m.}$ (deg)	13.31	13.39	13.46	13.61
21.5	399.1 (10.9)	176.3 (7.2)	266.4 (8.8)	258.6 (8.7)
32.1	143.8 (6.6)	92.7 (5.2)	119.7 (5.9)	114.6 (5.9)
42.7	122.1 (6.1)	82.0 (4.7)	104.5 (5.6)	121.7 (6.1)
53.3	146.6 (6.7)	120.8 (6.0)	109.9 (5.7)	134.9 (6.4)
63.7	137.5 (4.2)	169.7 (6.6)	113.8 (5.4)	84.0 (4.7)
74.0	129.2 (5.9)	187.5 (7.0)	101.8 (7.3)	83.6 (4.7)
84.2	122.3 (5.8)	149.6 (6.0)	100.8 (5.2)	90.3 (5.0)
94.3	114.8 (5.7)	128.4 (6.0)	93.3 (5.0)	105.7 (5.4)
104.2	116.4 (5.6)	151.8 (6.6)	82.2 (4.7)	75.9 (4.7)
114.0	127.8 (6.1)	168.0 (7.0)	74.5 (4.6)	60.1 (4.2)
123.7	184.8 (7.5)	170.7 (7.1)	85.0 (5.0)	62.0 (4.3)
133.3	231.0 (8.5)	149.1 (6.7)	102.0 (5.5)	91.9 (5.3)
142.7	181.7 (7.9)	104.9 (6.3)	95.0 (5.8)	92.9 (5.9)
152.1	153.9 (7.6)	103.9 (6.3)	107.3 (6.4)	97.4 (6.1)
161.5	100.6 (6.3)	97.9 (6.1)	95.8 (6.0)	97.4 (6.1)
170.7	101.0 (6.3)	115.6 (6.7)	109.7 (5.2)	155.3 (7.8)

Table I (viii)

E_p (Mev) / $\theta_{c.m.}$ (deg)	13.71	13.83	13.96	14.06
21.5	237.2 (8.3)	215.9 (7.8)	158.8 (5.8)	141.8 (6.9)
32.1	147.5 (6.5)	128.6 (6.1)	146.1 (6.4)	180.3 (7.8)
42.7	140.9 (6.4)	148.7 (6.6)	178.4 (7.2)	214.3 (7.9)
53.3	126.9 (6.1)	144.2 (6.3)	182.5 (7.3)	229.8 (9.8)
63.7	80.4 (4.5)	100.4 (5.0)	119.1 (4.8)	102.4 (5.5)
74.0	58.5 (3.9)	78.5 (4.5)	82.9 (4.6)	60.7 (4.3)
84.2	49.9 (3.6)	73.9 (4.4)	86.3 (4.7)	69.5 (4.3)
94.3	73.1 (4.4)	86.9 (4.7)	118.1 (5.5)	130.6 (6.3)
104.2	74.4 (4.5)	108.9 (5.5)	121.8 (5.7)	140.2 (6.8)
114.0	87.2 (5.0)	97.3 (5.3)	97.9 (4.3)	118.6 (6.4)
123.7	97.7 (5.3)	103.1 (5.5)	80.5 (4.8)	148.3 (7.2)
133.3	117.0 (5.9)	151.0 (6.7)	133.0 (6.3)	165.4 (7.7)
142.7	113.3 (6.4)	182.0 (8.1)	203.3 (8.5)	252.8 (10.5)
152.1	127.5 (6.9)	223.9 (9.1)	262.3 (8.0)	223.6 (10.0)
161.5	232.6 (9.4)	262.5 (9.9)	267.5 (10.0)	143.7 (8.0)
170.7	400.1 (12.3)	359.0 (11.6)	220.1 (9.1)	70.4 (5.6)

Table I (ix)

$\theta_{c.m.}$ (deg) \ E_p (Mev)	14.16	14.28	14.45
21.5	136.8 (6.5)	77.4 (4.8)	132.1 (5.0)
32.1	122.9 (6.2)	58.5 (4.3)	65.0 (4.7)
42.7	174.9 (6.1)	95.2 (5.7)	159.6 (10.5)
53.3	156.2 (6.8)	135.6 (7.3)	186.2 (8.0)
63.7	103.0 (5.3)	98.2 (5.1)	167.0 (5.3)
74.0	37.9 (3.3)	54.3 (3.9)	51.1 (3.2)
84.2	60.4 (3.4)	66.3 (4.5)	30.8 (2.8)
94.3	89.1 (5.1)	99.3 (6.0)	41.1 (3.6)
104.2	141.7 (6.6)	144.1 (6.6)	67.3 (4.7)
114.0	147.7 (6.8)	185.6 (7.6)	119.6 (6.3)
123.7	189.7 (7.8)	216.0 (8.4)	158.9 (7.4)
133.3	238.1 (8.8)	229.5 (7.6)	137.9 (7.0)
142.7	268.1 (10.4)	232.5 (5.5)	171.2 (8.6)
152.1	249.6 (10.1)	163.2 (8.1)	114.0 (7.0)
161.5	153.3 (8.0)	114.3 (6.9)	80.5 (6.0)
170.7	48.2 (4.5)	71.3 (7.7)	23.8 (3.3)

Table I (x)

$\theta_{c.m.}$ (deg) \ E_p (Mev)	14.50	14.55
21.5	120.7 (6.5)	141.1 (8.5)
32.1	123.1 (6.6)	123.1 (6.7)
42.7	202.6 (8.5)	193.1 (8.3)
53.3	235.9 (9.1)	245.0 (9.5)
63.7	184.5 (7.6)	194.5 (6.0)
74.0	97.4 (5.6)	117.8 (6.2)
84.2	57.2 (4.3)	83.7 (5.2)
94.3	64.5 (4.5)	80.1 (5.2)
104.2	66.7 (4.8)	58.2 (4.5)
114.0	79.0 (5.3)	49.5 (4.2)
123.7	106.4 (6.2)	64.4 (4.8)
133.3	127.5 (6.9)	79.8 (4.9)
142.7	132.8 (7.8)	111.1 (7.1)
152.1	114.4 (7.3)	85.6 (6.0)
161.5	65.9 (5.5)	50.0 (4.8)
170.7	38.1 (4.2)	19.6 (3.0)

Table II (i) Differential cross sections of the reaction $Al^{27}(p, \alpha_1)Mg^{24*}$ resulting in the first excited state of Mg^{24}.

$\left(\frac{d\sigma}{d\Omega}\right)_{c.m.}$ (μb/sterad)

$\theta_{c.m.}$ (deg) \ E_p (Mev)	10.65	10.83	10.99	11.11
21.5	2881 (37)	3588 (37)	2716 (53)	2403 (34)
32.2	2914 (27)	2247 (20)	2223 (47)	2152 (23)
42.9	3045 (33)	1529 (19)	1841 (43)	1976 (22)
53.4	2788 (34)	1360 (15)	1581 (29)	1927 (21)
63.9	2458 (32)	1522 (16)	1467 (39)	1257 (22)
74.2	2103 (22)	1575 (16)	1721 (43)	1317 (17)
84.4	1916 (21)	1632 (19)	1996 (47)	1138 (16)
94.5	1729 (20)	1646 (16)	2171 (35)	1249 (17)
104.4	1592 (20)	1287 (14)	1840 (45)	1362 (18)
114.2	1572 (20)	1237 (15)	1604 (45)	1372 (18)
123.9	1560 (20)	1300 (16)	1463 (42)	1357 (18)
133.4	1542 (20)	1374 (15)	1717 (48)	1399 (19)
142.9	1667 (23)	1444 (17)	1848 (49)	1680 (23)
152.2	1579 (23)	1341 (18)	2422 (57)	2011 (25)
161.5	1482 (22)	1219 (18)	2257 (55)	2227 (27)
170.8	1377 (21)	1211 (16)	2062 (47)	2203 (27)

Table II (ii)

$\theta_{c.m.}$ (deg) \ E_p (Mev)	11.22	11.25	11.41	11.45
21.5	2514 (28)	2405 (25)	3137 (30)	2350 (27)
32.2	2595 (26)	2415 (23)	3060 (26)	2253 (22)
42.9	2245 (23)	2160 (18)	2615 (24)	2162 (23)
53.4	2077 (22)	2041 (21)	2130 (22)	1810 (20)
63.9	1462 (22)	1603 (21)	1625 (23)	1412 (22)
74.2	1242 (18)	1307 (18)	1505 (19)	1183 (16)
84.4	1286 (18)	1242 (14)	1606 (20)	1189 (18)
94.5	1409 (19)	1437 (19)	1808 (22)	1403 (19)
104.4	1552 (20)	1533 (20)	1701 (21)	1657 (21)
114.2	1541 (21)	1614 (21)	1558 (21)	1965 (24)
123.9	1691 (22)	1624 (21)	1580 (21)	2071 (25)
133.4	1900 (23)	1997 (22)	1895 (23)	2097 (25)
142.9	2206 (25)	2469 (27)	2444 (27)	2103 (25)
152.2	2442 (27)	2610 (28)	2944 (29)	2282 (27)
161.5	2416 (27)	2375 (26)	3238 (31)	2667 (29)
170.8	2322 (27)	2100 (25)	3326 (31)	3072 (31)

Table II (iii)

E_p (Mev) / $\theta_{c.m.}$ (deg)	11.53	11.70	11.80	11.91
21.5	3203 (25)	2398 (31)	1683 (24)	1856 (25)
32.2	2906 (26)	2032 (30)	1633 (24)	1467 (23)
42.9	2089 (23)	1429 (23)	1447 (23)	1188 (21)
53.4	1607 (20)	1007 (19)	1269 (21)	1029 (20)
63.9	1409 (18)	955 (17)	943 (17)	920 (17)
74.2	1422 (19)	986 (18)	822 (16)	928 (18)
84.4	1546 (21)	1040 (18)	873 (17)	924 (18)
94.5	1638 (22)	902 (17)	920 (17)	864 (17)
104.4	1749 (24)	869 (16)	894 (17)	785 (17)
114.2	1778 (23)	1046 (19)	976 (18)	856 (18)
123.9	1854 (24)	1241 (21)	1062 (20)	951 (19)
133.4	1688 (23)	1396 (23)	1106 (20)	989 (20)
142.9	2016 (26)	1654 (27)	1234 (24)	1003 (22)
152.2	1867 (26)	1802 (29)	1292 (24)	1100 (22)
161.5	1536 (23)	2098 (44)	1623 (28)	1241 (25)
170.8	1262 (20)	2405 (34)	1732 (28)	1514 (27)

Table II (iv)

E_p (Mev) / $\theta_{c.m.}$ (deg)	12.08	12.17	12.25	12.37
21.5	1435 (23)	1479 (23)	2168 (22)	1610 (24)
32.2	1084 (22)	1215 (20)	1082 (11)	1166 (20)
42.9	959 (19)	1162 (20)	784 (13)	818 (17)
53.4	985 (19)	1143 (20)	683 (15)	780 (17)
63.9	1082 (20)	1134 (19)	747 (12)	928 (17)
74.2	1133 (19)	1032 (18)	857 (10)	976 (18)
84.4	1026 (20)	994 (18)	722 (15)	942 (17)
94.5	952 (18)	940 (18)	874 (17)	906 (17)
104.4	870 (14)	915 (18)	961 (17)	1065 (21)
114.2	799 (17)	933 (18)	1134 (19)	1123 (20)
123.9	803 (16)	965 (19)	1110 (19)	1101 (20)
133.4	800 (14)	898 (19)	1017 (21)	1002 (20)
142.9	981 (17)	990 (21)	1015 (20)	1012 (21)
152.2	1114 (23)	1065 (22)	1133 (22)	1074 (22)
161.5	1226 (23)	1249 (24)	1106 (21)	1101 (22)
170.8	1126 (19)	1386 (26)	861 (20)	1066 (22)

Table II (v)

E_p (Mev) / $\theta_{c.m.}$ (deg)	12.50	12.58	12.67	12.78
21.5	1895 (25)	1766 (24)	1543 (23)	1300 (21)
32.2	1339 (21)	1335 (21)	1085 (20)	852 (17)
42.9	896 (18)	932 (18)	852 (17)	673 (16)
53.4	760 (16)	748 (17)	641 (15)	760 (17)
63.9	790 (11)	694 (15)	620 (14)	837 (16)
74.2	598 (14)	576 (13)	585 (14)	628 (14)
84.4	530 (13)	489 (12)	524 (13)	443 (11)
94.5	724 (15)	608 (14)	549 (13)	511 (13)
104.4	1009 (15)	848 (17)	653 (15)	719 (15)
114.2	1273 (21)	1158 (20)	926 (19)	887 (25)
123.9	1285 (21)	1247 (21)	1265 (21)	1038 (19)
133.4	1207 (29)	1207 (28)	1482 (33)	1097 (19)
142.9	1133 (18)	1337 (24)	1654 (27)	1264 (23)
152.2	1220 (23)	1454 (25)	1657 (27)	1451 (26)
161.5	1398 (36)	1613 (27)	1692 (28)	1691 (28)
170.8	1819 (29)	1802 (28)	1555 (38)	2001 (31)

Table II (vi)

E_p (Mev) / $\theta_{c.m.}$ (deg)	12.85	12.94	13.05	13.16
21.5	1675 (24)	1692 (25)	1953 (20)	1682 (22)
32.2	1048 (19)	1142 (20)	1576 (22)	1346 (20)
42.9	835 (17)	926 (19)	1138 (16)	1112 (20)
53.4	932 (18)	940 (19)	856 (17)	728 (15)
63.9	920 (17)	837 (16)	749 (12)	757 (14)
74.2	721 (15)	673 (15)	678 (14)	719 (14)
84.4	476 (12)	534 (13)	655 (11)	664 (13)
94.5	447 (10)	599 (14)	615 (14)	694 (13)
104.4	616 (14)	700 (16)	775 (16)	808 (15)
114.2	775 (17)	745 (17)	913 (17)	914 (16)
123.9	981 (19)	820 (18)	963 (18)	892 (16)
133.4	1102 (20)	869 (18)	882 (17)	959 (17)
142.9	1199 (23)	982 (22)	933 (19)	1052 (22)
152.2	1322 (25)	1073 (23)	1175 (23)	1056 (20)
161.5	1396 (26)	1207 (24)	1431 (25)	963 (19)
170.8	1460 (26)	1305 (25)	1567 (26)	742 (17)

Table II (vii)

E_p (Mev) / $\theta_{c.m.}$ (deg)	13.31	13.39	13.46	14.61
21.5	1826 (23)	1229 (19)	691 (14)	695 (14)
32.2	1330 (20)	1129 (18)	614 (13)	612 (14)
42.9	940 (17)	1058 (17)	734 (15)	651 (14)
53.4	777 (16)	954 (18)	800 (15)	784 (16)
63.9	732 (10)	695 (13)	703 (14)	682 (13)
74.2	671 (13)	495 (11)	487 (16)	534 (12)
84.4	623 (13)	492 (11)	437 (11)	483 (12)
94.5	585 (13)	553 (12)	461 (11)	515 (12)
104.4	634 (13)	535 (12)	471 (11)	504 (12)
114.2	746 (15)	661 (14)	538 (13)	525 (12)
123.9	850 (16)	828 (16)	622 (14)	548 (13)
133.4	973 (17)	1059 (18)	724 (15)	655 (14)
142.9	1091 (20)	1133 (21)	775 (16)	693 (16)
152.2	1212 (22)	1059 (20)	830 (18)	811 (18)
161.5	1072 (21)	1027 (20)	917 (19)	1046 (20)
170.8	898 (19)	980 (20)	1072 (20)	1317 (23)

Table II (viii)

E_p (Mev) / $\theta_{c.m.}$ (deg)	13.71	13.83	13.96	14.06
21.5	708 (14)	823 (15)	860 (13)	857 (17)
32.2	747 (15)	730 (15)	743 (15)	678 (15)
42.9	766 (15)	773 (15)	839 (16)	650 (14)
53.4	786 (15)	791 (15)	798 (15)	760 (16)
63.9	668 (14)	655 (13)	578 (10)	564 (13)
74.2	541 (12)	526 (12)	397 (10)	336 (10)
84.4	482 (11)	483 (11)	417 (10)	326 (9)
94.5	550 (12)	511 (11)	453 (11)	391 (11)
104.4	506 (12)	515 (12)	436 (11)	374 (11)
114.2	499 (12)	503 (12)	469 (9)	362 (11)
123.9	512 (12)	503 (12)	478 (12)	409 (12)
133.4	527 (13)	556 (13)	484 (12)	444 (13)
142.9	647 (15)	622 (15)	508 (14)	515 (15)
152.2	819 (18)	810 (17)	598 (12)	541 (16)
161.5	1024 (21)	1061 (20)	755 (17)	680 (18)
170.8	1239 (22)	1241 (22)	899 (18)	887 (20)

Table II (ix)

E_p (Mev) / $\theta_{c.m.}$ (deg)	14.16	14.28	14.45
21.5	829 (17)	760 (15)	692 (11)
32.2	494 (12)	641 (14)	607 (14)
42.9	534 (11)	684 (14)	667 (22)
53.4	640 (15)	657 (16)	808 (17)
63.9	518 (12)	561 (12)	554 (10)
74.2	299 (9)	422 (11)	403 (9)
84.4	297 (8)	353 (10)	283 (8)
94.5	336 (10)	350 (12)	324 (10)
104.4	381 (11)	387 (11)	345 (11)
114.2	365 (11)	459 (12)	336 (11)
123.9	361 (11)	427 (12)	346 (11)
133.4	348 (11)	451 (11)	338 (11)
142.9	316 (11)	358 (12)	427 (14)
152.2	358 (13)	318 (11)	359 (13)
161.5	422 (13)	345 (12)	329 (12)
170.8	516 (15)	451 (20)	299 (12)

Table II (x)

E_p (Mev) / $\theta_{c.m.}$ (deg)	14.50	14.55
21.5	695 (16)	604 (18)
32.2	544 (14)	524 (14)
42.9	554 (14)	582 (14)
53.4	601 (14)	597 (15)
63.9	529 (13)	461 (9)
74.2	330 (10)	319 (10)
84.4	251 (9)	278 (10)
94.5	314 (10)	319 (10)
104.4	324 (11)	313 (10)
114.2	369 (11)	350 (11)
123.9	334 (11)	340 (11)
133.4	360 (12)	306 (11)
142.9	379 (13)	435 (14)
152.2	424 (14)	596 (17)
161.5	365 (13)	657 (18)
170.8	322 (12)	673 (18)

Table III (i). Differential cross sections of the reaction $Mn^{55}(p, \alpha_0)Cr^{52}$ resulting in the ground state of Cr^{52}.

$\left(\frac{d\sigma}{d\Omega}\right)_{c.m.}$ (μb/sterad)

E_p (Mev) / $\theta_{c.m.}$ (deg)	7.65	8.85	9.65
20.6	147.8 (7.4)	72.2 (5.7)	58.7 (3.8)*
30.9	121.1 (5.2)	62.6 (4.0)	53.2 (3.1)*
41.2	112.1 (5.3)	70.4 (3.2)	45.6 (2.9)
51.4	114.3 (5.3)	53.1 (3.8)*	35.4 (2.3)*
61.6	114.4 (4.7)	53.1 (4.5)	24.5 (1.6)*
71.7	106.5 (4.5)	57.9 (3.5)*	23.8 (1.9)*
81.8	103.8 (4.6)	54.2 (2.5)	23.8 (1.9)*
91.9	102.7 (4.6)	56.6 (3.5)	25.5 (1.8)
101.8	113.8 (4.1)	55.4 (3.4)	29.8 (1.7)*
111.7	114.3 (4.4)	53.8 (3.4)*	29.0 (1.6)*
121.6	109.6 (4.1)	59.4 (3.7)	30.4 (1.9)*
131.4	129.9 (3.4)	62.8 (3.6)*	31.9 (1.9)*
141.2	140.6 (5.0)	79.1 (4.4)	32.8 (2.0)
150.9	178.1 (6.6)	76.9 (4.5)	36.2 (2.0)*
160.6	180.6 (5.8)	69.5 (4.4)	46.6 (2.6)*
170.3	205.4 (5.1)	53.1 (3.7)	51.5 (2.7)

* Corresponding $\theta_{c.m.}$ should be added by 0.1° to the tabulated angle $\theta_{c.m.}$.

Table III (ii)

E_p (Mev) / $\theta_{c.m.}$ (deg)	10.7	11.8	12.9
20.7	28.4 (2.2)	27.1 (2.8)	15.3 (1.5)
31.0	23.4 (1.6)	21.5 (2.2)	9.17 (0.93)
41.2	35.7 (1.8)	13.5 (1.4)	5.69 (0.67)*
51.5	33.0 (1.5)	9.53 (1.09)	6.08 (0.75)
61.7	21.0 (1.2)	8.91 (1.01)	5.49 (0.54)
71.8	16.8 (1.2)	6.05 (0.94)	6.26 (0.64)
81.9	14.6 (1.1)	8.53 (0.97)	5.10 (0.58)
91.9	17.3 (1.0)	7.21 (0.88)	4.58 (0.59)*
101.9	20.1 (1.1)	7.88 (0.91)	3.94 (0.50)
111.8	22.1 (1.2)	9.29 (0.84)	2.87 (0.39)
121.7	23.4 (1.2)	8.72 (1.13)	3.44 (0.43)
131.5	18.6 (1.1)	9.29 (0.73)	2.82 (0.38)
141.2	20.7 (1.2)	9.55 (1.11)	4.15 (0.56)*
151.0	18.1 (1.2)	11.8 (0.93)	5.99 (0.62)
160.7	17.5 (1.2)	14.1 (1.3)	8.46 (0.74)
170.3	18.1 (1.2)	18.1 (1.4)	6.13 (0.63)

Table IV (i). Differential cross sections of the reaction $Mn^{55}(p,\alpha_1)Cr^{52*}$ resulting in the first excited state of Cr^{52}.

$\left(\frac{d\sigma}{d\Omega}\right)_{c.m.}$ (μb/sterad)

E_p (Mev) / $\theta_{c.m.}$ (deg)	7.65	8.85	9.65
20.7	459.6 (13.0)	349.9 (12.6)	274.2 (8.3)
31.0	419.0 (9.7)	296.5 (8.6)	271.5 (7.0)
41.3	390.8 (9.9)	300.5 (6.6)	226.6 (6.4)
51.5	364.0 (9.5)	297.9 (8.3)	165.0 (5.0)*
61.7	299.2 (7.6)	255.4 (9.7)	149.9 (4.0)*
71.9	276.6 (7.2)	205.1 (6.6)	137.0 (4.5)
82.0	275.0 (7.6)	192.0 (4.8)	128.7 (4.4)
92.0	277.8 (7.5)	169.0 (5.7)	143.2 (4.2)
102.0	280.2 (6.4)	167.1 (5.9)	132.7 (3.7)
111.9	285.8 (6.8)	166.7 (6.0)	148.0 (3.7)
121.7	294.6 (6.7)	182.8 (6.4)	158.4 (4.4)*
131.5	294.6 (5.2)	197.4 (6.5)	159.5 (4.3)*
141.3	335.2 (7.8)	237.0 (7.6)	169.1 (4.5)
151.0	380.6 (8.8)	246.3 (7.9)	191.6 (4.6)
160.7	418.1 (8.8)	261.7 (8.4)	198.4 (5.4)
170.3	585.3 (8.3)	259.8 (8.1)	208.1 (5.4)

Table IV (ii)

E_p (Mev) / $\theta_{c.m.}$ (deg)	10.7	11.8	12.9
20.7	203.7 (5.9)	153.2 (6.6)	128.5 (4.4)
31.0	169.0 (4.2)	130.1 (4.8)	109.9 (3.2)
41.3	142.7 (3.7)	105.8 (3.8)	73.1 (2.4)
51.6	117.0 (2.8)	81.4 (3.4)	47.2 (2.1)
61.8	94.4 (2.6)	51.2 (2.4)	34.5 (1.4)
71.9	83.4 (2.8)	50.1 (2.7)	28.4 (1.4)
82.0	79.6 (2.5)	45.8 (2.2)	26.2 (1.3)
92.0	76.7 (2.1)	41.0 (2.1)	22.6 (1.3)
102.0	74.4 (2.2)	42.1 (2.1)	23.9 (1.2)
111.9	70.9 (2.2)	44.6 (1.8)	20.5 (1.1)
121.8	75.5 (2.2)	47.9 (2.1)	23.6 (1.1)
131.6	90.3 (2.4)	46.3 (1.6)	26.2 (1.2)
141.3	109.9 (2.8)	53.0 (2.6)	29.8 (1.5)
151.0	116.3 (3.0)	52.9 (2.0)	29.4 (1.4)
160.7	107.2 (2.9)	62.2 (2.6)	32.9 (1.5)
170.4	102.9 (2.9)	63.3 (2.6)	36.1 (1.5)

Table V (i). Differential cross sections of the reaction $Co^{59}(p, \alpha_0)Fe^{56}$ resulting in the ground state of Fe^{56}.

$\left(\frac{d\sigma}{d\Omega}\right)_{c.m.}$ (μb/sterad)

E_p (Mev) / $\theta_{c.m.}$ (deg)	7.7	8.7	9.8	10.85
20.6	156.6 (7.9)	76.6 (5.7)	52.8 (2.6)	42.9 (5.0)
30.8	127.5 (4.9)	85.9 (5.5)	47.0 (2.9)*	33.5 (2.3)*
41.1	115.8 (4.5)	71.2 (2.9)	42.3 (2.0)	32.8 (1.9)
51.3	101.2 (4.3)	63.0 (2.7)	37.9 (1.8)	21.4 (1.2)
61.5	78.3 (4.0)	51.2 (2.9)	32.5 (1.5)	20.5 (1.2)
71.6	70.7 (3.7)	50.7 (2.8)	35.7 (1.7)	17.4 (1.2)
81.7	71.7 (3.7)	46.5 (2.4)	26.3 (1.6)	13.2 (1.0)
91.7	77.8 (3.8)	41.0 (2.3)	24.2 (1.5)	14.9 (1.0)
101.7	71.2 (3.7)	36.8 (2.2)	23.5 (1.6)	15.3 (1.1)
111.6	84.6 (3.8)	37.1 (2.1)	23.1 (1.7)	17.2 (1.2)
121.5	84.9 (4.1)	45.6 (2.4)	28.4 (1.7)	17.1 (1.2)
131.3	107.5 (4.6)	54.3 (2.7)	37.7 (1.9)	17.4 (1.2)
141.1	88.0 (4.2)	61.8 (2.8)	39.7 (2.1)	21.2 (1.3)
150.8	89.7 (4.0)	66.6 (2.8)	45.5 (2.5)*	19.9 (1.3)*
160.6	89.8 (3.5)	66.6 (3.0)	41.9 (2.1)	18.1 (1.2)
170.3	102.2 (4.5)	66.6 (3.0)	45.5 (2.1)	22.6 (2.4)

Table V (ii)

E_p (Mev) / $\theta_{c.m.}$ (deg)	11.9	13.1	14.1
20.6	50.9 (4.6)	42.0 (3.2)	74.0 (5.9)
30.9	30.0 (2.0)	27.9 (2.0)	39.5 (3.4)
41.1	19.0 (1.1)	18.9 (1.1)	19.2 (1.3)*
51.4	10.4 (0.65)	8.94 (0.72)	9.45 (0.82)
61.5	9.81 (0.88)	4.50 (0.54)	6.76 (0.65)*
71.7	7.60 (0.80)	6.98 (0.67)	4.55 (0.55)
81.7	7.82 (0.70)	7.84 (0.69)	5.27 (0.69)*
91.8	5.61 (0.51)	3.75 (0.48)	4.52 (0.58)
101.7	5.77 (0.65)	3.81 (0.41)	4.01 (0.59)*
111.7	5.28 (0.63)	4.56 (0.58)	3.71 (0.57)
121.5	7.82 (0.60)	4.44 (0.54)	4.34 (0.53)*
131.4	9.43 (0.87)	6.34 (0.62)	3.02 (0.47)
141.1	8.68 (0.82)	8.19 (0.62)	3.62 (0.57)*
150.9	7.98 (0.78)	5.65 (0.66)	5.19 (0.69)
160.6	6.31 (1.21)	7.09 (0.69)	4.47 (0.60)
170.3	8.14 (0.81)	14.3 (2.4)	6.80 (1.12)

Table VI (i). Differential cross sections of the reaction $Co^{59}(p, \alpha_1)Fe^{56*}$ resulting in the first excited state of Fe^{56}.

$\left(\frac{d\sigma}{d\Omega}\right)_{c.m.}$ (μb/sterad)

E_p Mev / $\theta_{c.m.}$ (deg)	7.7	8.7	9.8	10.85
20.6	400.2 (12.7)	196.8 (9.0)	171.8 (4.7)	118.1 (8.3)
30.9	368.2 (8.1)	234.2 (9.1)	163.2 (5.4)	143.3 (4.9)
41.2	339.7 (7.8)	221.7 (5.1)	165.1 (4.0)	113.7 (2.8)
51.4	328.3 (7.7)	224.0 (5.2)	141.4 (3.5)	80.6 (2.4)
61.6	304.8 (7.9)	199.7 (5.8)	131.7 (2.9)	69.7 (2.3)
71.7	260.0 (7.0)	203.7 (5.7)	122.5 (3.1)	68.4 (2.3)
81.8	265.8 (7.0)	199.7 (5.0)	135.9 (3.7)	72.4 (2.4)
91.8	297.1 (7.4)	184.9 (4.8)	131.0 (3.5)	63.3 (2.2)
101.8	317.5 (7.8)	201.8 (5.1)	125.9 (3.8)	57.3 (2.1)
111.7	308.2 (7.3)	188.9 (4.7)	112.8 (3.9)	55.9 (2.1)
121.6	326.3 (7.9)	203.0 (5.1)	120.5 (3.6)	58.4 (2.2)
131.4	338.5 (8.2)	205.7 (5.1)	113.8 (3.3)	73.0 (2.4)
141.2	350.4 (8.3)	217.7 (5.3)	123.8 (3.8)	84.2 (2.6)
150.9	340.5 (7.8)	217.6 (5.2)	133.3 (4.2)	81.6 (2.6)
160.6	317.8 (8.0)	229.7 (5.5)	155.4 (4.2)	91.2 (2.7)
170.3	314.4 (8.0)	233.5 (5.6)	150.2 (3.8)	79.6 (4.5)

Table VI (ii)

E_p (Mev) / $\theta_{c.m.}$ (deg)	11.9	13.1	14.1
20.6	98.0 (6.3)	110.7 (5.2)	109.6 (7.2)
30.9	110.7 (3.9)	110.7 (4.0)	112.5 (5.8)
41.2	81.1 (2.2)	69.4 (2.0)	63.0 (2.4)
51.4	46.0 (1.4)	41.4 (1.6)	29.7 (1.5)
61.6	36.2 (1.7)	26.1 (1.3)	22.9 (1.2)
71.7	36.0 (1.7)	28.6 (1.4)	27.7 (1.4)*
81.8	29.1 (1.3)	27.5 (1.3)	26.0 (1.5)
91.9	30.6 (1.2)	25.0 (1.2)	17.3 (1.1)
101.8	38.6 (1.9)	20.8 (1.0)	13.1 (1.1)
111.7	35.0 (1.6)	21.5 (1.3)	18.3 (1.3)*
121.6	39.9 (1.4)	25.7 (1.3)	18.4 (1.1)
131.4	51.0 (2.2)	26.9 (1.3)	21.3 (1.2)
141.2	45.3 (1.9)	25.8 (1.1)	25.2 (1.5)
150.9	41.2 (1.7)	25.8 (1.4)	25.1 (1.5)
160.6	47.9 (3.4)	24.3 (1.0)	25.7 (1.5)
170.3	48.9 (2.0)	38.5 (4.0)	24.4 (2.1)

Memoirs of the College of Science, University of Kyoto, Series A,
Vol. XXIX, No. 3, Article 3, 1961.

HYDROLOGICAL STUDY OF ATAMI HOT SPRINGS

BY

Kōzō YUHARA

(*Received December 27, 1960*)

ABSTRACT

In Atami spa, temperatures and heads of many hot springs were measured from 1953 to 1955, and their chemical constituents were also analysed. Geographical distribution of these elements suggests the underground structure of the springs, especially the underground flow of hot water and the intrusion of sea water. From the geochemical consideration for the chemical contents we presume that their origin is partly in the sea water.

Water-level observation in a hot-spring well was continued from 1954 to 1955. Tidal and barometric effects on this well were remarkable and interference effect produced by pumping other wells was also observed. These effects are discussed separately, and the transmissibility, the coefficient of storage and other physical characters are calculated.

PART I. GENERAL SURVEY OF ATAMI HOT SPRINGS

1. Introduction

The Atami spa, one of the most famous spas in Japan, is in the area formed by volcanic action of the Yugawara and Taga volcanoes and has been studied by many scientists geologically, geophysically and geochemically. Ōtuka and Kuno (**1**) mention that the source of the Atami hot springs is in "Yugashima group" which is thick strata of lavas and pyroclastics of pyroxene-andesites and basalts given by submarine eruptions during the older Miocene period because there are close relations between the spring- and group-distributions. Detailed geological investigation of Atami district was carried out by Ōtuka (**2**), who made clear that faults lead the hot water from deep underground to shallow formation. Fukutomi (**3**) classified the Atami hot springs into two series as the result of geochemical study. One of them is a series characterised by high temperature, large amounts of chloride and water rising through fissures from deep to shallow, while the other series differs from the former in their relatively low temperature and some content of sulphate, and the springs belonging to this series are spread extensively. He called the former "the hot springs in the central region" and the latter "the hot springs in the marginal region". It is interesting to know the present condition of the Atami hot springs, because a lapse of about 20 years

from Fukutomi's investigation may bring about some changes. It may also be of value to recognize such changes in order to know the nature of the hot springs.

About 100 years ago there were some natural hot springs and a geyser (Ōyu geyser) in Atami, but nowadays we find 250 hot-sprig wells. The flow of the natural springs decreased gradually with the progress of exploitation of other hot springs (**4**, **5**), and the Ōyu geyser stopped gushing in 1926. Most of the springs, at present, are wells, which are pumped except a few flowing spring. This may show that the hot springs communicate with each other in the underground, and the heads of them declined gradually.

On the other hand, it is well known that some hot springs near the sea are contaminated by sea-water intrusion. This intrusion increases the Cl-contents, lowers the temperature and depreciates the economical value of the hot springs. It is therefore important to know the degree of the intrusion in view of the protection of hot springs as underground resources.

The present writer observed, from 1953 to 1955, the head and the orifice temperature of about 80 hot springs in Atami, and analysed also the chemical contents. The results show not only the present situation of the springs, but also some information about the preceding problems, compared with past data.

2. Distributions of orifice temperature and chemical elements

The orifice temperature and some chemical elements of hot springs were measured twice, in August, 1953 as well as in August, 1954. The results are given in Table 1.

The distribution of orifice temperature in August, 1953 is shown in Fig. 1, being similar to that observed in August, 1954. Comparing them with the distribution in 1936 (**3**), we see the same trend that the highest temperature section of Atami is in "the central region", but near and at the south of the mouth of Wada River and on the northern sea-shore the temperature decreased. The distribution of Cl-content in 1953, described in Fig. 2, shows that there is much chlorine area near and at the south of the mouth of Wada River, though this area had less Cl-content in 1936.

Fukutomi (**3**) used a temperature-Cl diagram as an evidence that there are two distinct groups of hot springs in Atami. Plotting in this diagram the data obtained in the present observation, we get Fig. 3, in which the marks "●" represent the hot springs of the central region, and they deviate from the line indicated by Fukutomi, the difference between the central and the marginal regions being, however, not so obvious as found in 1936. On the other hand, it is clear that some springs lie approximately on the line A B. All of them are near and at the south of the mouth of Wada River, and they are shown in Fig. 3 by the

Table 1

No.	Temperature °C		Ph	Cl g/l		SO_4 mg/l	Methyl orange alkalinity mg/l	Remarks
	Aug., 1953	Aug., 1954	Aug., 1954	Aug., 1953	Aug., 1954	Aug., 1954	Aug., 1953	
1	78.0	82.0	7.9	1.54	2.09	564	15	
2	66.0			1.05			15	
3		54.0	7.7	11.70	11.10	1388	43	
4	75.0	69.8	8.2	0.47	0.49	690	30	
5	68.5	66.0	8.0	0.37	0.28	416	23	
6	71.3	75.5	8.2	0.42	0.41	760	30	
7	72.2	68.5	8.2	0.38	0.39	669	38	
8	62.3	59.2	7.9	0.40	0.44	710	26	
9		63.0	8.1	1.16	1.51	759	19	
10	91.2			2.18			21	
11	93.3	94.2	8.3	1.99	2.24	430	19	
12	91.2			1.87			26	
13	94.5	96.0	8.0			358	18	
14	91.5	92.2	8.3	1.23	1.77	484	15	
15	88.0	91.1	8.2	2.18	2.46	356	23	
16	88.5	90.2	7.8	1.88	2.17	382	22	
17	88.0	90.8	8.1		2.47	368	19	
18	94.3	95.7	8.2	3.23	3.26	248	23	
19	69.5	68.0	8.4			244	41	
20	71.6	67.3	7.9			290	47	
21	99.0	98.9	8.5	3.34	3.29	237	21	flowing spring
22	96.0	97.4	8.0	1.84	2.12	394	19	
23	95.0	91.4	8.3	1.49	1.86	435	22	
24	91.0	92.3	8.2	3.03	2.93	303	17	
25	94.0	95.0	8.0			309	21	
26	96.0			3.60			21	
27	79.0	75.0	8.0			303	30	
28	100.0	98.8	8.4	3.60	3.56	222	17	flowing spring
29	76.6	74.5	8.0			196	13	
30	71.3	69.0	8.2	1.36	1.40	91	27	
31	69.2	70.3	7.8	0.14	0.16	860	11	
32	55.0	57.8	8.1	0.13	0.10	190	38	
33	91.4	93.7	7.9	4.05	4.82	130	17	
34	52.0			2.18			23	
35	43.0	45.9	8.3	0.95	1.14	473	17	
36	53.5	53.2	7.9	1.55	1.51	388	14	
37	56.0	55.5	8.0	1.52	1.25	539	13	
38	57.0		7.7	0.25	0.21	830	15	
39	45.0	44.6	8.2	4.18	4.25	252	13	
40	46.0	49.5	8.5	3.67	3.97	917	19	
41	55.2	53.0	7.8	4.78	4.52	1024	21	
42	47.5	49.2	8.8	1.28	1.40	744	12	
43	49.0	51.7	8.5	2.60	2.96	956	13	
44	96.0						19	
45	95.5	97.1	8.2	4.40	4.52	139	21	
46	99.0	98.8	8.4	3.68	3.71	242	22	flowing spring
47	86.0	85.0	8.8	0.45	0.53	638	23	
48	96.0	95.5	8.1	3.61	3.54	214	11	flowing spring
49		70.5	8.0	2.01	2.18	224	16	
50		72.2	8.1	1.20	0.79	282	13	

Table 1 (continued)

No.	Temperature °C		Ph	Cl g/l		SO_4 mg/l	Methyl orange alkalinity mg/l	Remarks
	Aug., 1953	Aug., 1954	Aug., 1953	Aug., 1953	Aug., 1954	Aug., 1954	Aug., 1953	
51		72.0	8.6	1.04	1.20	341	33	
52	90.1	88.2	8.0	1.26	1.42	242	19	
53	60.5	60.7	7.9	0.22	0.24	850	16	
54	81.2	83.5	8.4	1.23	1.47	473	21	
55	79.0	79.5	8.4	1.37	1.53	520	15	
56		95.0	8.3	1.24	1.86	584	15	
57	74.0			0.91			32	
58		96.5	8.8	0.59	0.87	445	32	
59	58.8	60.5	7.8	0.22	0.77	902	23	
60	67.5	67.5	8.0	0.24	0.23	909	18	
61	48.3	51.1	7.6	5.51	5.90	1032	21	
62	52.0	50.5	8.0	0.22	0.22	873	21	
63	70.2		8.9	0.22	0.22	720	24	
64	65.2	65.7	8.0	0.28	0.33	753	20	
65	45.1	48.0	8.0	0.21	0.25		24	
66	38.0	36.8	8.0	0.04	0.02	36	44	
67	40.0	42.1	7.8	0.82	0.70	810	32	
68			8.3		4.14	750		
69					2.18			
70		77.0	7.9		0.42	690		
71		75.0	8.1		0.37	680		
72		48.0	7.1		0.50	141		
73		64.6	8.2		0.25	252		
74		81.5	7.9		1.42	529		
75		53.1	8.2		0.45	676		

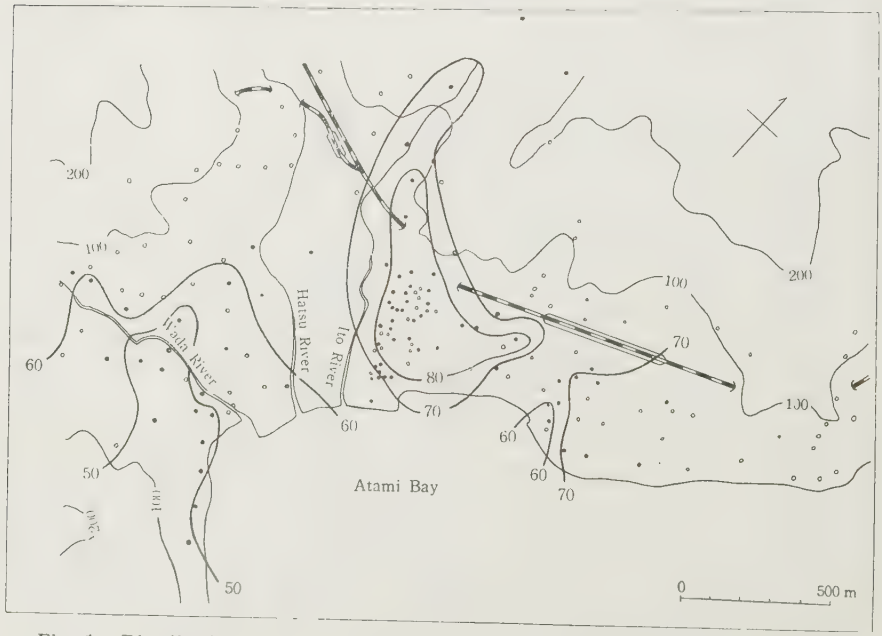

Fig. 1. Distribution of the spring temperature (C°) in 1953. Black points show the observed wells.

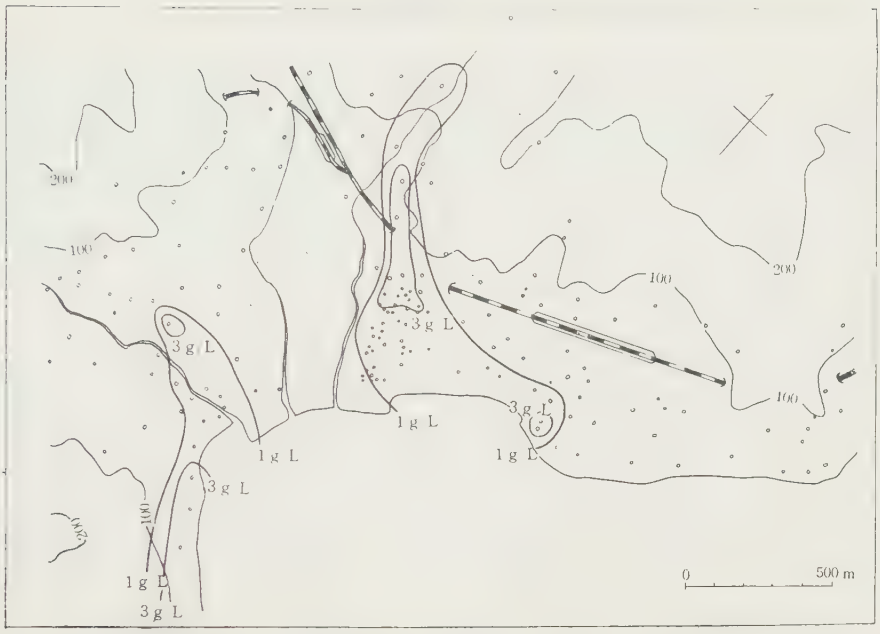

Fig. 2. Distribution of the Cl-content in 1953.

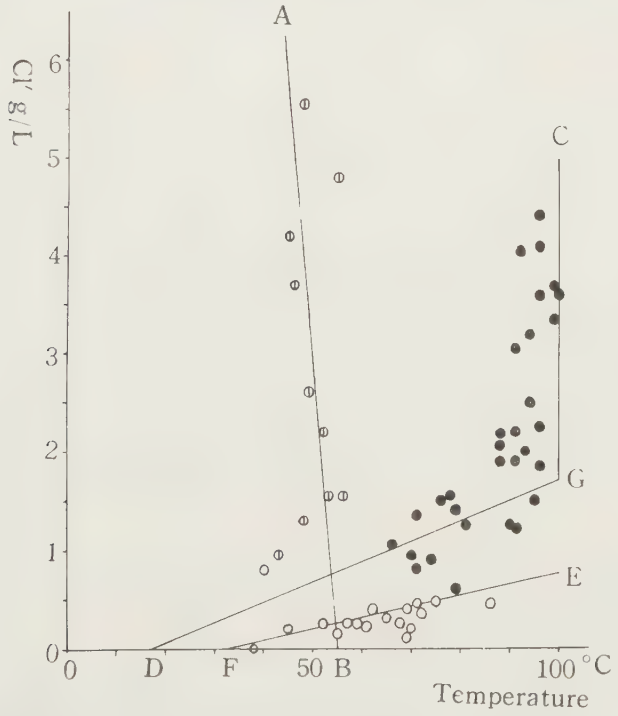

Fig. 3. Relation between the temperature and the Cl-content; "●" shows hot springs in the central region, "◐" hot springs near and at the south of the mouth of Wada River and they lie approximately on line A–B, and "○" hot springs in other region. Lines C–G–D and E–F were given by Fukutomi, who asserted that the hot springs in the central region lie along the former and those in the marginal region lie along the latter.

marks "Ⓘ". It may, therefore, be rational that we distinguish the hot springs near and at the south of the mouth of Wada River from other springs. If the line A–B is extended beyond A, it will pass near a point (Cl≒19 g/l, temp.=20°C) which is regarded as sea water. If, moreover, we assume that the sea water intrudes into land without temperature change, the hot springs on the line A–B are considered to be caused by the mixture of pure hot water as symbolized by point B with sea water. A probable cause of this intrusion of sea water is over-pumping hot water from the ground.

The present distribution of SO_4–content is similar to that in 1936, and the springs in the marginal region have more SO_4 than those in the central region. However, the area of less SO_4–content is narrowed in the northern part of the central region. If the hot springs of the central region are characterized by more chloride and less sulphate, as noted by Fukutomi, this feature of geographical distribution may suggest the slight decline of activities of hot springs in the central region.

The distribution of alkalinity is quite complicated. The high alkalinity is an index of HCO_3^- and CO_3^- contents, but they are affected by the escape of CO_2 from the hot water. It is therefore natural that the distribution of alkalinity is complicated.

3. Hydrostatic pressure of the hot springs in the central region

In order to estimate the underground flow of hot water, we must know the distribution of hydrostatic pressure. Ōtuka (2) showed the distribution of water tables of Atami hot springs along a line nearly parallel to the coastline from the data as obtained on the occasions of repairing the wells. From this distribution we may estimate that one source of Atami hot springs is in the central region, since the maximum water table is in this region. It is, however, inaccurate to estimate the flow from the data along a line, and it is desirable to get in areal range. However, it is very difficult to measure the hydrostatic pressure of all hot springs in Atami, because, in recent years, the water table of Atami hot springs are lowering gradually and air-lift-pumps are installed directly in most wells and also the structure of most private wells in the marginal region is beyond our scope. We therefore attempt to measure the hydrostatic pressure of the hot springs only in the central region.

The greater part of the wells in the central region is controlled by the Atami Municipal Office, so that their structures and pumping mechanisms are known. As soon as a pump starts, the pressure of the air-tank increases rapidly to the maximum, and then decreases asymptotically to a constant value. Since the maximum

denotes the hydrostatic pressure at the lower end of the air-tube, if the density of the hot water and the depth of the air-tube are known, we can calculate the height of the hydrostatic head by the air-tank pressure. When the hot water begins to issue from the upper end of the rising main, the head of hot water begins to decrease and then will settle in a steady state which corresponds to the constant value of air-tank pressure. Thus we can calculate the water head during pumping, too. The value of the specific weight of the hot water is different from spring to spring, but we here use the value of 0.99 g/cm^3, because the wells No. 17 and No. 45 have about 10 g l of total chemical contents, and if the temperature of hot water is 70°C the specific weight may be given approximately by the formula: 1 · 0.01 – 0.02 0.99. The total amount of the chemical contents used in this calculation is the highest and the temperature is nearly the lowest in this region. Discrepancy yielded by use of this presumed constant will be examined subsequently. As it is also possible to calculate the hydrostatic pressure of the hot water at the bottom of the well, we can then compare the pressure with that of the sea water at the same depth. In this calculation we also use the density of 0.99 g/cm^3 for the hot water and 1.03 g cm^3 for the sea water. Fig. 4 shows the distribution of the pressure differences between the hot water and the sea water during both pumping and stopping. In this figure we find a zone of high head with the shape of a tongue extending to the coast. This feature is also maintained during the course of pumping, but on this occasion, the zone where the pressure difference between the hot water and the sea water is positive is narrowed and consequently many of the hot springs may be in a negative domain.

The total amount of the chemical contents used in the present calculation is the maximum one in the region and also the minimum temperature in the region is used for the temperature, so that the pressure of each hot spring is less than that calculated. After all, the actual zone having positive pressure difference may be smaller than that shown in Fig. 4. Since the pressure measurement of the air-tank during pumping is not of long duration, the water table might not reach a steady state, and longer pumping may bring about more reduction of positive zone.

Since we could not get a core sample in Atami, the detailed underground geological conditions are unknown. From the results of the geological investigation of the ground surface, Ōtuka (2) considered that the hot springs in Atami form a water table as ground water because there are many large and small fissures in the Yugasima group. This consideration gives us an idea that the hot springs in this region may have an aquifer. The aquifer, furthermore, may be artesian, since there are a few flowing springs. If the aquifer is connected

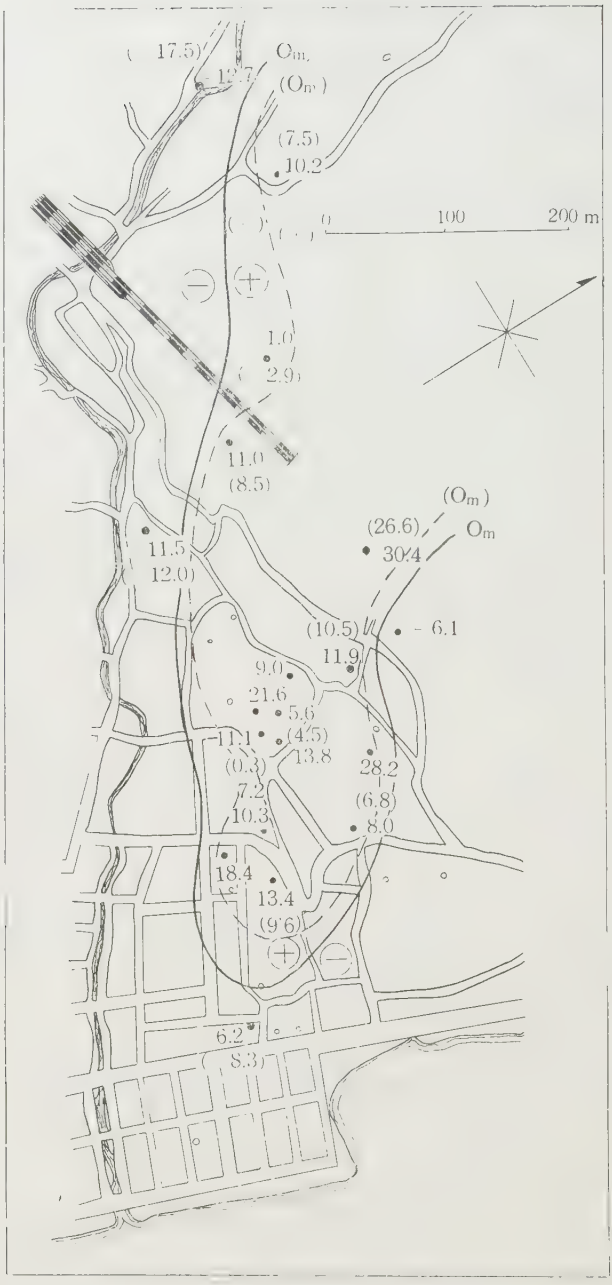

Fig. 4. Distribution of the difference of the hydrostatic pressure between the hot springs and the sea water at the depth of well bottom. It is shown by column length of pure water, and full curve shows statical state and dotted curve and numbers in parenthesis show the pumping state, in August, 1954, and the marks of plus show that the pressure of hot spring in this area is larger than that of sea water.

with the sea, the hot spring having smaller pressure than sea will give rise to the decrease in temperature and the increase in Cl-content. As a matter of fact, Wells No. 19, No. 25, No. 27 and No. 29 have a tendency of decreasing temperature and increasing Cl content. Therefore, it may be natural to regard this aquifer to be connected with the sea.

4. Some considerations on the origin of the chemical contents

The hot springs near, and at the south of, Wada River are diluted by the sea water as shown in §2, and there also may be a suspicion about sea water intrusion to some part of the central region where the springs have lower pressure than that in the sea water. These hot springs are shown in Fig. 5 with the marks "●", and had, in 1936, Cl content less than 0.5 g/l and further less other components. When such hot water is mixed with the sea water, it may approach, more or less, to the sea water in chemical composition.

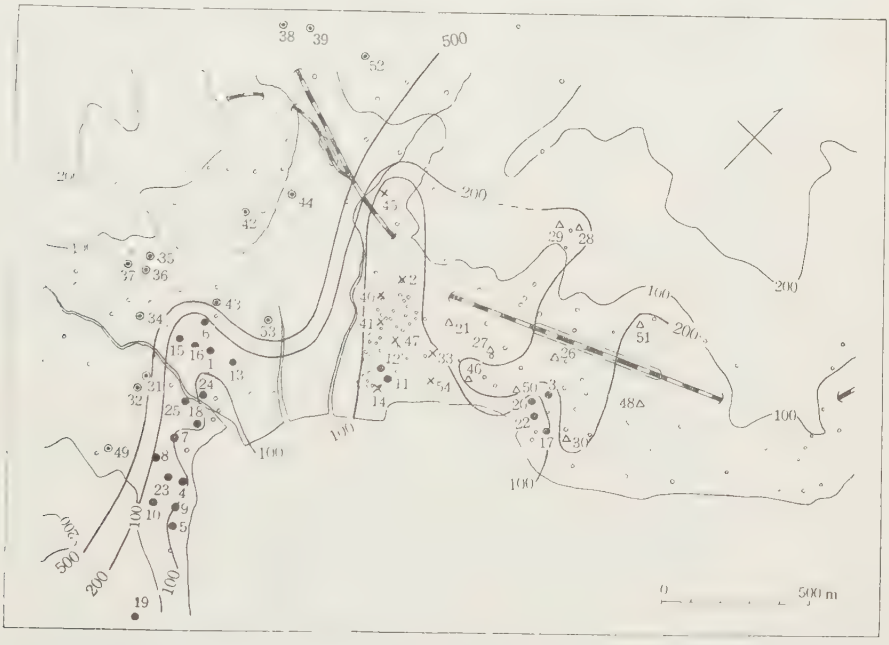

Fig. 5. Distribution of the "deviation". The marks, ●, ⊙, △ and ×, correspond to types, (a), (b), (c) and (d), in Fig. 6; side figures are the analysis number.

Seno (7) used a method of comparing Na, SO_4, Mg, Ca and K with Cl in weight and then illustrated the results in a diagram. He also introduced the total deviation "δ" of the hot water, which is defined as follows:

$$\delta_X = \left\{ \frac{X \text{ (hot water)}}{Cl \text{ (hot water)}} - \frac{X \text{ (sea water)}}{Cl \text{ (sea water)}} \right\} \times 100 ,$$

and

$$\delta = |\delta_{Na}| + |\delta_{SO_4}| + |\delta_{Mg}| + |\delta_{Ca}| + |\delta_K|.$$

Then the total deviation δ is an index to show whether the salts of water are originated from the sea water or not. He also suggested that when $\delta \leq 30$, the source of salts must be in the sea water and when $30 < \delta \leq 50$, it may be in the sea water.

Analysis tables of Atami hot springs in recent years are collected in "Nippon Kōsenshi" (8), from which we shall infer the origin of chemical elements of Atami hot springs. When the chemical elements of the hot springs near the mouth of Wada River are illustrated in Seno's diagram, they show a feature unlike that of the sea water, as seen in Fig. 6 (a). The values of δ in this area are about

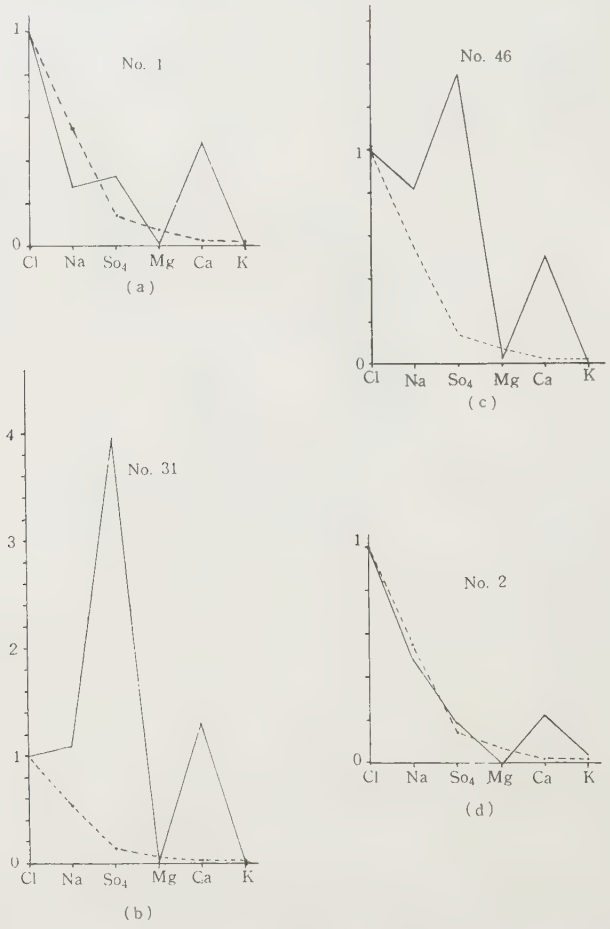

Fig. 6. Examples of Seno's diagram of the hot springs, (a) near and at the south of Wada River, (b) in the south-western part, (c) in the northern high ground, and (d) in the central region of Atami; dotted lines show the sea water.

100~200. Though it may not be correct to regard, from this diagram, the chemical elements of these springs as coming from sea water, yet it may be true, judging from the fact described in § 2, that most of Cl ions of the hot water come from the sea water. Thus, the chemical contents of these hot springs consist of some matter, of the magmatic- and the marine-origin, and are influenced by the surrounding formation by such chemical actions as solution, sedimentation and ion exchange. If a chemical composition with the same ratio as the sea water is subtracted from the composition of these hot water, the rest expressed in equivalent per million is negative for Na, K, and Mg ions, and the sum of their absolute values and SO_4 value is equal to the Ca value (see Fig. 7). From these results

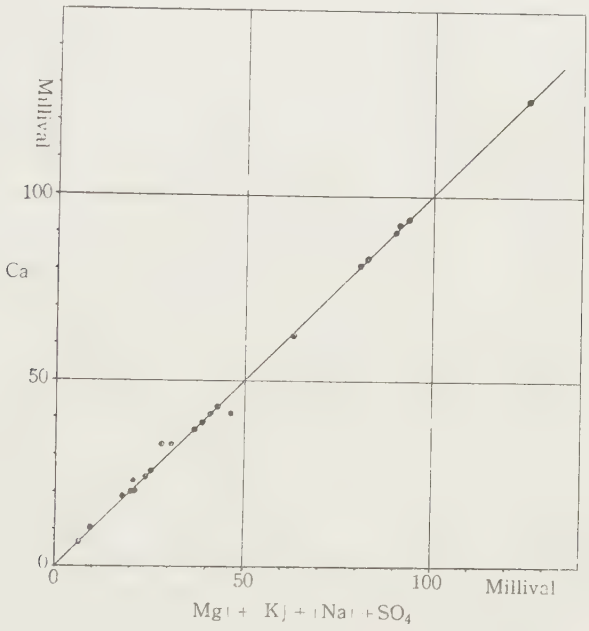

Fig. 7. Relation among Mg, K, Na, SO_4 and Ca residuals, which are introduced by substracting a chemical composition having the same ratio as sea water from the composition of hot water.

we may deduce the conclusion that $CaSO_4$ is dissolved in pure hot water of less chemical contents, and Na, K and Mg ions added to it by the intrusion of sea water are exchanged with Ca ions in the surrounding formations, thus finally the hot water has the present chemical constituents. According to this interpretation, there is little dissolved matter originating in the magma, and $CaSO_4$ is required in the ground. It is confirmed by Kuno (9) that gypsum exists as the secondary mineral in this district. The cation exchange in the hot water may

also be possible as in ground-water reported by Love (**10**). After his interpretation, the following discussion may be introduced. "In earlier geologic history the whole area of Atami was submerged beneath the sea and therefore was saturated with sea water. After emergence from the sea, the salty water was gradually flushed out of the formation by the hot water which contains much Ca ions. During this leaching and flushing, the colloids saturated with Na, K and Mg ions were thus brought into contact with water containing Ca as its chief basic constituent. Cation exchange took place leaving the colloids saturated with Ca ion while Na, K and Mg ions were removed from the aquifer by the flushing action. When exchange process is reversed by new intrusion of the sea water, the active colloids give up Ca ion in exchange for Na, K and Mg ions in the sea water. The resulting concentration of cation in the contaminated hot water tends to be higher in Ca and lower in Na, K and Mg than would be expected from simple mixtures of hot water containing $CaSO_4$ and sea water."

The hot springs on the northern beach of Atami have the same character as those near the mouth of Wada River. They are also shown in Fig. 5 by the marks "●", and might be contaminated by the sea water. The hot springs shown in Fig. 5 by the marks "⊙" are distributed in the south-western part of Atami, and have about 2 g/l of the total amount of chemical contents which is less than those of other springs. They also have a type of chemical elements shown in Fig. 6 (b), the "deviation" of which is more than 400. A characteristic of the chemical property of their springs is to have SO_4 ions four times as Cl content. In connection with this characteristic, it is interesting to remember the studies of volcanic ash by Miyake (**11**), Noguchi (**12**), and Iwasaki (**13**), who reported that there are much SO_4 and little Cl in the soluble component of volcanic ashes from Aso, Asama, Kusatsu-Shirane and Izu-Mihara volcanoes.

The hot springs in the high ground of northern Atami, marked with "△" in Fig. 5, have also a little chemical constituent and a large value of the deviation, and the ratio of some chemical components is shown in Fig. 6 (c), which differs somewhat from Fig. 6 (b). Chemical constituents of both hot springs in the south-western part and the northern high ground may be secondary, dissolved from the formation, since these springs have low temperature and less constituents.

Finally, the hot springs in the central region have the type of chemical composition as shown in Fig. 6 (d), and are marked with "×" in Fig. 5. They have the deviation less than 100, and their constitution resembles to that of the sea water, compared with other springs in Atami. Yazima (**14**), Honda and Terada (**15**) suggested that the origin of chlorine of these springs may come from the sea water, but, at the present time, it is difficult to prove it.

5. Summary

(1) Hot springs in the central region of Atami have the temperature of about 100°C, and much Cl and few SO_4 ions. These results are similar to those observed in 1936, but the activity of these hot springs becomes slightly weak, since the less sulphate area characterizing the central region becomes narrower.

(2) Hydrostatic pressure of the greater part of hot springs in the central region is larger than that of the sea water, and at present the sea water filtering into these springs should not occur. However, a few springs on the beach of the central region have a tendency of decreasing temperature and increasing Cl content, and their pressure is less than that of the sea water, so they may be contaminated by the water, and it was also proved from their chemical constituent.

(3) It becomes clear that the hot springs near and at the south of the mouth of Wada River are contaminated by the sea water, because their temperature decreases and their Cl content largely increases in comparison with the past state. Chemical constituent of these springs differs from that of the sea water, but the difference is explainable when the dissolving $CaSO_4$ and the cation exchange in underground are considered together with the sea water intrusion. This intrusion may be caused by the over-pumping.

(4) Hot spring in the south-western part and northern high ground of Atami have a little chemical constituent. It seems that their dissolved matter probably comes from the volcanic formation of this area. Some hot springs on the northern beach of Atami may also be contaminated by the sea water, since their Cl ions have been increasing in recent years.

(5) According to the pressure distribution of hot springs in the central region, it seems that the hot water comes through fissures from deep ground and spreads in an aquifer, which may be artesian, because there are some flowing springs in this region.

PART II. WATER LEVEL FLUCTUATION IN A HOT-SPRING WELL

6. Information about an observed well and method of observation

In Atami, most wells are pumped by air-lift-pumps of 2~20 horse-powers, but only one well named "Nagisa" is suitable for water-level observation, which is on the reclaimed ground 4.5 m above sea-level and 60 m from the sea-shore. On account of comparatively low temperature of 43°C, it has not been used. Underground geological condition around this well are unknown, but it appears from the general geology of the surroundings that the well penetrates into the "Yugashima group" and the hot water comes from the strata.

To measure the water level fluctuation in the well, Richard's automatic tide gauge was used, its reduction rate being 1/30. Observation continued from September 1954 to December 1955. Some examples of the record are shown in Figs. 9, 11, 12, 14 and 15. The water level in the well can be expressed by the following relation:

$$W_t = W_0 + aT_{t-\alpha} + bP_t + R + A, \qquad (1)$$

where

W_t = water level in the well at time t (cm),
W_0 = mean water level in the well (341 cm above a datum level and 319 cm below the ground surface),
$T_{t-\alpha}$ = deviation of sea level from the mean at time $(t-\alpha)$ (cm),
a = tidal efficiency of the water level in the well,
α = time lag between changes of the water and the sea levels,
P_t = change of atmospheric pressure from the mean at time t (cm of water column),
b = barometric efficiency of the water level in the well,
R = term of precipitational effects,
A = term of interference-effects produced by starting and stopping pumps of neighbouring wells.

The time lag of effect of barometric change is not found on the records, as the apparatus used is not so sensitive as to record a sharp barometric change.

In the following discussion the tidal data at Itō and the barometric and precipitational data at Aziro are used. Though Itō is at a distance of 15 km and Aziro is at a distance of 7 km from Atami, there may be not so large errors in using these records, when the general tidal and barometric effects are considered. As the data of A, driving conditions of air-lift-pumps in city-owned wells are used. On the other hand, there are many private wells and their discharges are generally smaller than those of the city-owned wells. Thus, it is enough to use the data of the city-owned wells in the first stage of discussion of the effect of pumping.

7. Tidal effect on the water level in the well

When there are little changes in the atmospheric pressure as well as in the driving condition of pump and there is no precipitation, then P_t, R and A are zero. Thus we have

$$W_t - W_0 = aT_{t-\alpha}. \qquad (2)$$

Periods in which the above conditions were satisfied are June 28~July 2, July 4~6

and July 12~17, 1955. In these periods, comparing $W_t - W_0$ with T, we can estimate the tidal efficiency "a" and the time lag "α". Fig. 8 shows the relation between the tide level and the corresponding water level in the well, at the maximum and the minimum. The tidal efficiencies are calculated by the method of least squares and the mean value is $0.495 \fallingdotseq 0.5$.

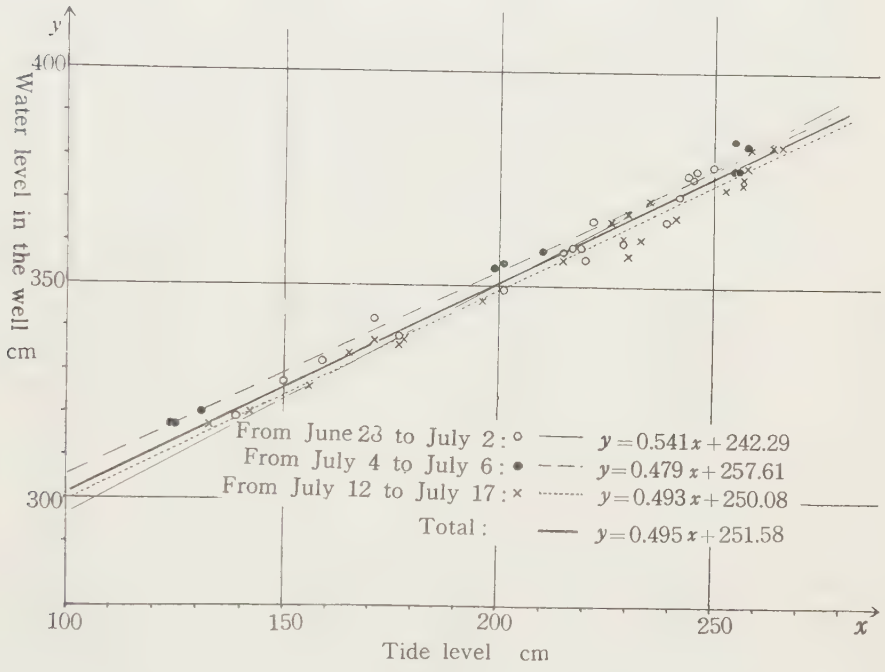
y
400
350
300
Water level in the well
cm
From June 23 to July 2 : ○ —— y = 0.541x + 242.29
From July 4 to July 6 : ● – – – y = 0.479x + 257.61
From July 12 to July 17 : × ····· y = 0.493x + 250.08
Total : —— y = 0.495x + 251.58
100
150
200
250
x
Tide level cm

Fig. 8. Relation between the tide level and the water level in the well.

When we consider the time lag, the eight-day clock of the apparatus was replaced by a one-day clock and the time check was marked electrically every hour from August 5 to August 9, 1955. Thus the time errors can be kept to a few minutes. The times of appearance of the maximum and minimum water level are compared with those of the tidal records, as in Table 2. Phase lag ranges from 20 to 95 minutes and the means is about 60 minutes. The variation of phase lag of apparent tidal effect is caused by the tidal wave constitution. When the effects of tide move in an aquifer, each component reduces its own amplitude and delays its own phase, then the resultant wave of these components is observed in a well as a water level record. The harmonic analysis of the tide and the water level was done by Darwin's method in a period from January 1 to January 29, 1955, and the result is shown in Table 3.

Table 2.

Date		Time of appearance: Water level in tbe well	Time of appearance: Tide	Time difference of the appearance
		h m	h m	minutes
Aug. 5	Min.	13 00	11 45	75
	Max.	19 30	18 25	65
Aug. 6	Min.	1 00	0 00	60
	Max.	7 00	5 40	80
	Min.	13 30	12 15	75
	Max.	19 30	18 45	45
Aug. 7	Min.	1 40	0 35	65
	Max.	7 25	6 25	60
	Min.	13 40	12 40	60
	Max.	20 40	19 05	95
Aug. 8	Min.	2 10	1 05	65
	Max.	8 20	7 05	75
	Min.	14 00	13 20	40
	Max.	20 30	19 45	45
Aug. 9	Min.	2 20	2 00	20
	Max.	9 00	7 55	65
	Min.	14 40	13 50	50
			Mean	61

Table 3.

	M_2		S_2		K_1		O_1	
	H_m	κ_m	H_s	κ_s	H'	κ'	H_0	κ_0
	cm	°	cm	°	cm	°	cm	°
Tide	35.4	145.1	17.1	179.4	22.1	176.5	18.3	155.3
Water level in the well	13.7	168.1	7.9	204.3	12.0	195.2	10.1	180.0
(Water level)/(Tide level),	0.39	—	0.46	—	0.54	—	0.55	—
(Water level)-(Tide level), degree	—	23.0	—	24.9	—	18.7	—	24.7
(Water level)-(Tide level), minute	—	48	—	50	—	75	—	106

8. Effect of barometric pressure change on the water level

As cyclones and fronts accompany the rain, it is difficult to pick up the case of pressure change without rainfall from the actual record. Thus, we were obliged to take the data of February 20, 28 and October 11, 1955, when it was raining. An example of the record of the water level is shown in Fig. 9, together with tidal and barometric curves. The records should include the effect of precipitations, but it may be negligible as shown in a subsequent section. When in

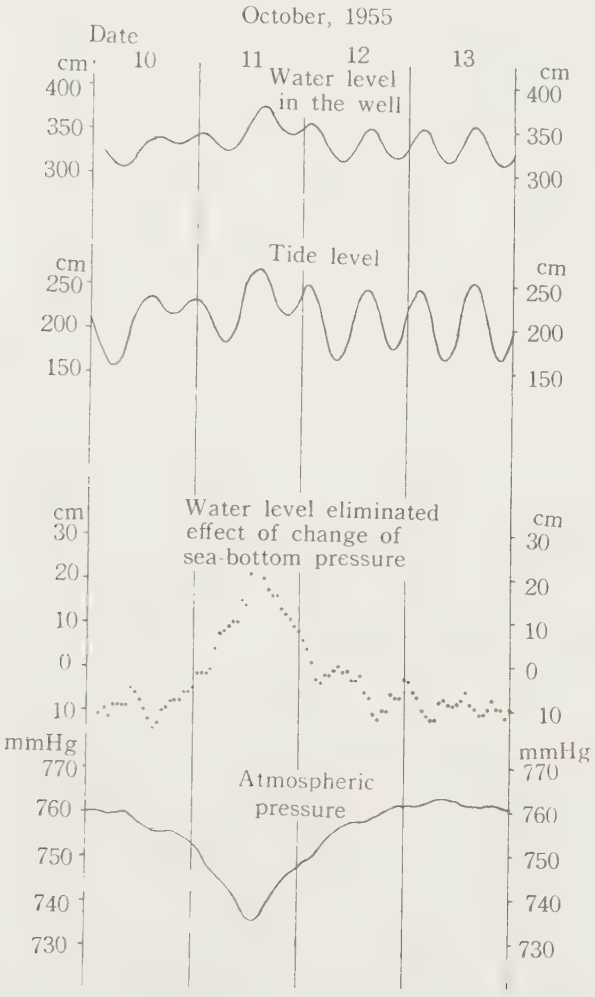

Fig. 9. An example of the effect of the atmospheric pressure change on water level in the well.

Eq. (1) both A and R are nearly zero, we have

$$W_t - W_0 - aT_{t-\alpha} = bP_t . \qquad (3)$$

The left-hand side of this equation shows the water level change from which the tidal effect is eliminated, and it may be calculated with the values of a and α of the former section. For the discussion of the effect of barometric pressure change on the water level in a well, we must divide it into three elements which are on the sea-surface, the ground-surface and the water-surface in the well, but the last two elements are usually discussed as one. The increase of atmospheric pressure on the sea-surface causes descent of the sea-level, but this compensation

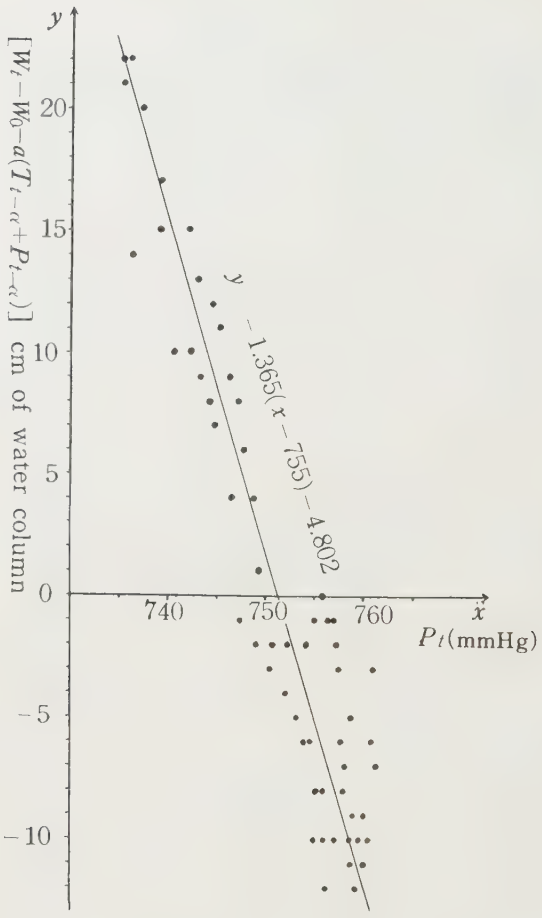

October 11 and 12, 1955

Fig. 10. An example of the relation between the water level eliminated effect of change of sea-bottom pressure, $W_t - W_0 - a(T_{t-\alpha} + P_{t-\alpha})$, and the atmospheric pressure, P_t.

Table 4.

	b'	
	cm of water column / mm Hg	cm of water column / cm of water column
1955,		
Feb. 18~20	−1.148	−0.845
Feb. 26~28	−1.574	−1.158
Oct. 10~12	−1.365	−1.003
Mean		−1.002

is usually imperfect and the increase of atmospheric pressure may bring about the increment of sea-bottom pressure, and then the water level in the well may ascend at the flood tide. Thus, the effect of atmospheric pressure change may be written as:

$$bP_t = aP_{t-\alpha} + b'P_t . \qquad (4)$$

The first term on the right-hand side of Eq. (4) shows the effect on the sea-surface, so that the damping rate a and the phase lag α are nearly equal to those in the tidal effect. The second term shows the effect on the ground-surface and the water-surface. Thus, Eq. (3) is expressible as follows:

$$W_t - W_0 - a(T_{t-\alpha} + P_{t-\alpha}) = b'P_t . \qquad (5)$$

The values of the left-hand side of Eq. (5) may be calculated with a and α which are given in the former section, and their variations are also plotted in Fig. 9. The value of b' is determined from Fig. 10 by the method of least squares, and is listed in Table 4 together with other examples, the mean value being -1.00. The "barometric efficiency" in other papers corresponds to b used here, and it follows from Eq. (4) $b \fallingdotseq a + b' \fallingdotseq -0.5$. The relation $b' \fallingdotseq -1$ shows that the pressure change on the ground-surface does not affect the water level in the well, and that the aquifer is nearly rigid.

9. Annual variation and effect of precipitation on the water level

If the discharge rate of the hot water from the aquifer is equal to the recharge rate, the pressure of the hot spring should be kept at a constant value. When the discharge exceeds the recharge, the head of the hot ground water falls gradually, and then the head will be settled at a level when the discharge and the recharge are balanced. On the other hand, when the discharge is less than the recharge, the head will rise.

In Atami, with the increase of the discharge from the aquifer, the head of the hot ground water has decreased. Total discharge rate is at present about $9 \cdot 10^3$ m^3/day (**19**), and it is important to know whether this discharge is over or under the recharge, the secular variation of the mean head of the hot ground water being helpful to know. We average the values in 24 hours to compare with the daily data of the atmospheric pressure and the precipitation, and the effect of tide may also be nearly eliminated.

Fig. 11 shows daily means of the water level of the Nagisa well, the sea level and the atmospheric pressure*. The water level from which both tidal and

* It is based on Monthly Report, C. M. O., Japan, and somewhat differs from the data shown in other figures as it is reduced to the mean sea level.

barometric effects with the same coefficients as given before are eliminated is also shown in Fig. 11. They denote the annual variation which is low in winter and high in summer, but neither monotonously decrease nor increase. This suggests that the recharge and discharge of the aquifer are nearly balanced through a year. A main cause of the annual variation is generally the precipitation, but, as shown in Fig. 11, the daily mean of the water level has no reliable correlation, and the effect of precipitation upon this well seems to be not so remarkable. Furthermore, in order to pay attention to the effects of short periods, the hourly water level, from which both tidal and barometric effects are eliminated, is calculated during several days before and after December 19, 1954, as well as during several days before and after February 27, 1955, when there was respectively a solitary rain. The result is shown in Fig. 12, in which we cannot find the

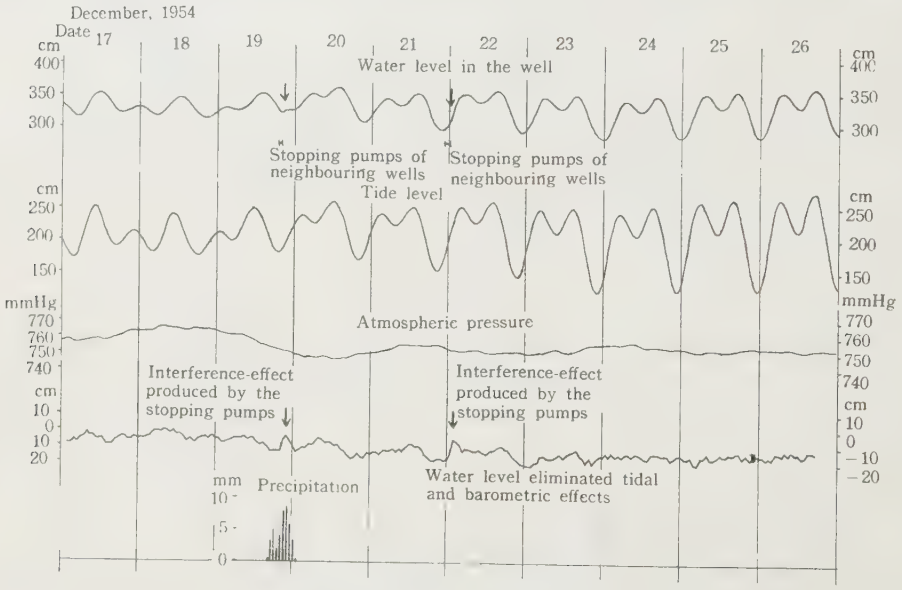

Fig. 12. Water level in the well and other factors during several days before and after Dec. 19, 1954.

ascent of head for the precipitation. Finally, the effect of precipitation upon this well seems to be very small, and it coincides with the result of study in Beppu (**20**) where the hot springs near the sea-shore were scarcely affected by the precipitation. Annual density variation of sea water contributes to annual pressure change at the sea bottom, but, by this effect, sea-bottom pressure is greater in winter and smaller in summer than that calculated from the sea level (**21**). Therefore the annual variation of the well-water level is also inexplicable by this density variation,

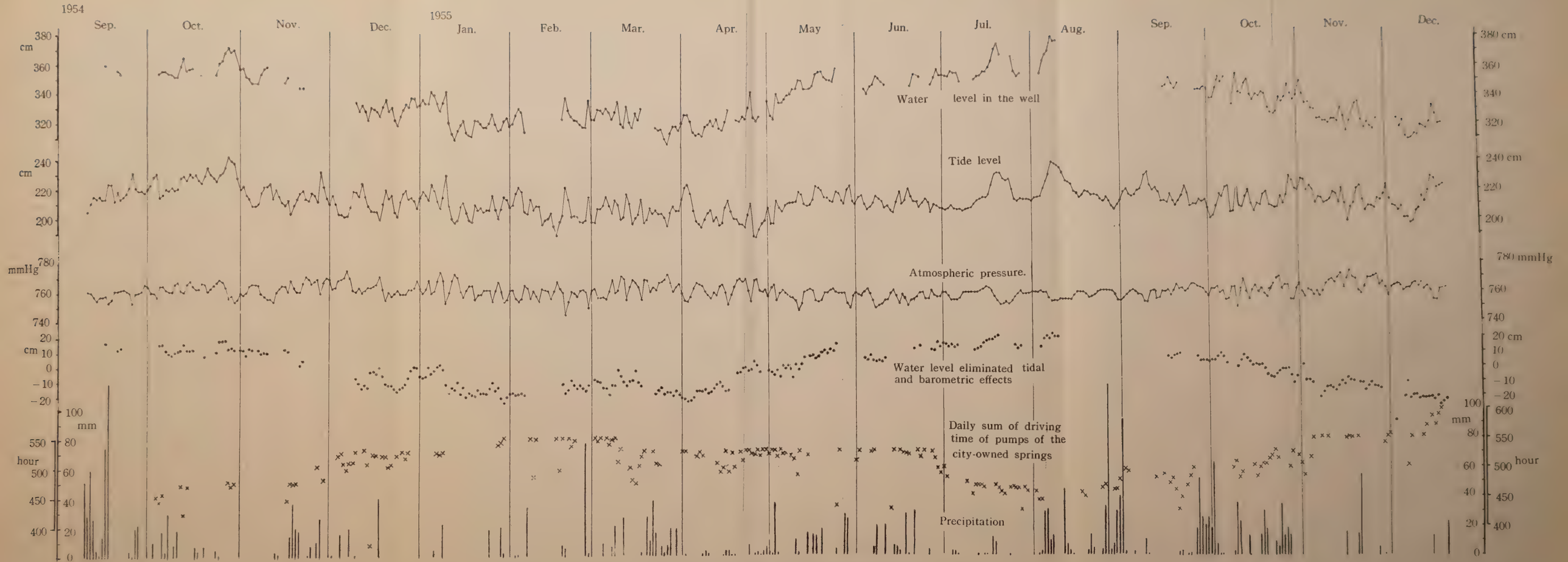

Fig. 11. Daily means of water level in the well and other factors.

Daily sums of driving time of pumps of city-owned springs are registered by Atami Municipal Office and also shown in Fig. 11. They have reciprocal correlation with the annual water-level variation, being approximately an index of annual variation of total discharge from the aquifer. Thus, the annual variation of head shown in Fig. 11 seems to be related to the change in the discharge.

10. Interference-effect produced by starting and stopping pumps of neighbouring wells upon the water level in the observed well

During this observation period, remarkable changes of the water level in the Nagisa well were found and they were inexplicable by the effects of tide, atmospheric pressure and precipitation, but related with starting and stopping pumps of other wells.

There are several hot springs near the Nagisa well as shown in Fig. 13. It is important to know which springs interfere with the Nagisa well. In Beppu (**22**), some springs are affected by adjacent wells and others by rather distant wells, and the extent and the direction of the interference are indeterminate. To search for the well of which discharge affects the head of the observed well, we examined the abnormal changes on the water level record, comparing

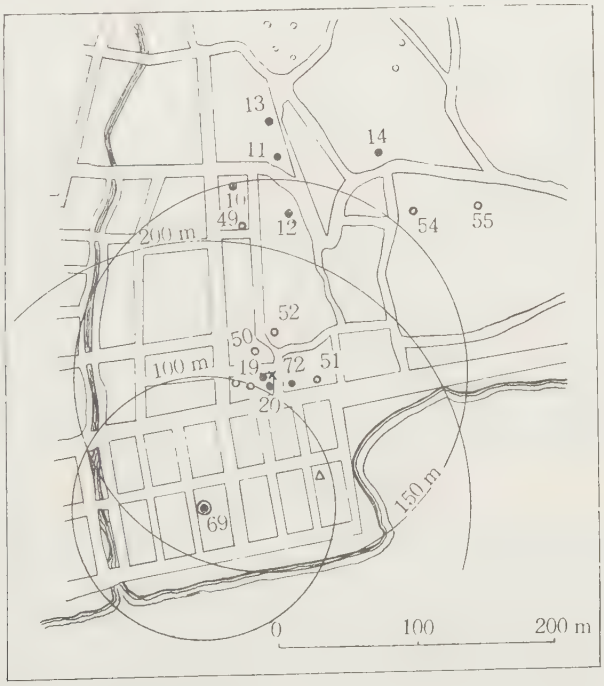

Fig. 13. Distribution of hot springs near "Nagisa well"; ●, municipal well; ○, private well; ⊙, observed well; △, a well under drilling; ×, assumed representative well.

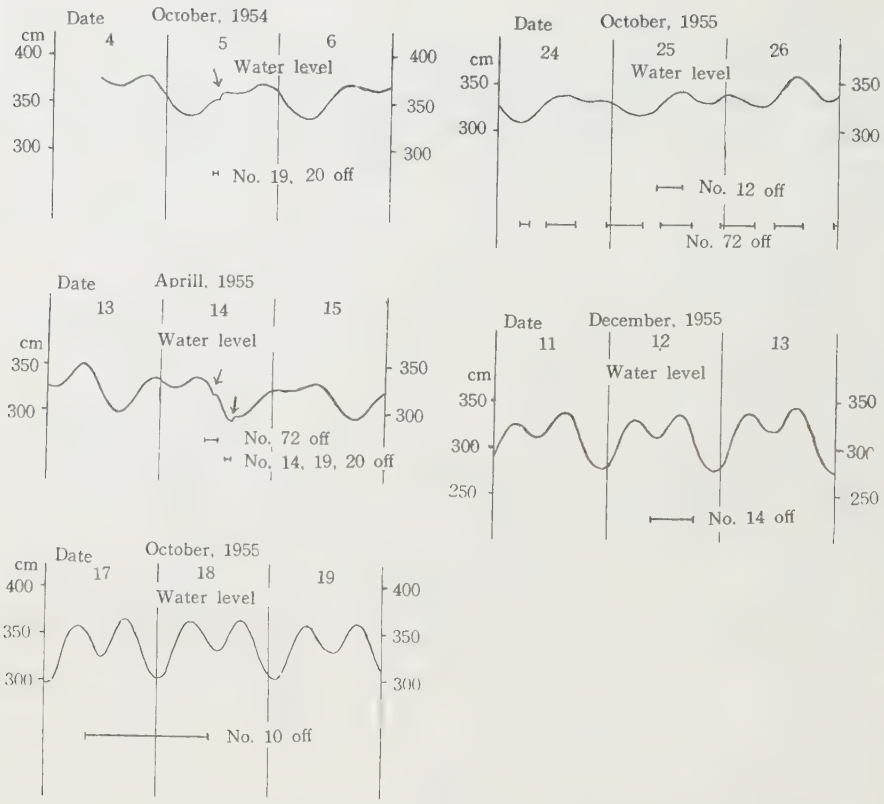

Fig. 14. Relation between water level in the observed well and stopping pumps of neighbouring wells.

with driving condition of pumps installed in neighbouring city-owned wells. Some examples are shown in Fig. 14, from which it appears that No. 19 and No. 20 wells affect greatly the head of the Nagisa well, and No. 10, No. 12 and No. 14 do not affect at all and No. 72 does sometimes. The driving conditions are registered only for the city-owned wells and not for the private wells, but the head of the Nagisa well must be affected by the change in pumping condition of both city-owned and private wells in a limited area where No. 19, No. 20 and No. 72 wells exist.

An example of the observed abnormal change is shown in Fig. 15. The lowest row of this figure gives true interference-effect reduced by eliminating tidal and barometric effects from the record of the water level. Rise and fall of the water level occurred simultaneously with stopping and restarting the pumps of neighbouring wells. The quantitative relation between the rate of discharge and the water-level change may be connected with the property of the aquifer, and will be discussed in the next section.

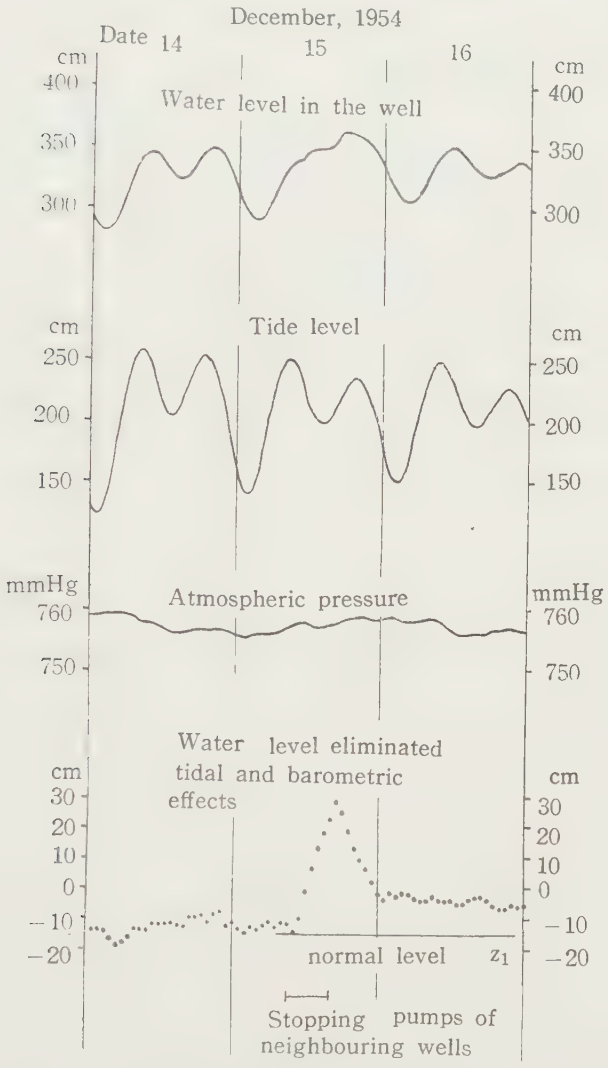

Fig. 15. An example of the interference-effect produced by stopping pumps of neighbouring wells on the water level in the well.

11. Physical properties of the aquifer in the central region of Atami

The region extending from the Nagisa well to the west is called "the central region of Atami" as described above. Hot-spring wells in this region seem to be in the same aquifer, because they closely resemble in chemical and hydrological properties. The aquifer is in "Yugasima-group" described in section 1. This group has no sand stratum but a great many large and small fissures, so its permeability can be assmed to be uniform enough to regard it as a nearly

homogeneous aquifer (**2**). It may also be artesian, because there are a few flowing hot springs in this region.

It is of interest to know whether the aquifer is connected with the sea or not, and we can find some informations about this problem: (1) for the hot springs of which pressure is less than that of sea water, the temperature decreased and the Cl content increased; (2) if the aquifer is not connected with the sea, the tidal effect upon the well is produced by the tidal load change on the sea bottom through the impermeable formation to the aquifer, but it is contradictory to the former result that the aquifer is nearly rigid; (3) it is also said that there are springs in the bottom of the Atami Bay (**14, 19**). Thus, the aquifer is regarded to be directly connected with the sea. If some additional conditions are assumed for the aquifer, we can lead its transmissibility and coefficient of storage. These conditions are as follows.

(a) The aquifer is homogeneous, isotropic and horizontal, and its thickness is uniform.

(b) When the interference-effect is considered, the aquifer is regarded as a horizontally infinite layer, while the real range is about 1 km^2.

(c) When pumping of a well is continuous, the head distribution of the neighbourhood is able to reach the nearly steady state, that is, the discharge from the aquifer is compensated by the recharge from the outside. This assumption is necessary only for the discussion of interference-effect, and unsuitable for a long period, because the head of Atami hot springs has fallen gradually in recent years.

Most hot water in Atami is forced out by air-lift-pumps. When pumping is continuous at a constant discharge, the water level in the observed well would be kept in steady state from the assumption (c), and then if the pumping stops, the water level will rise. In this case, the stopping of pumps is equivalent in mathematical treatment to the starting pump of negative discharge, $-Q$, over the continued positive discharge, Q. Thus, applying Theis' theory (**23**), we can express the water level in the observed well with the assumptions (a) and (b), that is,

$$z - z_1 = \frac{Q}{4\pi kD} \int_{\lambda}^{\infty} \frac{e^{-\lambda}}{\lambda} d\lambda , \qquad (6)$$

where z_1 = water level, from which tidal and barometric effects are eliminated, in observed well before stopping pump,

z = water level, from which tidal and barometric effects are eliminated, in observed well after stopping pump,

Q = rate of discharge,

k = permeability,

D = thickness of the aquifer,

$\lambda = \frac{r^2 S}{4kDt}$,

r=distance from pumped well to observed well,

S=coefficient of storage,

t=time elapsed from the stopping of pump.

When $\lambda \ll 1$, it follows approximately

$$z - z_1 \fallingdotseq \frac{Q}{4\pi kD}\left(\ln\frac{4kDt}{r^2 S} - 0.577\right), \qquad (7)$$

and this approximation holds roughly when $t > 2$-hours as seen in Fig. 16. Eq. (6) or Eq. (7) shows the behaviour of water level in the observed well at a distance r from a pumped well. In practice, there are some pumping wells which affect the water level of the Nagisa well, but it is permissible to imagine a representative well for the actual wells, because they are in a limited area. The relation between t and $z - z_1$ is given from the data as shown in Fig. 15, and illustrated semi-logarithmically in Fig. 16.

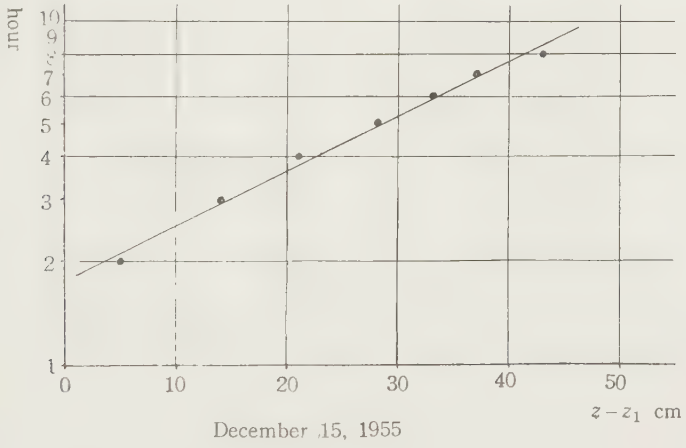

Fig. 16. An example of the relation between t and $z - z_1$.

After the restarting pump with the same rate of discharge Q, putting the period of the stopping as t_1, we get

$$z - z_1 \fallingdotseq \frac{Q}{4\pi kD}\ln\frac{t}{t - t_1}. \qquad (8)$$

The relation between $\frac{t}{t - t_1}$ and $z - z_1$ is shown in Fig. 17.

According to the investigation of the Atami Municipal Office, the sum of actual discharge rates of some wells in the limited area, Q, was 600 l/min in December, 1954 and r is about 200 meters. The values of T and S are calculated

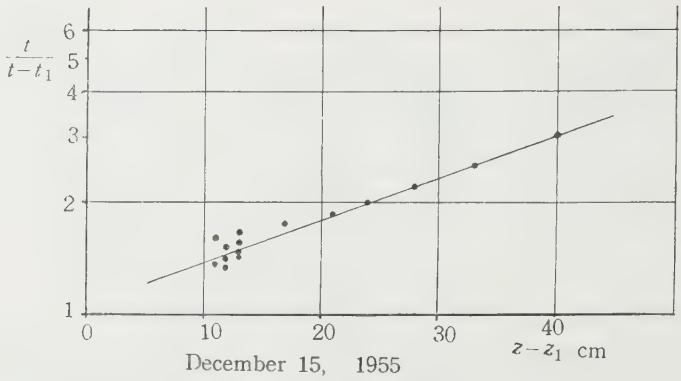

Fig. 17. An example of the relation between $\frac{t}{t-t_1}$ and $z-z_1$.

Table 5.

		$T=kD$ cm²/min	S (1)	S (2)	S (3)
Dec. 15, 1954	Case of stopping pump	1750	1.7×10^{-5}	1.5×10^{-5}	2.6×10^{-5}
	Case of restarting pump	1232	—	—	—
Mar. 10, 1955	Case of stopping pump	2545	2.2×10^{-5}	2.9×10^{-5}	2.3×10^{-5}
	Case of restarting pump	4100	—	—	—
Dec. 7, 1955	Case of stopping pump	3220	1.4×10^{-5}	1.1×10^{-5}	1.1×10^{-5}
	Case of restarting pump	2025	—	—	—
Mean of all values		2600			2.0×10^{-5}

(1) Calculated with "T" for stopping pump.
(2) Calculated with the mean of both"T" for stopping and restarting pump.
(3) Calculated with the mean of all "T".

by the method of least squares, and these results are shown in Table 5. The cause of disagreement of these results may be ascribed to the uncertainty of z and Q, and that the assumptions used may not be completely accurate. Finally, $T=kD=2600$ cm²/min and $S=2.0\times10^{-5}$ are given in round numbers.

In § 8, we regarded the aquifer as rigid from the result that the pressure change on the ground surface does not affect the water level in the well. On the other hand, the aquifer seems to have elastic characteristics, because the water level variation obeys Theis' equation. This means that the water in the aquifer is compressible and the permeable medium of the aquifer is nearly incompressible. Jacob (24) introduced, in his elastic theory, the coefficient of storage as

$$S = \rho g D\left(\frac{\theta}{E_w} + \frac{p}{E_s} + \frac{\theta q}{E_c}\right), \tag{9}$$

where ρ is the density of water, g the acceleration of gravity, θ the porosity of the medium of which the aquifer is composed, p the negative ratio of a given change in compressive stress to the change in hydrostatic pressure producing it, q a dimensionless quantity of clay intercalated in the aquifer, and E_w, E_s and E_c are moduli of elasticity of the water, the solid skeleton and the clay, respectively. When the aquifer is rigid, Eq. (9) may be reduced to

$$S = \rho g D \frac{\theta}{E_w}. \tag{10}$$

Substituting in Eq. (10) $S=2.0\times10^{-5}$, $\rho=1\,\mathrm{g/cm^3}$, $g=980\,\mathrm{cm/sec^2}$ and $\frac{1}{E_w}=48.9\times10^{-12}\,\mathrm{cm\cdot sec^2/g}$, we get $D\theta=4.2\times10^2\,\mathrm{cm}$. Since θ is unknown, the value of D is not determined, but the order of D presumed with the probable θ may be from 10^3 to $10^4\,\mathrm{cm}$.

We can also estimate the physical properties of the aquifer from the tidal effect. When the above conditions (a) and (b) are assumed, the problem can be treated as one-dimensional wave propagation. If the amplitude and the phase of tidal wave are given by H_T and κ_T, and those of water-level fluctuation by H_W and κ_W, we can introduce the next relation like Ferris' equation (25):

$$H_W \cos(nt-\kappa_W) = H_T e^{-x\sqrt{\frac{nS}{2T}}} \cos\left((nt-\kappa_T-x\sqrt{\frac{nS}{2T}}\right), \tag{11}$$

where n is the velocity of each tidal component, x the distance from a point where the aquifer is in contact with the sea, and S, T and t are the coefficient of storage, transmissibility and time respectively. Thus,

$$\frac{H_W}{H_T} = e^{-x\sqrt{\frac{nS}{2T}}}, \tag{12}$$

and

$$\kappa_W-\kappa_T = x\sqrt{\frac{nS}{2T}}. \tag{13}$$

We can, therefore, calculate the values of $x\sqrt{\frac{S}{T}}$ and x, and the results are shown in Table 6. The distinct discrepancy between the value calculated from Eqs. (12) and (13) may be caused by a simplification of the natural complex situation to a simple model for mathematical treatment. Thus, according to a rough estimation, the aquifer may be in contact with sea at a place on sea bottom from 0.7 to 1.7 km off-shore.

Table 6.

(a) Calculated with the ratio of amplitude.

Tidal component	$\frac{H_W}{H_T}=e^{-x\sqrt{\frac{nS}{2T}}}$	$x\sqrt{\frac{nS}{2T}}$ (radian)	x (cm)
M_2	0.39	0.904	1.65×10^5
S_2	0.46	0.776	1.34
K_1	0.54	0.615	1.50
O_1	0.55	0.597	1.51

(b) Calculated with the phase lag.

Tidal component	$\kappa_W-\kappa_T$	$x\sqrt{\frac{nS}{2T}}$ (radian)	x (cm)
M_2	23.0	0.401	0.71×10^5
S_2	24.9	0.435	0.75
K_1	18.7	0.326	0.80
O_1	24.7	0.431	1.09

12. Summary

(1) Tidal effect on the observed well of hot ground water is obvious, and the tidal efficiency is about 0.5 and the phase lag about one hour.

(2) Water level in the well rises with the barometric pressure decrease and falls with its increase. The barometric efficiency is about 0.5 and the phase lag is very small. The barometric pressure change affects the water level through the sea and the well directly, but not the ground surface, and this means that the permeable medium of the aquifer may be rigid.

(3) The water level is high in winter and low in summer, but the effect of precipitation upon the well is inappreciable. The cause of this annual variation seems to be the seasonal variation of the total pumping rate of Atami hot springs. Therefore, the head of hot ground water in Atami will fall more and more with future exploitation.

(4) The interference-effects produced by starting and stopping pumps of neighbouring wells upon the observed well are very noticeable. The hot springs in the central region of Atami are closely connected with each other, and may be in the same aquifer.

(5) The aquifer may be regarded as a confined one, and its transmissibility is about 2600 cm^2/min, its coefficient of storage about 2.0 10 ^{5}, and the order of the thickness of the aquifer may be from 10^3 to 10^4 cm.

(6) The aquifer seems to be in contact with the sea at a certain place on sea bottom from 0.7 km to 1.7 km off-shore.

Acknowledgements

The writer wishes to expess his sincere thanks to Dr. K. Seno for his kind guidance and to the members of the Atami Municipal Office for their heartly co-operation to this study. The writer is also greatly indebted to Mr. F. Itō, a member of Itō Meteorological Station, for his kindness in copying meteorological and tidal data. The cost of this study was partly convered by a research grant from the Ministry of Education.

REFERENCES

1. Y. Ōtuka and H. Kuno; Bull. Earthq. Res. Inst., **10** (1932), 472.
2. Y. Ōtuka; Zisinkenkyusho-Ihō, No. 21 (1943), 414 (in Japanese).
3. T. Fukutomi; Bull. Earthq. Res. Inst., **15** (1937), 113.
4. T. Kamizu; Chigakuzasshi, No. 287 (1912), 754 (in Japanese).
5. M. Yokoyama; ditto, No. 323 (1915), 915 (in Japanese).
6. M. Yokoyama; ditto, No. 463 (1927), 497 (in Japanese).
7. K. Seno; Tikyubuturi, **7** (1943), 131 (in Japanese).
8. The Welfare Ministry; Nippon Kōsen-shi, (1954), 376 (in Japanese).
9. H. Kuno; Explanatory text of the geological map of Atami, (1952), 23.
10. S. K. Love; Trans. American Geophy. Union, (1944), 951.
11. Y. Miyake; J. Met. Soc. Japan, **16** (1938), 89 (in Japanese).
12. K. Noguchi; J. Chem. Soc. Japan, **59** (1938), 1225 (in Japanese).
13. I. Iwasaki; ditto, **57** (1936), 255 (in Japanese).
14. E. Yazima; Chigakuzasshi, No. 198 (1905), 415 (in Japanese).
15. K. Honda and T. Terada; Publ. Earthq. Invest., **4** (1906), 51.
16. K. Honda; ditto, No. 18 (1904), 73.
17. K. Maeda; Jishin, **6** (1934), 275 (in Japanese).
18. M. Morita; ditto, **7** (1935), 395 (in Japanese).
19. Atami Municipal Office; "Atami", 1953 (in Japanese).
20. K. Seno; Jap. J. Astron. Geophy., **17** (1940), 265.
21. T. Nomitsu and M. Okamoto; Mem. Coll. Sci., Kyoto Univ., Ser. A, **10** (1927), 125.
22. K. Seno and K. Yamashita; Tikyubuturi, **8** (1950), 1 (in Japanese).
23. C. V. Theis; Trans. American Geoph. Union, (1935), 519.
24. C. E. Jacob; ditto, (1940), 574.
25. J. G. Ferris; I.U.G.G., Ass. Gene. Bruxelles, (1951), 148.

Memoirs of the College of Science, University of Kyoto, Series A,
Vol. XXIX, No. 3, Article 4, 1961.

DROP PRODUCTION BY BURSTING OF AIR BUBBLES ON THE SEA SURFACE (III) STUDY BY USE OF A WIND FLUME

BY

Yoshiaki TOBA

(*Received December 27, 1960*)

ABSTRACT

Experiments on the air entrainment in wind waves and the drop production from them, are carried out by use of a wind flume, 21 m long. A new mechanism of the air entrainment, that is caused by instability of small waves which override gravity waves and in which the surface tension exerts to a considerable degree, is first observed. The lowest wind speed for the occurrence of this process is about 13 $m \cdot sec^{-1}$ (at 10 m level), which is considered to be one of the important critical wind speeds for air-sea boundary processes. Small droplets measured in the air above wind waves are confirmed to be produced by bursting of the air bubbles entrained in wind waves. Concentration-size distribution of the droplets in the air directly above the sea surface and density-mass distribution of sea-salt nuclei at various heights, are derived, by theoretical treatment, from the results of the experiment. After some modification, the latter nearly represents the actual distribution of giant sea-salt nuclei in the atmosphere. The rate of production of droplets of each size grade, estimated by the experiment, is ensured also by comparison with an observation of salt fallout near the coast. Dependence of the rate on wind speed also agrees with the field observation. Distribution of the entrained air bubbles in wind waves is measured, and the coefficient of mixing in wind waves is estimated from it.

1. Introduction

Part of the atmospheric condensation nuclei, especially giant salt nuclei which grow to droplets that can initiate rain from warm clouds, are believed to originate from the ocean surface. Further, it is presumed that sea water droplets which become salt nuclei are not large splashing water from wave crests, but are small droplets produced when air bubbles burst at the sea surface. Studies on the drop formation, by bursting of each bubble at sea water surface, has been made by several investigators (**1**, **2**, **3**, **4**, **5**, **6**, **7**, **8**, **9**). These investigations show that smaller bubbles eject droplets, having diameters of ten and odd percents of original bubbles, through disintegration of water jet formed upon collapse of a bubble cavity, and also that bubbles larger than a few mm produce comparatively many droplets of a few tens micron, through shuttering of the bubble film.

However, as to the actual process of entrainment of air bubbles in sea water and the drop formation from them, few studies have been made so far. Merely, D. J. Moore and B. J. Mason (5) caught droplets in the air flow above sea water in a wind-wave tunnel 6 m long; and D. C. Blanchard and A. H. Woodcock (7) measured the size and rate of rise of small bubbles in sea water, at the surf zone after a breaking surf passed and large bubbles rose to the water surface, and estimated the rate of formation of droplets through disintegration of jets from the bubbles.

In order to know the rate of supply of sea-salt nuclei into the upper air, it is first necessary to know the rate of production of sea water droplets at the air-sea boundary, or the distribution of the droplets in the atmosphere very near the boundary. Especially, quantitative as well as qualitative research of such dramatic phenomena like the entrainment of air bubbles in wind waves and droplet production from them, must be also in themselves part of the most important problems in the air-sea boundary processes. So a comprehensive experiment on the problem has been carried out, by use of a wind flume of a comparatively large scale, and a series of theoretical considerations has been made in connection with the actual distribution of sea-salt nuclei in the atmosphere, as well as with the salt fallout near the coast.

In the experiment, tap water was used, instead of sea water, to protect the installations from damage. There might be, in consequence, some discrepancy between the results and the real phenomena at the air-sea boundary. But, so far as the essentials of the physical processes are concerned, serious deviations would not be found in the results.

2. Procedure and condition of experiment

2.1. Procedure of experiment

The wind flume used is set up at Ujigawa Hydraulics Laboratory of Disaster Prevention Research Institute, Kyoto University. The flume part is 21.6 m long, 0.75 m wide, 1.02 m high, containing fresh water 0.5 m deep, the side walls being made of polished glass. The wind is uniformly rectified through wind tunnel 8.6 m long and wind speed at the entrance to the flume varies from 0.5 up to 12.1 $m \cdot sec^{-1}$. Reflection of waves is prevented by a gentle bottom slope at the end of the flume, while an effort is made to remove surface contamination by draining the surface water over the bottom slope at the end of the flume.

Room temperature was between 10 C and 19 C, while water temperature was between 10 C and 18 C, humidity having been between 86 percent and 57 percent, in the course of the present experiment.

Methods of measurement of various elements were as follows.

(i) *Distribution of wind speed*

Wind speed profiles were measured by use of a miniature anemometer of Robinson type, up to the height of 35 cm above the undisturbed water surface, at 4.5 m, 6.9 m, 10.0 m and 13.6 m in fetch. The mean wind speed in the cross section of the wind tunnel was also measured at the entrance to the flume.

(ii) *Elements of wind waves*

Wave form was registered by an ink-writing oscillograph connected with a resistance type wave-meter of H. Kunishi (**10**), at the above-mentioned four fetches. Period and height of waves were read on the records, and the wave length was calculated from the wave period, by the well-known formula for surface waves, in which the surface tension is also taken into account.

(iii) *Bubbles*

The room was darkened and bubbles were photographed under an illumination. A camera was set at a fixed distance of 1 m or 60 cm from the glass wall, and the focus was arranged at 3 cm inside the wall. The depth of the focus was 3.5 cm or 1.3 cm, respectively. Bubbles on photographs were read, by use of a moving microscope with an arranged scale. Bubbles in water were not round but flat, so that vertical and horizontal diameters were read for each bubble and converted into an equivalent diameter, by assuming the bubble shape to be an ellipsoid. Motion pictures (64 frames per sec) and stereographs of bubbles entrained in wind waves, were also taken at a fetch of 10 m.

(iv) *Droplets*

Droplets larger than 100μ were caught by a dye-treated filter paper 2 cm wide, held vertical and normal to the wind. Method of the measurement is referred to Y. Toba (**11**). For smaller droplets, a glass slide 5 mm wide coated with MgO (**12, 13, 14**) was adopted. The ratio 0.86, between the droplet diameter and the diameter of the crater made by it, was used. For droplets of 150~250μ and 250~350μ, both methods gave equivalent results, while for droplets of 100~150μ, results by filter paper seemed to be unreliable, so that only results by glass slides were adopted for this size. The efficiency of drop deposition on the filter paper and glass slides, was checked by I. Langmuir and K. B. Blodgett's method (1945) cited in A. H. Woodcock and M. M. Gifford (**15**), and the measured number of droplets for each diameter grade was multiplied by a correction factor. This factor was found to be significant only for droplets smaller than 50μ. Observation of droplets was also made at the same fetches together with observation of wind profiles, at the height ranging from 8 cm to 25 cm, where wind profiles obey the logarithmic law.

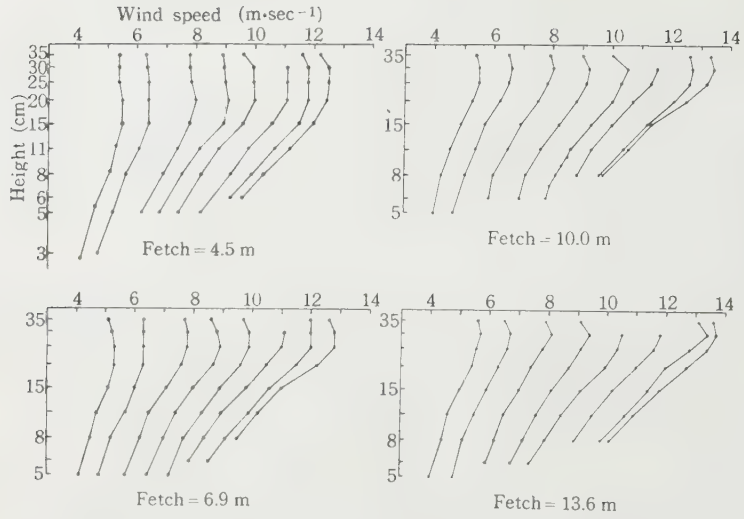

Fig. 1. Distribution of the wind speed. Heights are measured above the still water surface.

Table 1. The mean wind speed in the cross section of the wind tunnel and the wind speed at 10 m level.

Mean wind speed ($m \cdot sec^{-1}$)	12.1	11.6	10.8	9.7	8.7	7.5	6.1	5.1
Wind speed at 10 m level ($m \cdot sec^{-1}$)	22.8	21.4	18.7	16.5	14.9	12.6	10.3	8.7

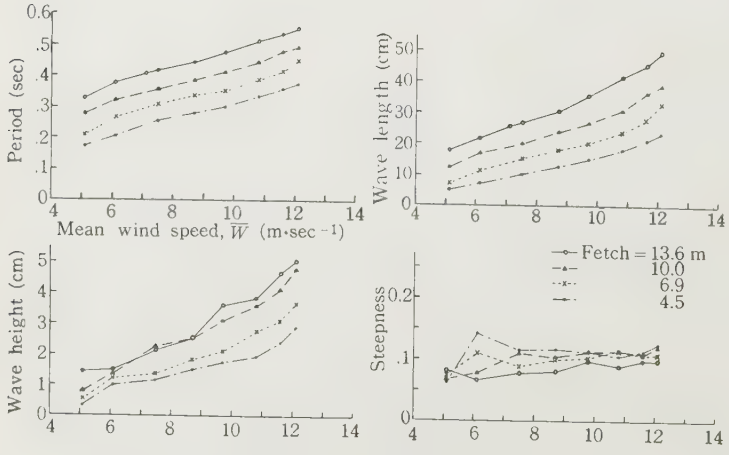

Fig. 2. Elements of the main wind waves.

2.2. Distribution of wind speed and elements of wind waves

Eight grades of the mean wind speed, ranging between 5.1 m·sec^{-1} and 12.1 m·sec^{-1}, were used. The observed wind profiles at each fetch are illustrated in Fig. 1. Retween 8 cm and 15~25 cm in height, they were represented approximately by the logarithmic law. Wind speeds at 10 m level were calculated by extrapolating these values. The values are listed in Table 1.

Average period and average wave height of the main gravity waves read from the wave records, and wavelength and steepness calculated from them are illustrated in Fig. 2.

3. Air entrainment in wind waves

3.1. Mechanism of the air entrainment in wind waves

The breaking of crests of large gravity waves reached to a maximum steepness has been so far regarded as the principal mechanism of the air entrainment and bubble formation in wind waves. At shores, a plunging breaker is considered to be an effective mechanism for the entrainment of bubbles. In the present experiment, another important mechanism has been observed for the first time. It is the entrainment of air bubbles caused by instability of small waves which override the large gravity waves, and in which the surface tension exerts to a considerable degree.

W. H. Munk (**16**) proposed a hypothesis for the fact that short wavelets are found forward of the crests of large waves. According to him, it is in such conditions that the sum of the phase velocity of foregoing capillaries and the orbital velocity of underlying wave is equal to the phase velocity of the underlying wave. A. H. Schooley (**17**) observed, in a small wind-wave tunnel, capillary waves which ride on the front of larger gravity waves and progressed with the same velocity as that of larger gravity waves. In the present experiment, these fine capillaries are also observed for 5 or 6 m·sec^{-1} in the mean wind speed (Fig. 3). But when the interference between trains of underlying gravity waves affects the orbital velocity of the waves, this condition breaks, and capillary waves that exist closest to the crests, are observed to move back relatively to the main gravity waves, and again lead the next crests of gravity waves.

When the wind speed increases further and main gravity waves become larger and more irregular, the above regularity no longer exists and all over the water surface becomes covered by wavelets, the wavelength of which is less than several cm, and which progress backward relatively to the main gravity waves. Fig. 4 shows this stage. At the first glance, main gravity wave train progresses with

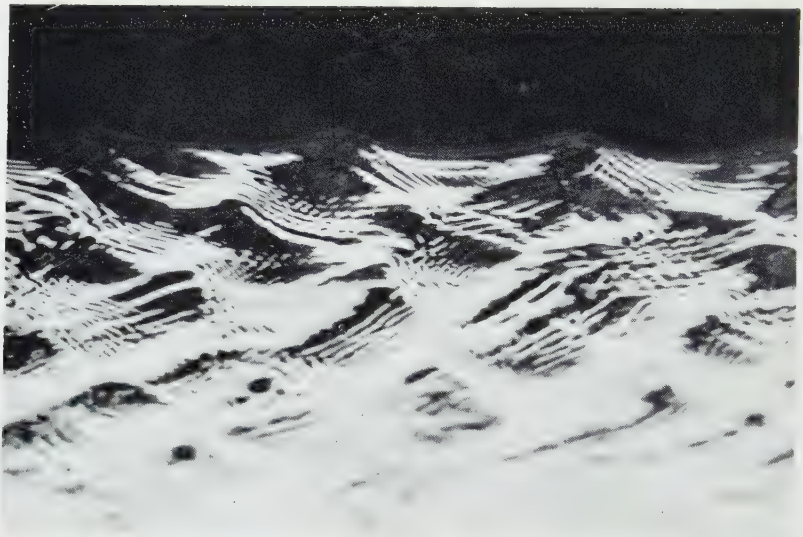

Fig. 3. Water surface seen from beneath. Capillary wave crests intersect one another. (W : 6.1 m·sec^{-1}, Fetch = 4.5 m)
The width of all the photographs is about 35 cm.

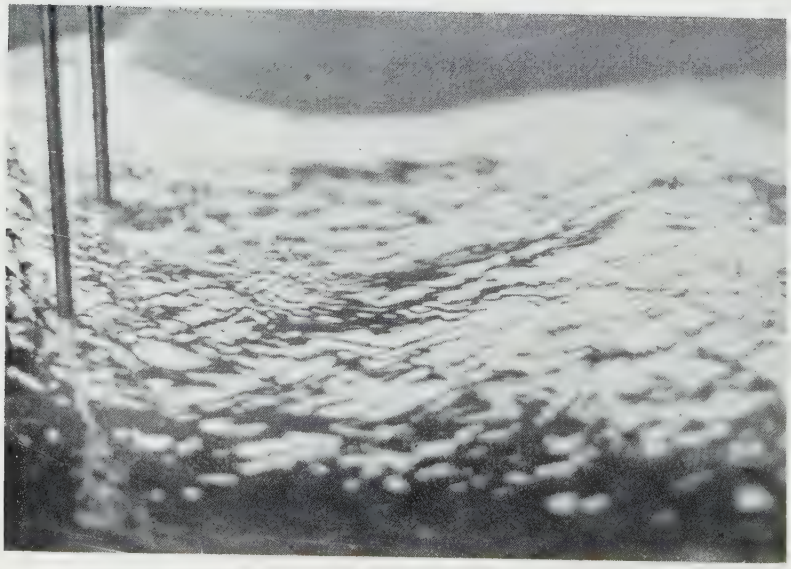

Fig. 4. Roughness rides all over the main wave train. ($\overline{W}$: 11.6 m·sec^{-1}, Fetch = 6.9 m)

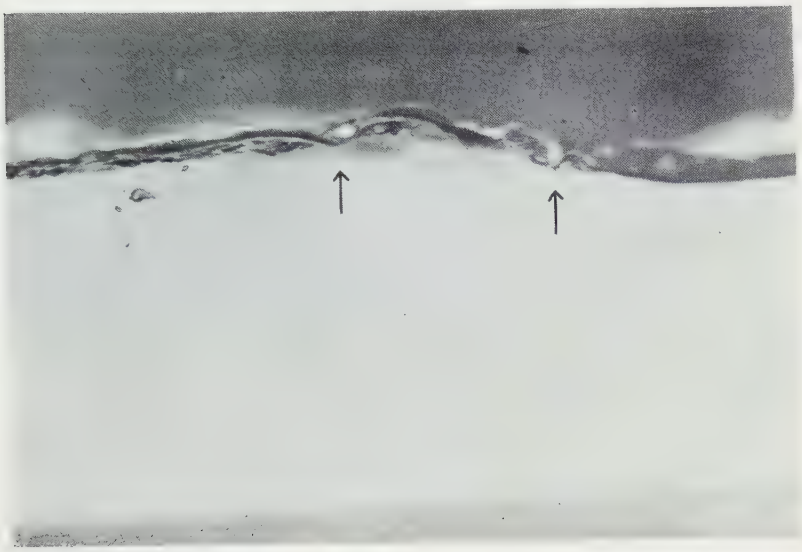

Fig. 5. Profiles of wavelets, which peak downwards. ($\overline{W}$ = 8.7 m·sec^{-1}, Fetch = 13.6 m)

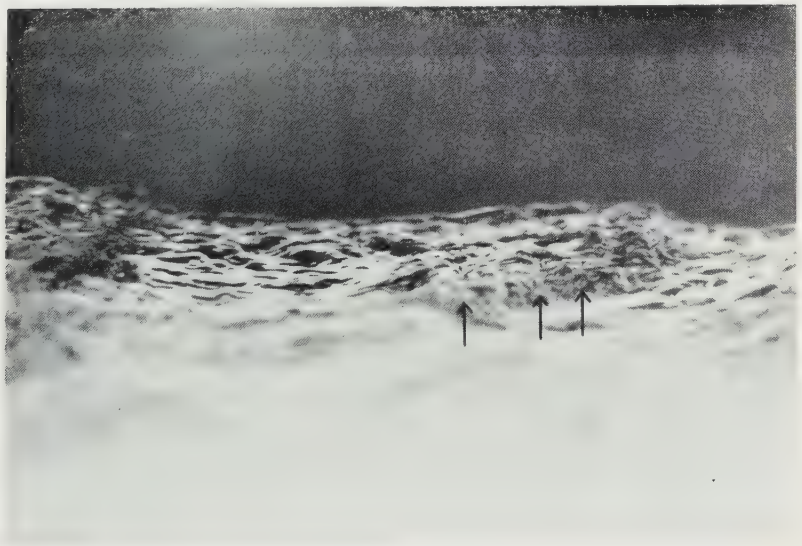

Fig. 6. Roughness from beneath. It looks like a ceiling of a stalactite grotto. ($\overline{W}$ = 11.6 m·sec^{-1}, Fetch = 4.5 m)

a certain speed, and wavelets on it exist at random. However, if one turns one's eyes away from the main wave train, and set them to wavelets, one will find a pattern of wavelets progressing with a speed smaller than that of the gravity wave train which passes through it. It appears to converge where crests of main waves pass, and diverge where troughs of them pass, namely, it seems that, through a medium of the pattern of wavelets, a longitudinal wave train progresses with a phase velocity equal to that of the main gravity wave train. This kind of convergence had been pointed out by P. J. H. Unna (**18**) for larger gravity waves, and was cited by Munk (**19**). This kind of convergence and the interference of wavelets, as shown in Fig. 3, increase the steepness of the wavelets. These wavelets of large steepness also have a profile that peaks downwards, which is the reverse of the case of gravity waves, as Schooley (**17**) observed for small capillary waves. Fig. 5 shows the typical profile of this type. The water surface, as seen from beneath, looks like a ceiling of a stalactite grotto (Fig. 6). This again confirms G. D. Crapper's theory (**20**) of capillary wave profiles. As Crapper suggested for pure capillary waves, air bubbles are enclosed at the troughs, and scatter into water by turbulence as shown in Fig. 7. Since the profile of these wavelets may be determined by factors such as the surface tension, the acceleration of gravity, the viscosity, etc., bubbles thus entrained will have a definite size range, but because of the very complicated situation the definite size range does not manifest itself apparently. Further developed conditions of the air entrainment of this type are shown in Fig. 8. Although bubbles are being entrained, basic gravity wave itself is not always breaking, as understood from the photograph.

The condition in which this mechanism of the air entrainment first occurs will be shown in **3.3.** The wind speed is much greater than force 4 on the Beaufort scale, and is about $13\,\mathrm{m\cdot sec^{-1}}$ (10 m level). This mechanism is expected to occur all over the crests of comparatively small gravity waves at the sea surface, when wind speed exceeds further this value. This wind speed is considered to be an important critical wind speed for air-sea boundary processes. As this mechanism of the air entrainment is much affected by the surface tension of sea water, a change in the surface tension at the sea surface may result in a corresponding change in the rate of production of sea-salt nuclei over the oceans.

3.2. Distribution of the air bubbles in wind waves

Bubbles are entrained when some main wave crests pass, and rise through water until the next entrainment occurs. To obtain an average vertical distribution of entrained bubbles, for each wind speed and for each fetch, it is desirable to take at random time a number of photographs for each condition, and to take an

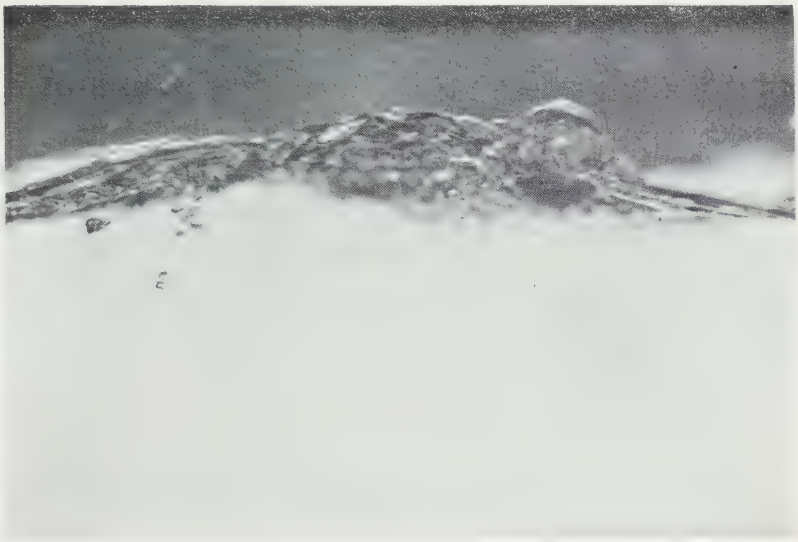

Fig. 7. Bubbles are being entrained in wind waves. ($\overline{W}=10.8\ \mathrm{m\cdot sec^{-1}}$, Fetch = 13.6 m)

Fig. 8. Further developed conditions of the air entrainment. ($\overline{W}=11.6\ \mathrm{m\cdot sec^{-1}}$, Fetch = 13.6 m)

average of them. But it is rather useless, because there appears no bubble on the majority of the photographs, especially for lower wind speeds. Thus, an alternative method is employed to take rather a small number of photographs, by aiming at instances when bubbles come in sight of the camera, and to estimate the average distribution of bubbles by use of the other properties together, which are explained in the next section.

The number and the size of bubbles on photographs have been read for each depth below the water surface. Examples of the vertical distribution of bubble number are shown in Fig. 9. As seen in the figure, the number of bubbles decreases exponentially with increasing depth. This vertical distribution can be used to estimate the coefficient of mixing in wind waves, which will be mentioned in the last section of this paper.

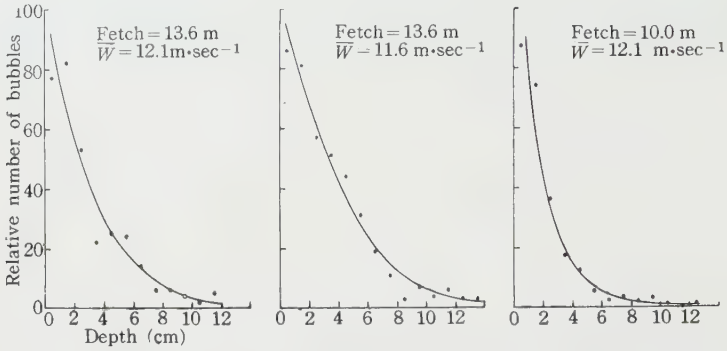

Fig. 9. Examples of the vertical distribution of the entrained air bubbles in wind waves.

3.3. Rate of entrainment of the air bubbles in wind waves

It can be considered that there exists an equilibrium condition, in an average, between bubbles entering from water surface and those rising to the surface. Consequently, the average rate of entrainment of bubbles (B) can be estimated by the product of average concentration at the surface (θ_0) and the rising velocity (w) of bubbles for each bubble size. Namely,

$$B = w\theta_0 .$$

But, θ_0 is not known and what is actually known is θ_0', which is an average surface concentration of bubbles at a region of the wave train where bubbles are formed. To reduce θ_0' to θ_0, some factors that represent a proportion of the region of wave train where bubbles exist to that where they do not, must be multiplied. One factor is $\alpha/100$, where α represents the percentage of crests

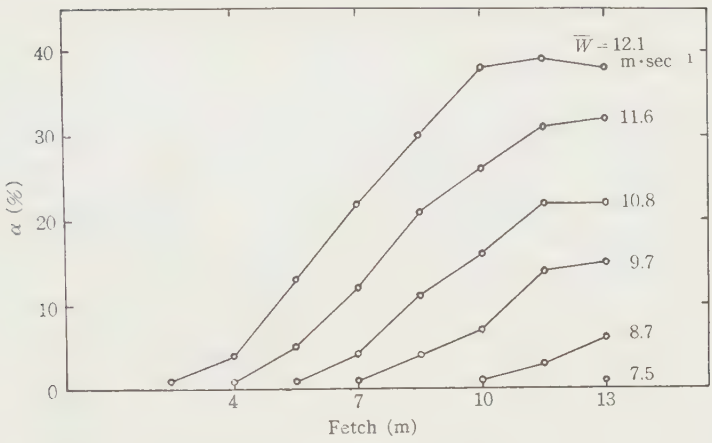

Fig. 10. Values of α: the percentage of crests of main gravity waves that are entraining air bubbles.

of main gravity waves that are entraining air bubbles (not all of the crests of main gravity waves entrain bubbles). Values of α are shown in Fig. 10.

As seen from the figure, the lowest wind speed for the occurrence of the air entrainment at 13 m in fetch, is 7.5 m·sec^{-1} in the mean taken in the tunnel section, and this corresponds to 13 m·sec^{-1} at 10 m level. The critical wind speed increases with decreasing fetch. However, curves in Fig. 10 seem to saturate already at 13 m in fetch, so that this critical wind speed may apply to the open ocean.

The other factor is $[\theta']\ Tw\theta_0'$, where $[\theta']$ means the total number of bubbles, for each size grade, contained in a water column of unit base area, and T is the period of the main wave. The ratio $[\theta']/w\theta_0'$ means a sort of residence time, or an average life-time of bubbles in water. The terminal velocity of the air bubbles in water (w) was examined critically in a paper by R. L. Datta *et al.* (**21**). According to it, the velocity of small bubbles increases almost linearly with an increasing bubble size, and reaches about 32 cm·sec^{-1} for a bubble of 2 mm in diameter, then decreases to 24 cm·sec^{-1} for one of about 6 mm, and then increases slowly. The residence time is generally smaller than T. The ratio of the residence time to T is thus understood to be necessary for reducing θ' to θ. Consequently, B is given by

$$B = w\theta_0' \times \frac{\alpha}{100} \times \frac{[\theta']}{Tw\theta_0'}$$

$$= \frac{\alpha}{100T}[\theta'].$$

The calculated value of B for each fetch and each wind speed is illustrated

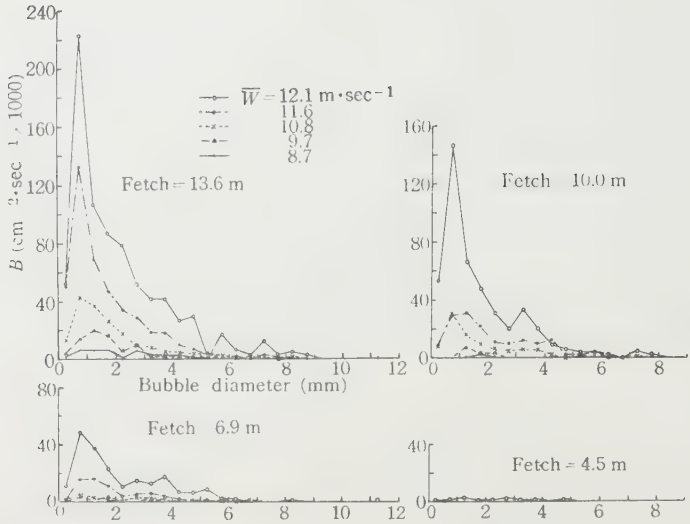

Fig. 11. Values of B: the rate of formation of air bubbles in wind waves.

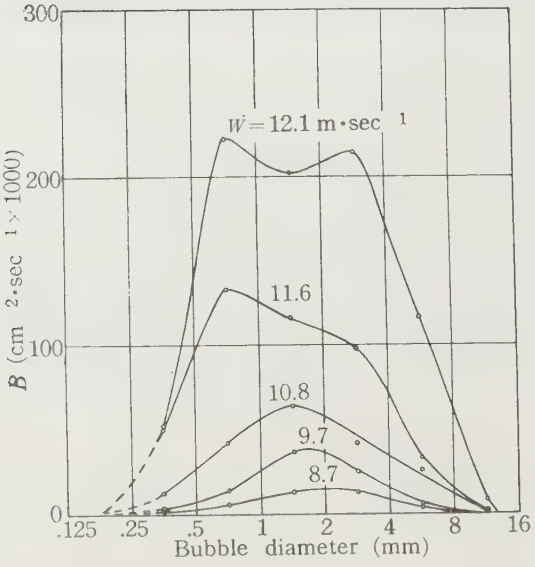

Fig. 12. Values of B per equal log(bubble size) interval, for 13.6 m in fetch.

in Fig. 11 for each bubble size. From this figure it is found that bubbles between 0.5 mm and 1 mm in diameter are observed most frequently, and that this dominant peak diminishes rapidly as the wind speed decreases or as the fetch decreases, namely, as the rate of bubble entrainment decreases. Bubbles of this peak seem to be produced by great disturbance of water due to turbulent motion in waves, when bubbles are being entrained. The values of B per equal log(bubble size) interval, are calculated by smoothed values from Fig. 11, and are shown in Fig. 12 for 13.6 m in fetch. The curves have nearly symmetrical shapes, with their axes between 1 mm and 2 mm in bubble diameter, the axes tending to shift to larger diameters for lower wind speeds.

4. Drop production from wind waves

4.1. Drop production by bursting of air bubbles

It seems that there are at least two different mechanisms of drop production by bursting bubbles. One is the disintegration of water jet formed upon collapse of a bubble cavity. Relations among the size, the number and the height of the ejection of these droplets, and the bubble size and the temperature for sea water were studied by C. G. Boyce (**1**), D. C. Blanchard and A. H. Woodcock (**7**), S. Hayami and Y. Toba (**8**) and others (**2, 3, 4, 5, 6, 9**), and for fresh water, by O. Stuhlman Jr. (**22**) and D. M. Newitt *et al.* (**23**). From these results, one can see that the droplets have a size of ten and odd percents of the original bubbles, and that the occurrence of this mechanism is mainly restricted to bubbles smaller than 4 mm in diameter, and further that the ejection is most conspicuous for droplets of about 300μ in diameter.

The other mechanism seems to concern with the shuttering of bubble film. Using sea water, B. J. Mason (**6**) observed that, besides the large drops produced by disintegration of the jets, bubbles greater than 2 mm diameter produced a second group of droplets having diameters between 5μ and 30μ, bubble of 2 mm diameter producing, on an average, only about one droplet in this size range. This group of droplets was also measured by D. M. Newitt *et al.* (**23**), who measured for bubbles ranging between 3.1 mm and 5.3 mm of fresh water. The mean size of these droplets lay between 60μ and 20μ. The majority of these droplets were formed below 1 cm in height. The number of these droplets is found to be nearly proportional to the area of bubble film calculated by Y. Toba (**24**), and about 50 per 1 cm^2 of the film, as shown in Table 2. This relation seems to show that this group of droplets is produced by shuttering of bubble film. Experiments by K. Isono (**9**) on bubbles of sea water of 3 mm diameter also show similar results in size distribution of droplets, but the number is rather large.

Table 2. Summarized relation between bubbles and droplets produced from them.

Bubble diameter (mm)	Droplets from jet: Allotment of bubble number (%)	Droplets from jet: Diameter (μ)	Droplets from jet: Number per bubble	Droplets from film: Number assumed to be 50 per 1 cm^2 of bubble film (Diameter: 0~50μ)	Droplets from film: Number from data by Newitt *et al.* (23)
0 ~ 0.5		0~ 50	4		
0.5~ 1.0	80	50~100	4	0.005	
	20	100~150	4		
1.0~ 1.5	40			0.045	
	60	150~250	3.6		
1.5~ 2.0	46			0.17	
	54	250~350	2.5		
2.0~ 2.5	46			0.42	
	54	350~450	1.6		
2.5~ 3.0	32			0.90	
	68	450~550	1		
3.0~ 3.5	20			1.6	1.6
	80	550~650	1		
3.5~ 4.0	10			2.7	2.4
	90	650~750	1		
4.0~ 4.5				4.3	3.8
4.5~ 5.0				6.2	6.0
5.0~ 5.5				8.7	11
5.5~ 6.0				11.6	
6.0~ 6.5				15	
6.5~ 7.0				19	
7.0~ 7.5				23	
7.5~ 8.0				29	
8.0~ 8.5				35	
8.5~ 9.0				42	
9.0~ 9.5				50	
9.5~10.0				58	

Table 3. Values of F_1': the rate of droplet production from wind waves, estimated from the rate of entrainment of bubbles, at 13.6 m in fetch. ($cm^{-2}\cdot sec^{-1}\times 10^3$)

Droplet diameter (μ)		$\bar{W}$ (m·sec^{-1}) 12.1	11.6	10.8	9.7	8.7
0~ 50	From jet	210	200	59	16	6.8
	From film	1700	450	220	66	37
	Sum	1900	650	270	82	44
50~100		710	420	140	45	18
100~150		400	220	92	43	16
150~250		390	230	122	71	24
250~350		200	100	58	35	14
350~450		91	45	22	13	6.1
450~550		48	22	9.0	5.3	2.9
550~650		42	19	6.5	3.7	2.4
650~750		34	13	5.0	2.8	1.8

Mason (6) found, in a cloud chamber, that bursting bubbles produced much larger numbers of particles of a third group too small to be detected by conventional methods. The number of these particles was between 100 and 200 for a bubble of 3 mm diameter, and their salt contents lay between 10^{-15} gm and $2\ 10^{-14}$ gm ($0.4 \sim 1.0\mu$ in droplet diameter). Droplets of this group were far small to produce giant nuclei.

Difference between sea water and fresh water may be significant, but it does not seem to be essential, at least so far as the results of the above-mentioned experiments of drop production reveal. For example, the efficiency and a critical point of drop ejection, measured by Hayami and Toba (8) by sea water bubble, seem indistinct in the experiment by Newitt *et al.* (23) for fresh water, but the latter shows similar features to the former; namely, the efficiency of drop ejection by jet disintegration seems to fall from about 3 mm to zero by about 6 mm diameter. The size of ejected droplets is also close in both cases.

Relations which combine the rate of bubble formation with the rate of droplet formation from the bubble, are summarized in Table 2, which also contains the comparison between the number of droplets produced by shuttering of bubble film obtained by assuming the production rate to be 50 per 1 cm^2 of film, and the value from the experiment by Newitt *et al.* (23).

4.2. Rate of drop production estimated from the entrained air bubbles in wind waves

Using Table 2 and smoothed values of B in **3.3**, the rate of drop production from wind waves is estimated as shown in Table 3 for 13.6 m in fetch. It is seen that the number of droplets produced by film shuttering is much larger than that by jet disintegration. The items of the former are illustrated in Fig. 13, showing that bubbles of several mm in diameter are most responsible for drop formation of this group.

4.3. Distribution of water droplets in space above wind waves

From the number of droplets caught, in a given time interval, by dye-treated filter paper and glass slides coated with MgO and from wind profiles, the number of droplets contained in a unit volume of the air was calculated for each drop size grade, by taking account of the drop deposition error on ribbons. The size grades smaller than 350μ are listed in columns I and II of Table 4. The typical examples of the distribution are shown in Fig. 14 for 13.6 m in fetch. Results of the droplet measurement by dye-treated filter paper, are also close to results of an experiment carried out by S. Okuda and S. Hayami (25) on the evaporation from wavy surface, by use of the same wind flume.

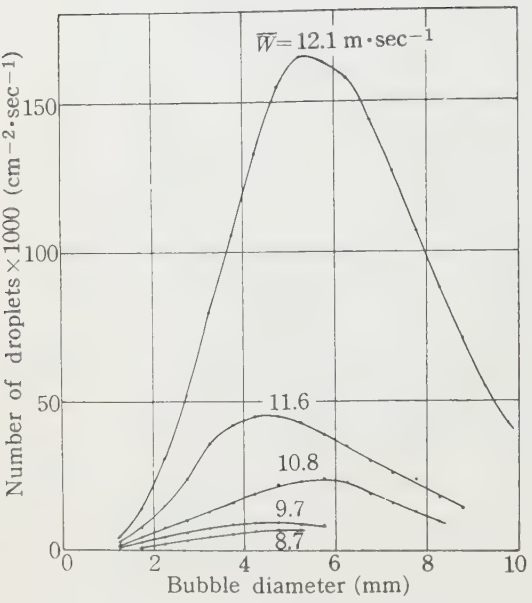

Fig. 13. Relation between the number of droplets produced by shuttering of bubble film and bubble diameter, for 13.6 m in fetch.

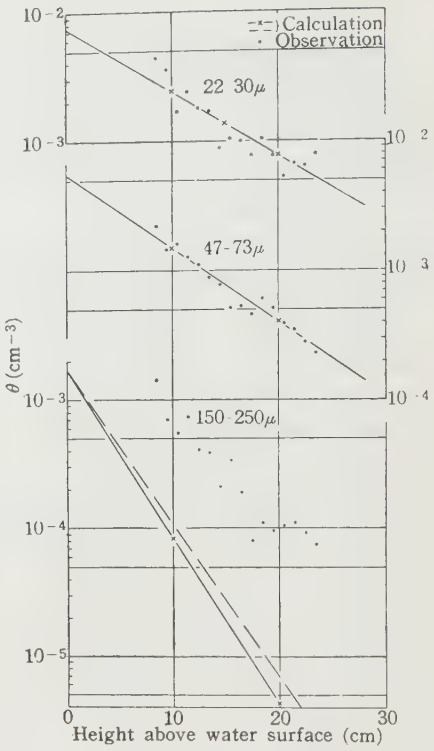

Fig. 14. Examples of the distribution of droplet concentration (θ) in the wind-flume, observed and calculated, for $\bar{W}$= 12.1 m·sec^{-1} and fetch=13.6 m. The broken line is the calculated curve by Eq. (4) below.

Consistency of the distribution of droplets in the space above wind waves, with the rate of production of droplets estimated in the last section, will be examined theoretically in the following chapter. The result will confirm that the droplets are produced by bursting of the entrained bubbles. However, much larger droplets that had diameters of 1 mm or more were caught occasionally. They could be distinguished from droplets produced by bubbles because of their extraordinary sizes. They are considered to be sprashing water from wave crests.

5. Theoretical considerations

5.1. Process of diffusion of droplets produced at the air-water boundary

Consider a simple case where wind blows uniformly in a horizontal direction. Take the coordinate origin at the entrance to the flume, the x-axis in the direction of the wind velocity, and the z-axis positive upward from the still water surface.

For the sake of convenience, consider a class of droplets of the same diameter, or of the same terminal velocity. Let u denote the wind velocity, w the terminal velocity of the droplet falling in the air, η the coefficient of mixing, and θ the number of droplets contained in the air per unit volume, or the concentration of droplets in the air. Then, the equation of droplet distribution in the air is given, under stationary conditions, by

$$u\frac{\partial\theta}{\partial x}=w\frac{\partial\theta}{\partial z}+\eta\frac{\partial^2\theta}{\partial z^2}. \tag{1}$$

Boundary conditions are

$$\left.\begin{aligned} -\eta\frac{\partial\theta}{\partial z}&=F(x) \quad \text{at} \quad z=0\ ,\\ \theta&=0 \quad \text{at} \quad z=\infty\ ,\\ \theta&=0 \quad \text{at} \quad x=0\ , \end{aligned}\right\} \tag{2}$$

and

where $F(x)$ represents the time rate of production of droplets per unit area of the water surface. The solution of Eq. (1) subject to the conditions (2) is given by

$$\theta=\int_0^x F(x-\lambda)\left\{\frac{1}{\sqrt{\pi\eta u\lambda}}e^{-\frac{1}{4\eta}\left(\frac{uz^2}{\lambda}+\frac{w^2\lambda}{u}+2wz\right)}-\frac{w}{2\eta u}\operatorname{erfc}\left(\frac{w\sqrt{\lambda}}{2\sqrt{\eta u}}+\frac{z\sqrt{u}}{2\sqrt{\eta\lambda}}\right)\right\}d\lambda\ , \tag{3}$$

where

$$\operatorname{erfc}(x)=1-\frac{2}{\sqrt{\pi}}\int_0^x e^{-t^2}dt\ .$$

For infinitely long fetch the solution becomes

$$\theta=\frac{F}{w}e^{-\frac{w}{\eta}z}=\theta_0 e^{-\frac{w}{\eta}z}\ . \tag{4}$$

In this case, F is considered as constant.

Further, when the droplet distribution given by Eq. (4) is brought on land where the production of droplets at the boundary does not exist any longer, the boundary conditions for Eq. (1) become

$$\left.\begin{aligned} \theta&=\frac{F}{w}e^{-\frac{w}{\eta}z} \quad \text{at} \quad x=0\ ,\\ \theta&=0 \quad \text{at} \quad z=\infty\ ,\\ \frac{\partial\theta}{\partial z}&=0 \quad \text{at} \quad z=0\ , \end{aligned}\right\} \tag{5}$$

and

where the origin of the x-axis is taken at the coast. The solution for this case is given as follows:

$$\theta \quad F\left[\frac{1}{w}e^{-\frac{w}{\eta}z}-\int_0^x\left\{\frac{1}{\pi\eta ux}e^{\frac{1}{4\eta}\left(\frac{uz^2}{x}+\frac{w^2x}{u}+2wz\right)}\right.\right.$$
$$\left.\left.-\frac{w}{2\eta u}\operatorname{erfc}\left(\frac{w\sqrt{x}}{2\sqrt{\eta u}}+\frac{z\sqrt{u}}{2\sqrt{\eta x}}\right)\right\}dx\right]. \qquad (6)$$

5.2. Comparison of theoretical calculations with data from the experiment
Determination of the rate of droplet production from wind waves

To calculate θ by Eq. (3), it is necessary to determine $F(x)$. In a range of the fetch within which the present experiment was carried out, F can approximately be expressed, as seen from the values in Fig. 11, by

$$F = F_1(x-x_0)/(1360-x_0)\,,$$

where F_1 represents the value of F at 13.6 m in fetch, x_0 being the fetch where the air entrainment began to take place. For the case of $\overline{W}=12.1\ \mathrm{m\cdot sec^{-1}}$ ($\overline{W}$: the mean wind speed in the tunnel section), 460 cm was adopted for x_0.

The terminal velocity (w) of a water droplet smaller than about 1.7 mm in diameter can be calculated from knowledge of the fluid resistance exerting upon a moving sphere. Values of w has been calculated from the formulae by C. N. Davies (1945), which are expressed as follows (**26**):

$$Re = \frac{C_D Re^2}{24}-2.3363\times10^{-4}(C_D Re^2)^2+2.0154\times10^{-6}(C_D Re^2)^3$$
$$-6.9105\times10^{-9}(C_D Re^2)^4\,,$$
$$\text{for}\quad Re<4\quad\text{or}\quad C_D Re^2<140\,;$$

$$\log Re = -1.29536+9.86\times10^{-1}\log(C_D Re^2)$$
$$-4.6677\times10^{-2}[\log(C_D Re^2)]^2+1.1235\times10^{-3}[\log(C_D Re^2)]^3\,,$$
$$\text{for}\quad 3<Re<10^4\quad\text{or}\quad 100<C_D Re^2<4.5\times10^7\,,$$

where Re and C_D represent Reynolds number and drag coefficient, respectively. They are given by

$$C_D Re^2 = 4(\rho_l-\rho_a)gd^3/3\rho_a\nu^2\,,$$

and

$$w=\frac{\nu Re}{d}\,,$$

where d is the diameter of the sphere, ν is the kinematic viscosity of the air, and ρ_l and ρ_a are the density of the liquid and the air, respectively. It is noticed that the water drop of diameter 142μ represents a critical point in the law of terminal velocity. Droplets smaller than about this size (containing 7.5×10^{-8} gm of salts) can be picked up into the upper air easily as seen from the following section.

For the value of u, $1000\ \mathrm{cm\cdot sec^{-1}}$ (a value at about $z=10$ cm) has been used.

The value of η is said to be estimated by $\eta=0.4\,w_*z$, where w_* is the friction velocity. It has been evaluated from the data obtained by H. Kunishi (27) on the structure of wind stress, based on measurements of the distribution of wind velocity in the same wind flume. It is found that $w_*=107$ or $\eta=26.9z$ for $\overline{W}=12.1\,\mathrm{m\cdot sec^{-1}}$. Thus, it is presumed that the representative value of η in the present experiment is about 250 c.g.s. for $\overline{W}=12.1\,\mathrm{m\cdot sec^{-1}}$.

By Eq. (3) θ was calculated numerically for a case of droplets of $50\sim100\mu$ in diameter, for $\eta=500$ and $\eta=250$, respectively. The values are shown in Fig. 15 by circles and crosses respectively. The distribution of θ calculated by assuming $\eta=250$ has the same gradient with the observation, but somewhat shifting upwards. This shift must result from an overestimation of F_1. The value of $\eta=250$ is applied to all the drop size grades and examples of the calculation are shown in Fig. 14 by crosses. For drop size smaller than 100μ, the calculation has been performed by taking at first F_1 to be unity, and parallel translation of the results has been made to fit the observations, the distance of translation representing the true value of F_1. Thus obtained values of F_1 are tabulated in column IV of Table 4. The corresponding values of F_1 estimated from the entrained bubbles and denoted as F_1' (Table 3), are shown in column V, and the ratio F_1/F_1' is shown in column VI. For droplets smaller than 100μ, the ratio is about 0.3. This discrepancy between F_1 and F_1' can be well understood by the fact that F_1' has been calculated by an assumption that each bubble produces droplets in a way shown in Table 2, but, in fact, flocking and coalescence of bubbles occur at the water surface and reduce the rate of formation of droplets. The reduction factor thus seems to be about 0.3 in the case of our experiment.

For droplets of $150\sim250\mu$, the observed values of θ are denser for larger z compared with the calculation as seen from Fig. 14, and for droplets of $250\sim350\mu$, the tendency becomes stronger. This arises probably from a fact that these droplets are ejected to some height when they are produced by disintegration of the jets. The ejection is most conspicuous for droplets of 300μ, as stated in **4.1.** If one considers that the origin of z-axis must be taken at some level above water surface owing to the ejection, for example, at $z=3$ cm for droplets of $100\sim150\mu$, at $z=6$ cm for those of $150\sim250\mu$ and at $z=7$ cm for those of $250\sim300\mu$, the reduction factor takes values similar to the case of droplets smaller than 100μ. In Table 4, the reduction factor for droplets larger than 100μ is assumed to be 0.30. The calculated values in Fig. 14 are given after multiplied by the reduction factor. This sufficient consistency between the observation and the calculation confirms that droplets observed in the air above wind waves have been produced by bursting of air bubbles entrained in the way already described.

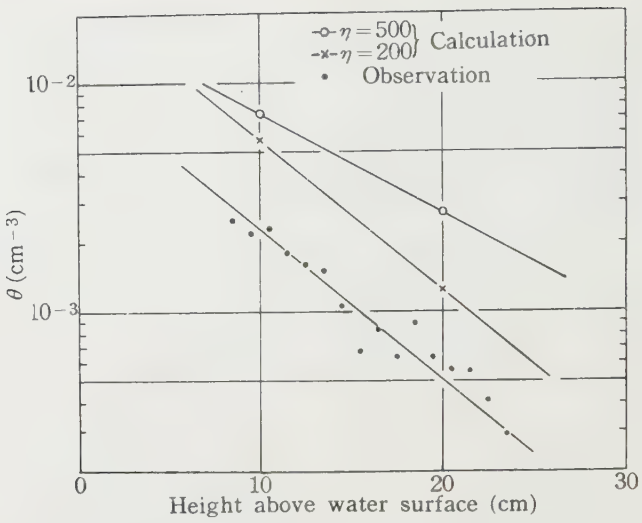

Fig. 15. Comparison among the distributions of θ calculated by assuming $\eta=500$ and $\eta=250$, and observed, for droplet diameter $=50\sim100\,\mu$, $\bar{W}=12.1\,\mathrm{m\cdot sec^{-1}}$ and fetch $=13.6$ m (see the context).

Table 4. Values concerning the droplets produced from wind waves when the wind speed is $22.8\,\mathrm{m\cdot sec^{-1}}$ (at 10 m level) (see the context).

I Drop diameter of center of size band (μ)	II Range of each size band (μ)	III w ($\mathrm{cm\cdot sec^{-1}}$)	IV F_1 for size band of II ($\mathrm{cm^{-2}\cdot sec^{-1}}$)	V F_1' for size band of II ($\mathrm{cm^{-2}\cdot sec^{-1}}$)	VI $\frac{F_1}{F_1'}$	VII $\frac{w\rho_0(x=13.6\,\mathrm{m})}{F_1}$	VIII F_1 for 10μ size band ($\mathrm{cm^{-2}\cdot sec^{-1}}$)	IX $F_1/w=\theta_0(x=\infty)$ for 10μ size band ($\mathrm{cm^{-3}}$)
8.6	<13	0.22	0.11	—	—	0.012	0.13	0.58
17	13～ 22	0.85	0.161	—	—	0.044	0.19	0.22
26	22～ 30	2.0	0.147	—	—	0.10	0.17	0.086
34	30～ 39	3.5	0.078	—	—	0.17	0.091	0.026
43	39～ 47	5.4	0.035	—	—	0.26	0.041	0.0075
Sum			0.54	1.9	0.28			
60	47～ 73	10.2	0.125	—	—	0.44	0.048	0.0047
86	73～100	19.3	0.086	—	—	0.70	0.033	0.0017
Sum			0.21	0.71	0.30			
125	100～150	36.1	0.12	0.40	(0.30)	0.93	0.023	0.00064
200	150～250	68.8	0.12	0.39	(0.30)	0.95	0.012	0.00017
300	250～350	114	0.060	0.20	(0.30)		0.0060	0.000053

It must be noted here that the calculated values of θ lie nearly on straight lines in the graphs, together with points by observation. This shows that, although observed distribution of droplets appears exponential, it does not mean that the equilibrium condition expressed by Eq. (4) is obtained. In reality, the ratio $w\theta_0(x=13.6\,\mathrm{m})/F_1$, namely, the ratio of the rate of fall of droplets and the rate of production of them at 13.6 m in fetch, is calculated, and listed in column VII of Table 4, which shows that the smaller the droplets are, the farther the state is from the equilibrium, and that the equilibrium conditions (4) nearly hold only for droplets larger than 150μ. The distribution of θ calculated by Eq. (4) for 150~250μ in diameter is shown by a broken line in the figure. For 250~350μ in diameter, the calculation by Eq. (4) only is performed.

The obtained values of F_1 are converted respectively to the value for 10μ band of the droplet size, and are listed in column VIII of Table 4, and are shown in Fig. 16. The figure shows an outstanding peak at about 20μ in diameter. Also, it exhibits that a group of droplets produced through the shuttering of bubble

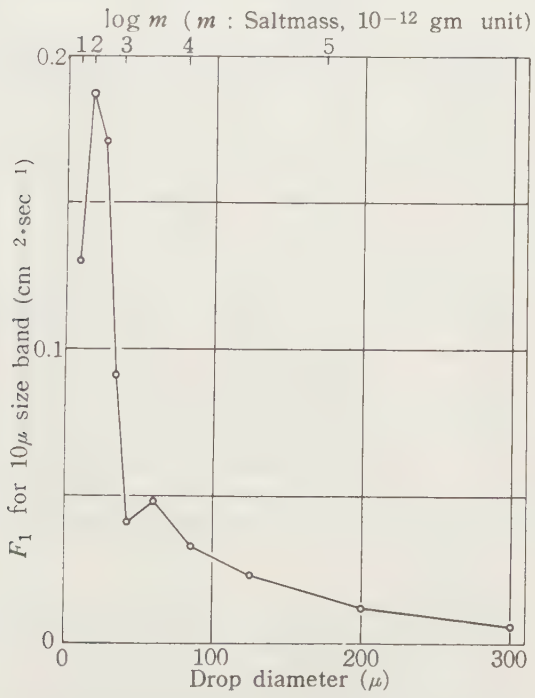

Fig. 16. Production rate of droplets from wind waves (F_1) when the wind speed is 22.8 m·sec^{-1} (at 10 m level). Values are shown for each 10μ size band of droplets.

film and which have diameters of a few tens μ, is superposed on a group of droplets which are produced through the jet disintegration and which seem to have a maximum frequency at about 60μ in droplet diameter.

It must be noted that, according to an estimation of the rate of evaporation of droplets in the wind flume before caught by the glass slides, droplets of the 8.6μ class may have been subjected to a significant change in size, so that a possibility arises that the degree of fall in the number of droplets, smaller than 20μ, is overestimated. However, this error belongs only to droplets smaller than 10^{-10} gm in the salt content, probably.

5.3. Distribution of sea-salt particles in the atmosphere

The value of F increases nearly linearly with the fetch, within short fetches as used in the experiment, and the value of F in equilibrium state cannot be estimated from the result of this experiment alone. But it may be supposed that it would not assume a value much different from F_1 (value of F at 13.6 m in fetch), because a value of wind stress over the water surface, measured at fetches

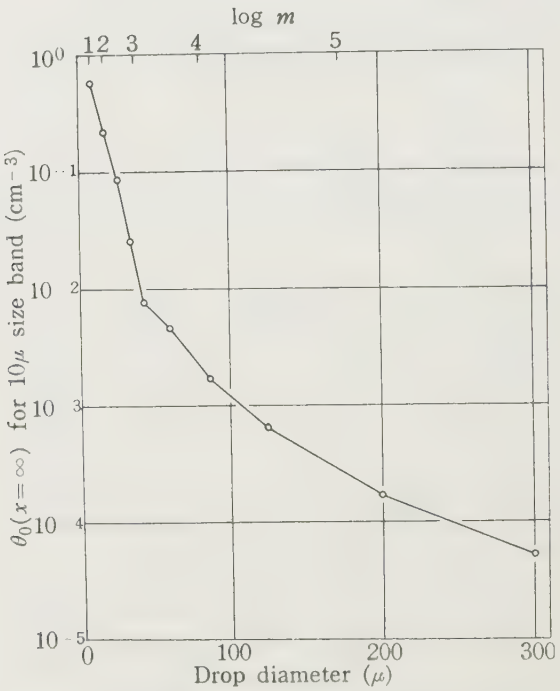

Fig. 17. Concentration of droplets at the surface of the open ocean (θ_0) when the wind speed is 22.8 m·sec^{-1} (at 10 m level). Values are shown for each 10μ size band of droplets.

greater than 10 m by use of the same wind flume by H. Kunishi (**27**), agrees with a value obtained by K. Brocks (**28**) at the North and Baltic Seas, and the value of α in **3.3** is also saturated already if the fetch exceeds 10 m. So, it is assumed that F is also saturated shortly and the value of F_1 nearly holds in the open ocean. This assumption will be ensured, in this and the next sections, by comparison of theoretical calculations using F_1 with actual observations.

The concentration of droplets at the surface of the open ocean is given by $\theta_0(x=\infty)=F_1/w$. The values of θ_0 calculated for 10μ size band are shown in column IX of Table 4 and in Fig. 17 for wind speed of 22.8 m·sec^{-1} (10 m level). From the figure, it is found that the concentration of droplets increases monotonously with a decreasing drop size, although the rate of production is maximum at 20μ diameter.

The size of droplets can be expressed by the mass of salt contained (m, in 10^{-12} gm unit) by assuming that the droplets consist of sea water. Fig. 17 has been redrawn in Fig. 18 by plotting $d\Theta_0/d(\log m)$ against $\log m$, where Θ_0 is the cumulative number of droplets, per unit volume of air at $z=0$ level, containing

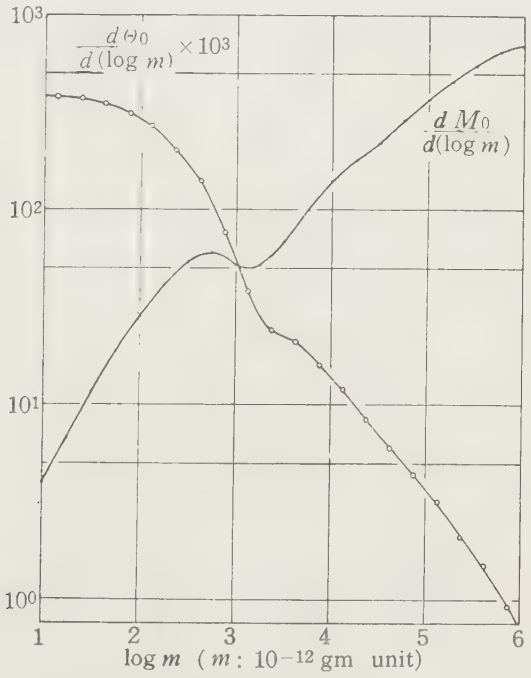

Fig. 18. Concentration-salt mass distribution and density-salt mass distribution of sea water droplets at the surface of the open ocean when the wind speed is 22.8 m·sec^{-1} (at 10 m level) (see the context).

salt less than or equal to m. The salt mass density M is defined as the total mass of sea salt, per unit volume of air, in droplets containing salt less than or equal to m, and the salt mass density-salt mass distribution at $z=0$ level is illustrated also in Fig. 18.

For the open ocean, Eq. (4) holds. Then comes

$$\log \frac{\theta_0}{\theta} = \frac{1}{2.3} \frac{w}{\eta} z ,$$

so that it is considered that for every distance of

$$\Delta z = 2.3 \eta / w ,$$

θ reduces to one order smaller. This distance is a function of w as well as of η, namely, it shows that larger droplets diminish rapidly at higher levels. Using this relation, one can estimate the salt mass density in the upper air from that at the sea surface. Using the values of terminal velocity of sea water droplets (w) shown in column III of Table 4, the salt mass density has been calculated for $z/\eta = 0.1$, 1 and 2, and is illustrated in Fig. 19 by full lines. However, droplets do not remain as sea water droplets, but evaporate and become lighter, and the terminal velocity becomes smaller. The effect makes peaks of curves shift to

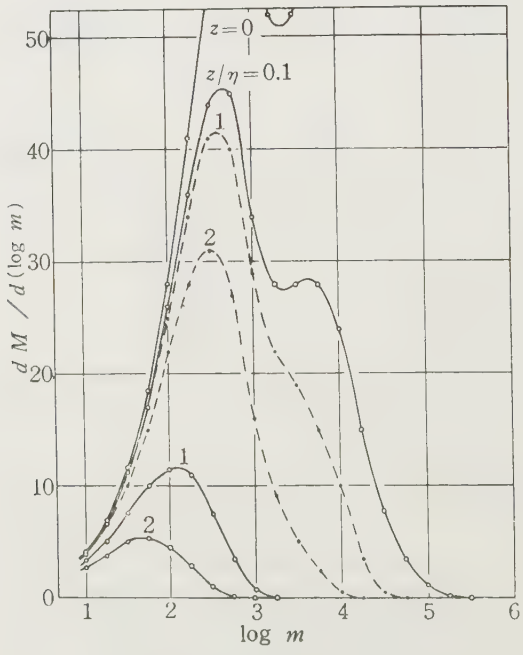

Fig. 19. Density-mass distribution of sea-salt particles at different heights (see the context).

the right. Using the values of w for dry sea-salt particles, the salt mass density has been calculated in the same way, and is illustrated by broken lines in Fig. 19. Actual conditions may lie between these two cases.

The salt mass density has a maximum value at $\log m=6$ for $z=0$, as seen from Fig. 18, but it has at about $\log m=3$ for $z/\eta=0.1$, and at around $\log m=2$ for $z/\eta=1$ or 2. If one assumes η in the lower atmosphere to be 10^4, $z/\eta=0.1$ will correspond to the condition at 10 m level, and $z/\eta=1$ at 100 m level. If η is 10^5, $z/\eta=1$ will correspond to the condition at 1000 m level. E. Eriksson (**29**) calculated the density-mass distribution from flight observations by A. H. Woodcock (**30, 31**) of sea-salt nuclei in the atmosphere at different wind forces, and obtained curves having similar features to those in Fig. 19. Considering that Fig. 19 represents a case of wind force 9, one may find that the order of magnitude is compatible with each other. The distribution of θ in the atmosphere is a complicated problem in meteorology, nevertheless the above fact seems to give a good support to the assumption that the values of F_1 represent the production rate of sea-water droplets at the open ocean surface for wind force 9. The other support will be given in the following section.

As to the position of the maxima of the curves in Fig. 19, one find that they shift to the left compared to Eriksson's figure. This may be explained by the coalescence of droplets in the course of their circulation.

5.4. Salt fallout near the coast, and dependence on wind speed

I. Kita and T. Aya (**32**) measured the rate of fallout of sea salt, between 20 m and 1000 m inland from the coast of Tadotsu, under a condition of the wind speed up to 20 m·sec^{-1}, and obtained the following empirical law:

$$q = e^{0.34u+0.8}x^{-1}, \qquad (7)$$

where q represents the rate of fallout of Cl in mg·m^{-2}·hr^{-1}, u the wind velocity in m·sec^{-1}, and x the distance from the coast line in m. If one assumes that the salt fallout has the same contents with sea water and considers the rate of fallout of total sea salt, q', in 10^{-6} mg·cm^{-2}·sec^{-1}, the above formula will be reduced to

$$q' = e^{0.34u-2.19}x^{-1}. \qquad (8)$$

The formula (8) is calculated for $u=22.8$, and the value is shown by a broken line in Fig. 20.

On the other hand, using Eq. (6), the salt fallout on land near the coast can be calculated as follows:

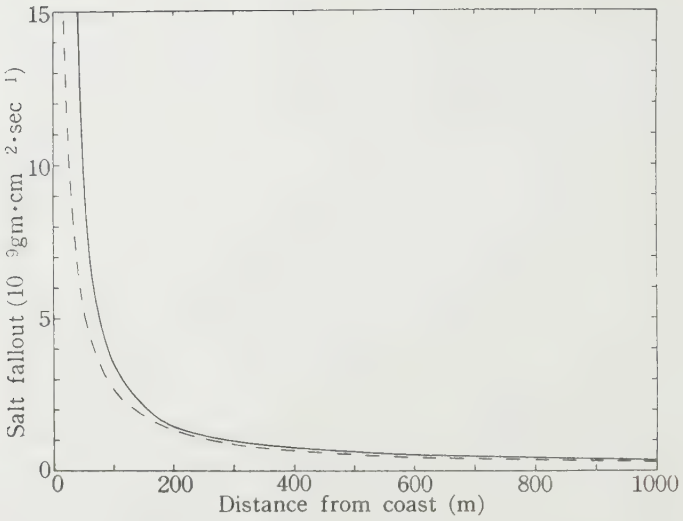

Fig. 20. Salt fallout near the coast. The full line is calculated by Eq. (6) by use of the value F_1, and the broken line represents the formula by KITA and AYA (32) (see the context).

$$q'(x,u) = \sum m w \theta_0$$
$$= \sum m F w \left[\frac{1}{w} - \int_0^x \left\{ \frac{1}{\sqrt{\pi \eta u x}} e^{-\frac{w^2 x}{4\eta u}} - \frac{w}{2\eta u} \operatorname{erfc}\left(\frac{w\sqrt{x}}{2\sqrt{\eta u}} \right) \right\} dx \right], \qquad (9)$$

where the summation must be performed concerning the droplet size grade. Eq. (9) is calculated by using the value of F_1 in column IV in Table 4. An example of the calculation of θ_0, by using values $\eta = 5 \times 10^3$ and $u = 2 \times 10^3$ (c.g.s. units), which are the conditions at about 2 m level for wind speed of 22.8 m·sec^{-1}, is shown in Fig. 21. The calculated value of q' is shown by a full line in Fig. 20.

If the full line is translated to the left by 25 m, it agrees with the broken line exactly. This means that $x = 0$ has been taken at 25 m off-shore in the calculation. In reality, there is a sea-bank about 3 m high, and it is considered that droplets produced near the sea-bank are not brought on land. The retreat of 25 m of $x = 0$ line in the calculation, therefore, would not be unreasonable. The above best agreement seems to ensure the validity of the value of F_1 used as the value at the open ocean.

In the empirical law due to Kita and Aya, the wind factor is expressed by $\exp(0.34u)$, when u is measured in m·sec^{-1}. On the other hand, as seen from Eq. (9), the rate of salt fallout on land is proportional to the value of F, as far as a

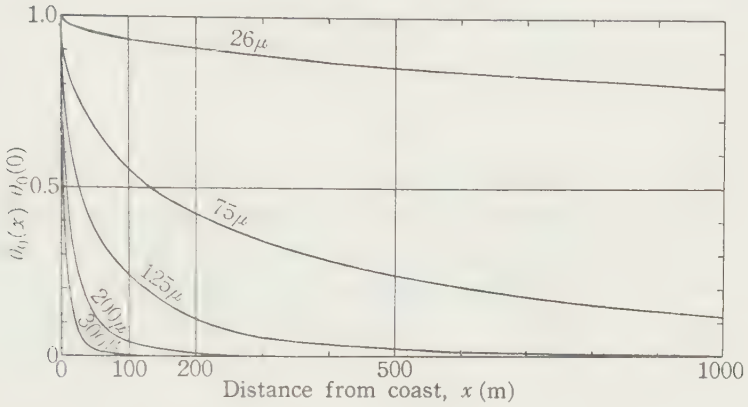

Fig. 21. Ratio $\theta_0(x)/\theta_0(0)$ calculated by Eq. (6) for five grades of droplet diameter.

class of droplets of the same size is concerned. Now, values of F_1' in Table 3 are multiplied by the reduction factor of 0.3 owing to bubble flocking, and the change of the rate of salt production with wind speed is obtained for the three classes of droplet size smaller than 150μ, because classes of larger droplets do not contribute to the salt fallout farther than several tens of the meter from the coast, as Fig. 21 shows. The values also depend on the wind speed exponentially and F or mF can be expressed roughly by the relation:

$$F \text{ or } mF = e^{0.40u+\text{const.}} \qquad (u : \text{m}\cdot\text{sec}^{-1}) , \tag{10}$$

in the range of the wind speed between 15 m·sec^{-1} and 23 m·sec^{-1}. Thus, the wind factor given by Eq. (10) agrees well with the result of field observation.

5.5. Coefficient of mixing in wind waves

In wind waves, there is scarcely any net transport of bubbles in the x direction, so that the distribution of bubble concentration can be expressed by the equation

$$w\frac{\partial\theta}{\partial z}+\eta\frac{\partial^2\theta}{\partial z^2}=0 , \tag{11}$$

where θ represents the concentration of bubble in water, w the terminal velocity of bubbles rising through water, η the coefficient of mixing in wind waves, and the z-axis is taken positive downward from the water surface. The boundary conditions in this case are

$$\left.\begin{aligned} &\theta = 0 && \text{at } z = \infty , \\ &\frac{\partial\theta}{\partial z} = -\frac{B}{\eta} && \text{at } z = 0 , \end{aligned}\right\} \tag{12}$$

and

where B is the time rate of the bubble formation at the water surface per unit area. If η=const., the solution is

$$\theta = \frac{B}{w} e^{-\frac{w}{\eta}z} = \theta_0 e^{-\frac{w}{\eta}z}, \tag{13}$$

and θ decreases exponentially with z.

As the average distribution of bubble concentration decreases nearly exponentially with depth, as shown in **3.2**, it is considered that the above condition holds in the range of the depth where bubbles are entrained, and one can estimate the value of η from the gradient of the graph showing the observed distribution of θ, namely,

$$\eta = \frac{wz}{2.3(\log \theta_0 - \log \theta)}. \tag{14}$$

Now, for the three examples shown in **3.2**, the value of η is calculated for each grade of the bubble diameter. They are shown in Table 5, together

Table 5. Coefficient of mixing in wind waves, estimated from vertical distribution of the entrained air bubbles.

Bubble diameter of center of size band (mm)		0.25	0.75	1.25	1.75	2.25	2.75	3.0<	(From the total number of bubbles)
w (cm·sec^{-1})		4.0	12	20	28	29	27	25	(20)
η(cm^2·sec^{-1})	$\overline{W}$=12.1 m·sec^{-1} Fetch=13.6 m	14	54	60	78	97	66	47	56
	$\overline{W}$=12.1 m·sec^{-1} Fetch=10.0 m	9	35		29	31		26	43
	$\overline{W}$=11.6 m·sec^{-1} Fetch=13.6 m	16	48	74	75	71	80	66	60

with the value of w used in the calculation. From this, it appears that the estimated values of η increase with the values of w, and the relation between η and w is given by

$$\eta = 6.5\, w^{3/4} \qquad \text{(c.g.s.)},$$

that is, $z/[2.3(\log \theta_0 - \log \theta)]$ is proportional to $w^{-1/4}$. The apparent change of η with w may be attributed to the change of w itself due to an interaction among many bubbles rising through water, because the values of w used in the above calculation are based on the data for single bubbles given by R. L. Datta *et al.* (**21**). If the value of η is assumed to be constant for all w as in the above reduction, though it is probably a function of z, the constant value of η will be obtained by assuming the actual rising velocity of bubbles (w') to be

$$w' = C w^{1/4}, \tag{15}$$

where C is a constant. Eq. (15) means that the rising velocity of bubbles is somewhat averaged in the case of grouping. Using this w' instead of w in Eq. (14), one obtains

$$\eta = 6.5\,C\,.$$

The value of C cannot be determined unless the independent estimation of η or w' is carried out. The values of η obtained from the distribution of total bubble concentration shown in **3.2** (Fig. 9) by use of a provisional representative value of $w=20\,\mathrm{cm\cdot sec^{-1}}$, are tabulated in the right column of Table 5.

6. Concluding remarks

From the above studies we may come to the following conclusion. When the wind speed exceeds about $13\,\mathrm{m\cdot sec^{-1}}$ (10 m level), small wavelets in which the surface tension exerts to a considerable degree and which have a profile that peaks downward, begin to enclose air bubbles at their troughs on crests of underlying gravity waves. The bubbles produce small droplets when they burst at the sea surface. Splashing water from wave crests is in large drops which fall back quickly into the sea, but droplets which are produced from bubbles and which contain salt less than $10^{-7}\sim10^{-8}$ gm are easily transported into the upper air by atmospheric turbulence, and form atmospheric condensation nuclei, among which the giant sea-salt nuclei can initiate rain from warm clouds. These smaller sea-salt particles are transported, as far as the inner part of continents, ceaselessly and play an important role in the circulation of materials on the earth. Comparatively large droplets are also transported as far as several hundred meters from the coast, and cause salt spray damage of the coastal plant.

There are at least two different mechanisms for droplet production by bursting bubbles, and they belong to either of the two bubble size ranges which are divided by a few mm in diameter. Droplets carried up into the upper air or transported far inland are produced mostly by film shuttering of bubbles of several mm. This is derived from bubble size distribution in wind waves, the number of droplets produced from each bubble, and the diffusivity of droplets in the atmosphere.

As to the dependence of the rate of droplet production on wind speed u ($\mathrm{m\cdot sec^{-1}}$ at 10 m level), it is expressed approximately by $\exp(0.40u)$ in the range of the wind speed between $15\,\mathrm{m\cdot sec^{-1}}$ and $23\,\mathrm{m\cdot sec^{-1}}$. The rate of production of droplets of each size grade for the wind speed of $23\,\mathrm{m\cdot sec^{-1}}$, is shown in Fig. 16 and column IV in Table 4. For this wind speed, the rate of production of sea-water droplets having diameter from several to 150μ (containing $10^{-11}\,\mathrm{gm}\sim8\times10^{-8}\,\mathrm{gm}$ of sea-salt), amounts to $0.87\,\mathrm{cm^{-2}\cdot sec^{-1}}$ in number, and to

6.0×10^{-9} gm·cm^{-2}·sec^{-1} in total mass of salt. If one considers droplets from several to 100μ (from 10^{-11} gm to 3×10^{-8} gm in sea-salt), the values become 0.75 cm^{-2}·sec^{-1} and 1.7×10^{-9} gm·cm^{-2}·sec^{-1}, respectively.

The above estimated production rate of sea-water droplets has been checked, by connecting it theoretically with actual data of giant sea-salt nuclei obtained by A. H. Woodcock, and with data of salt fallout near the coast. Now, the rate of salt production may also be considered as a link of sea-salt circulation on the earth. E. Eriksson (**29**) estimated the rate of total sea-salt deposition over the oceans to be about 10^{-11} gm·cm^{-2}·sec^{-1}. On the other hand, the concentration of chloride in rain water has been measured by many investigators, and there is an outstanding tendency that it decreases nearly exponentially with distance from the coast. Generally, the concentration seems to be less than 20 mg·l^{-1} even at coastal areas (**33**). This corresponds to the yearly total deposition of chloride by precipitation of 200 kg·ha^{-1}·year^{-1} in maximum, for 1000 mm of annual precipitation. This value is seen also in figures by Eriksson (**29**). If the deposition rate of chloride (including dry deposition) over the oceans is twice this value, it will become 10^{-10} gm·cm^{-2}·sec^{-1}. Depositon of the sea-salt on the continents is, according to Eriksson (**29**), only about 10 per cent of the total deposition on the earth. Hence, if one assumes that droplets smaller than 100~150μ produced at the sea surface are all transported into the upper air, one will come to a conclusion that atmospheric sea-salt is sufficiently furnished if only from a few per mille to a few per cent of sea surface area is always exposed to the wind of 23 m·sec^{-1}. On the other hand, B. J. Mason (**34**) states that if the sea surface is to be capable of supplying enough condensation nuclei for cloud formation, it must produce them at a rate of about 10^4·m^{-2}·sec^{-1} in number in the regions where waves are breaking. Even if only one tenth of the atmospheric condensation nuclei is sea-salt, the above rate will be 10^3·cm^{-2}·sec^{-1}. The result of the present study has revealed that the rate of droplet and bubble formation is 0.8 cm^{-2}·sec^{-1} for 23 m·sec^{-1} in wind speed. If one bubble produces 100~200 droplets of the third group that contain salt of 10^{-14}~10^{-15} gm as stated in **4.1**, the production rate will become only of the order of 10^2. Thus the rate of production of atmospheric sea-salt is sufficient in amount, but deficient in number. This conclusion seems to suggest that one droplet produces many minute secondary salt nuclei while it stays in the air and evaporates (**35**, **36**, **37**, **38**, **39**, **40**), although giant sea-salt nuclei may coalesce one another as shown in **5.3**.

Acknowledgements

The author wishes to express his sincere gratitude to Prof. Shōitirō Hayami for his cordial guidance and encouragement throughout this study. He thanks

to Assis. Prof. Hideaki Kunishi for numerous advices. He also thanks to Mr. Haruo Higuchi and other members of the Ujigawa Hydraulics Laboratory of Disaster Prevention Research Institute, Kyoto University, who provided facilities in carrying out the present experiment.

REFERENCES

1. S. G. Boyce, The salt spray community, Ecological Monogr., **24** (1954), 29.
2. A. H. Woodcock, C. F. Kientzler, A. B. Arons and D. C. Blanchard, Giant condensation nuclei from bursting bubbles, Nature, **172** (1953), 1145.
3. C. F. Kientzler, A. B. Arons, D. C. Blanchard and A. H. Woodcock, Photographic investigation of the projection of droplets by bubbles bursting at a water surface, Tellus, **6** (1954), 1.
4. F. Knelman, N. Dombrowski and D. M. Newitt, Mechanism of the bursting of bubbles, Nature, **173** (1954), 261.
5. D. J. Moore and B. J. Mason, The concentration, size distribution and production rate of large salt nuclei over the oceans, Quart. J. Roy. Meteor. Soc., **80** (1954), 583.
6. B. J. Mason, Bursting of air bubbles at the surface of sea water, Nature, **174** (1955), 470.
7. D. C. Blanchard and A. H. Woodcock, Bubble formation and modification in the sea and its meteorological significance, Tellus, **9** (1957), 145.
8. S. Hayami and Y. Toba, Drop production by bursting of air bubbles on the sea surface (I). Experiments at still sea water surface, J. Oceanogr. Soc. Japan, **14** (1958), 145.
9. K. Isono, Microphysical processes in precipitation mechanism, Japanese J. Geophys., **2** (1959), 1.
10. H. Kunishi, On design of resistive wave meter, Dis. Prev. Res. Inst. Annuals, **3** (1959), 65.
11. Y. Toba, Observation of sea water droplets by filter paper, J. Oceanogr. Soc. Japan, **14** (1958), 151.
12. K. R. May, Apparatus for coating surfaces with magnesium oxide, J. Sci. Instr., **17** (1940), 231.
13. K. R. May, The cascade impactor. An instrument for sampling coarse aerosols, J. Sci. Instr., **22** (1945), 187.
14. K. R. May, The measurement of airborne droplets by the magnesium oxide method, J. Sci. Instr., **27** (1950), 128.
15. A. H. Woodcock and M. M. Gifford, Sampling atmospheric sea-salt nuclei over the ocean, J. Marine Res., **8** (1949), 177.
16. W. H. Munk, High frequency spectrum of ocean waves, J. Marine Res., **14** (1955), 302.
17. A. H. Schooley, Profiles of wind-created water waves in the capillary-gravity transition region, J. Marine Res., **16** (1958), 100.
18. P. J. H. Unna, White horses, Natare, **148** (1941), 226.
19. W. H. Munk, A critical wind speed for air-sea boundary processes, J. Marine Res., **6** (1946), 203.
20. G. D. Crapper, An exact solution for progressive capillary waves of arbitrary amplitude, J. Fluid Mech., **2** (1957), 532.
21. R. L. Datta, D. H. Napier and D. M. Newitt, The properties and behaviour of gas bubbles formed at a circular orifice, Trans. Instn Chem. Engrs., **28** (1950), 14.
22. O. Stuhlman, Jr., The mechanics of effervescence, Physics, **2** (1932), 457.
23. D. M. Newitt, N. Dombrowski and F. H. Knelman, Liquid entrainment I. The mechanism of drop formation from gas or vapour bubbles, Trans. Instn Chem. Engrs., **32** (1954), 244.
24. Y. Toba, Drop production by bursting of air bubbles on the sea surface (II). Theoretical study on the shape of floating bubbles, J. Oceanogr. Soc. Japan, **15** (1959), 121.

25. S. Okuda and S. Hayami, Experiments on evaporation from wavy water surface, Rec. Oceanogr. Works Japan, **5** (New series) (1959), 6.
26. W. R. Lane and H. L. Green, The mechanics of drops and bubbles in *Surveys in Mechanics* (Cambridge University Press, 1956), 162.
27. H. Kunishi, Unpublished paper.
28. K. Brocks, Measurements of wind profiles over the sea and the drag at the sea surface, International Oceanographic Congress, Preprints (1959), 742.
29. E. Eriksson, The yearly circulation of chloride and sulfur in nature; meteorological and pedological implications, Tellus, **11** (1959), 375; **12** (1960), 63.
30. A. H. Woodcock, Salt nuclei in marine air as a function of altitude and wind force, J. Meteor., **10** (1953), 362.
31. A. H. Woodcock, Atmospheric sea-salt nuclei data for Project Shower, Tellus, **9** (1957), 521.
32. I. Kita and T. Aya, Observation of the scattering of saline drops near the seashore inland by strong wind. J. Meteor. Res., **11** (1959), 373 (in Japanese).
33. E. Eriksson, Composition of atmospheric precipitation, Tellus **4** (1952), 215; 280.
34. B. J. Mason, *The Physics of Clouds* (Clarendon Press, Oxford, 1957).
35. H. Dessens, Les noyaux de condensation de l'atmosphére, C. R. Acad. Sci., **223** (1946), 915.
36. Y. Miyake, The chemical nature of the saline matter in the atmosphere, Geophys. Mag., **16** (1948), 64.
37. K. Sugawara, S. Oana and T. Koyama, Separation of the components of atmospheric salt and their distribution, Bull. Chem. Soc. Japan, **22** (1949), 47.
38. T. Koyama and K. Sugawara, Separation of the components of atmospheric salt and their distribution (continued), Bull. Chem. Soc. Japan, **26** (1953), 123.
39. W. E. Ranz and W. R. Marshall, Evaporation from drops, Chem. Engr. Prog., **48** (1952), 141; 173.
40. S. Twomey and K. N. McMaster, The production of condensation nuclei by crystallizing salt particles, Tellus, **7** (1955), 458.

Memoirs of the College of Science, University of Kyoto, Series A,
Vol. XXIX, No. 3, Article 5, 1961.

NMR PULSE APPARATUS AND ITS APPLICATION TO THE INVESTIGATION OF INTERNAL MOTION OF HIGH POLYMER (POLY-PROPYLENE)

BY

Akira HIRAI and **Takao KAWAI**

(*Received March 17, 1961*)

ABSTRACT

After detailed report in this Memoirs of a NMR pulse apparatus, some improvements were made on the apparatus. The first part of this paper deals with the construction of the improved parts and the second part with the application of the improved apparatus to the investigation of the internal motion of high polymer (poly-propylene). As a result, we could definitely separate the internal motions of poly-propylene, into the segmental motion, and the internal motion of methyl groups. The experimental data about the spin lattice relaxation time (T_1) for internal motion of methyl groups were analysed following BPP theory, and b, τ_0 and ΔE were determined to be 2.2 A, 4×10^{-12} sec and 1.9 Kcal/mol respectively.

1. Introduction

The spin lattice relaxation time (T_1) in nuclear magnetic resonance (NMR) is a very useful quantity for investigations of the dynamical character of substances. To measure T_1 of proton, particularly in high polymers, we had constructed a NMR pulse apparatus, whose detailed description was already reported in this Memoirs (hereafter referred to as I) (**1**). Some results obtained by using that apparatus to investigate the sorbed water (**2**) and the segmental motion of some high polymers (**3**) were also reported. In performing experiments we realized the necessity to improve the apparatus such that the stability of apparatus is increased, the stronger rf pulse is obtained, and T_1 at lower temperatures (at least, as low as liquid nitrogen temperature) and the spin echo decay time (T_2) can be measured.

In the first part we shall report the construction of the improved apparatus, though there are several papers published about the NMR pulse apparatus, (**4**, **5**, **6**), since the data on T_1 for various substances are now demanded by many researchers and the apparatus for measuring T_1 is not fully commercialized.

In the second part we shall describe the application of this improved NMR apparatus to the investigation of the internal motion of poly-propylene, as a

typical example of the study by using the NMR pulse apparatus.

2. Construction of improved apparatus

The whole block diagram of the improved apparatus is given in Fig. 1, where improved parts are shown by double boxes. Other parts are the same as reported in I. For measurements of T_1 and T_2, the 90°-90° pulse method was used (**7**). All experiments were performed at 25 Mc/sec, which corresponds to about 6000 gauss for proton. A detailed description of the improved parts are given below.

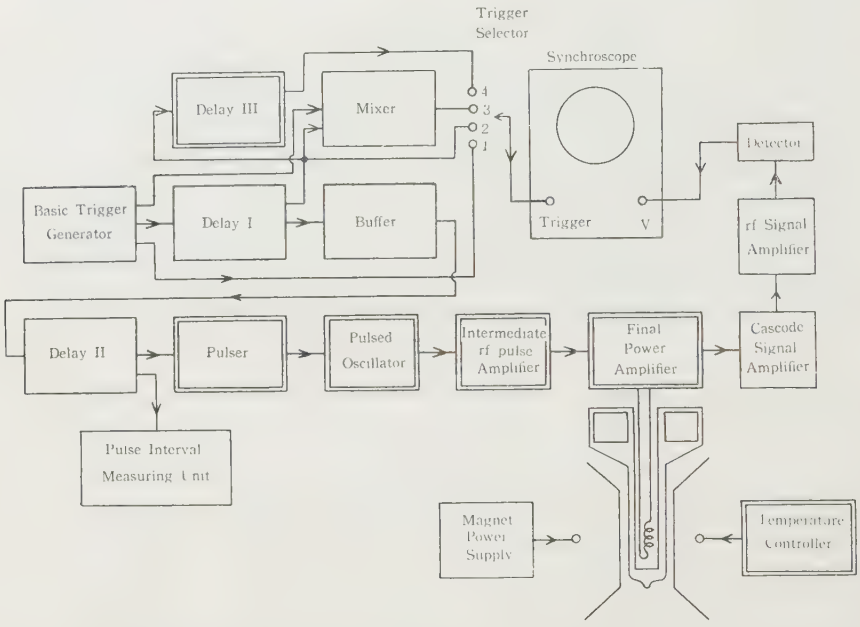

Fig. 1. Block diagram of the whole apparatus, where the improved parts are shown by double boxes.

(A) *Pulser and pulsed oscillator*

The circuit diagram is shown in Fig. 2. For pulser, a plate coupled monostable multivibrator with plate catching diode (8) is used, since it provides better performance than the previous one for narrow pulses. By proper choice of R and C elements, an appropriate pulse width for 90° pulse was obtained. Negative gate pulse from this pulser initiates oscillation of the next Hartley type pulsed oscillator (**9**). The rf pulse of small amplitude thus obtained is then amplified by the following amplifier stage.

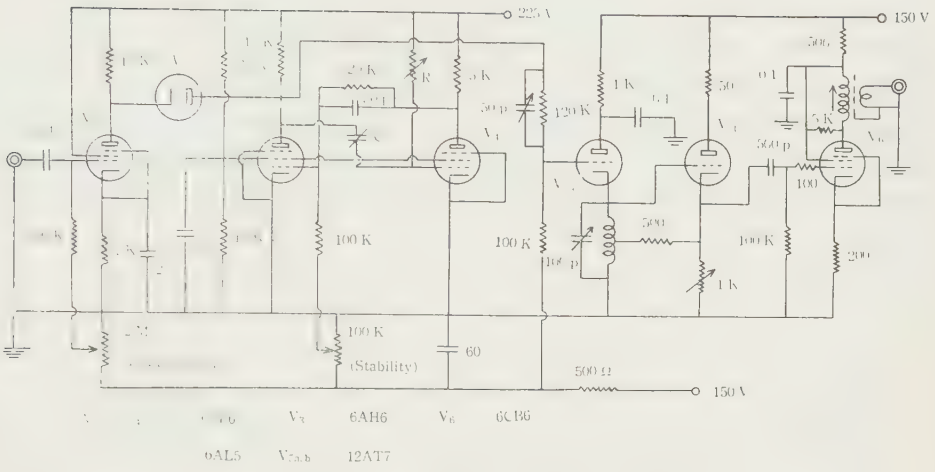

Fig. 2. Circuit diagram of pulser and pulsed oscillator.

(B) *Intermediate rf pulse amplifier*

Fig. 3 shows the circuit diagram. In this stage, the rf pulse of small amplitude from pulsed oscillator is amplified to drive the next final power amplifier. The stability and the wide band width are important in this stage, the overall band width being about 1 Mc/sec.

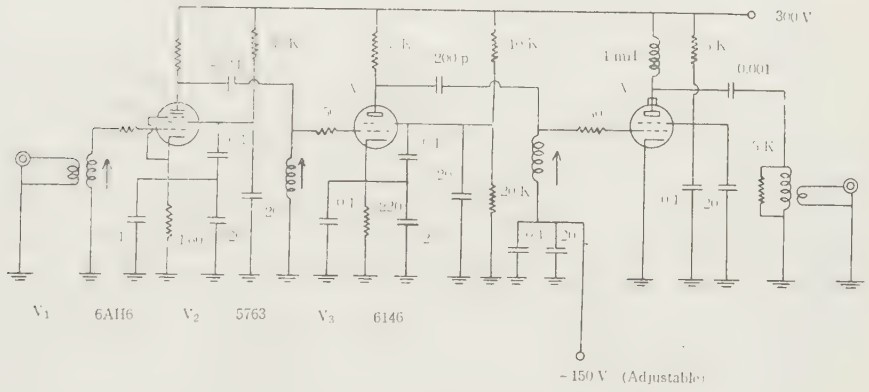

Fig. 3. Circuit diagram of intermediate rf pulse amplifier.

(C) *Final power amplifier and associated circuits*

Fig. 4 shows the circuit diagram. The previously used gas flow type cryostat was replaced by the Gutowsky type (**10**). The sample coil is composed of 12 turns of BS 16 enamelled copper wire 1.1 cm in inside diameter and 1.6 cm long, to which are shunted the capacity of rigid coaxial line included in Dewar jar,

the capacity of low capacitance coaxial cable about 40 cm long, a variable condenser, and the output capacity of power tube (Eimac 4-125A), to constitute a resonance circuit of 25 Mc/sec. This resonance circuit serve both as a plate load of the power tube and as an input circuit to the nuclear signal receiver. Eimac 4-125A seems to be the best choice for our purpose, owing to low output capacity and moderate power handling capacity. The pulse width for 90° pulse was about 5μ sec.

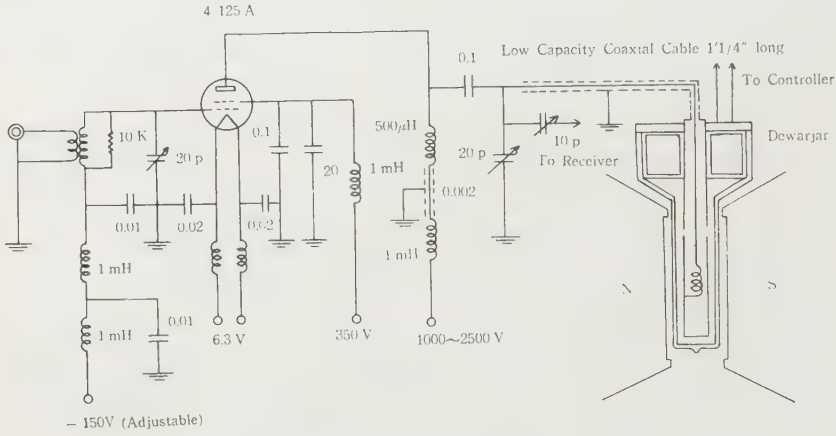

Fig. 4. Circuit diagram of final power amplifier and associated circuits.

(D) *Delay III*

This circuit was attached in order to measure the spin echo decay time (T_2). If the time interval between the first pulse and the second is τ, the spin echo signal appears after the time interval 2τ from the first pulse. The time delay of delay III should be equal to that of delay I. Delay III was a monostable multivibrator as was delay I, as described in I. R and C elements in both delays, which determine the time delay, have accuracy of 0.5% and are ganged. If the synchroscope trigger selector is set at 4 (Fig. 1), only the spin echo signal appears on synchroscope screen. This spin echo signal decays exponentially with the time constant T_2, when we vary the pulse interval τ.

(E) *Temperature controller*

This is a commercial product. The voltage from the copper constantan thermocouple is compared with a pre-set standard voltage and the error voltage is used for automatic temperature control. The constancy of cryostat is about ± 1°C for a temperature range above room temperature and near the liquid nitrogen temperature, and falls to about ± 3°C between them, due to performance of the cryostat.

The procedure of measuring T_1 was already reported in I. Accuracy in measuring T_1 is about $\pm 5\%$ under good S/N condition and about $\pm 30\%$ or more under bad condition (such as at lower temperatures in the present case).

Now, we consider the nuclear signal amplitude just after the first pulse (y_1). In principle, y_1 is proportional to the number of resonant nuclei. However, our apparatus cannot detect the nuclear signal of protons in rigid state. This is because the pulse width for 90° pulse (t_w) is not so narrow and the receiver recovery time (t_{dead}) is not so small as to detect the resonance signal of protons in rigid state. Rough estimation can be made as follows. Assume that the resonance line can be described by Bloch equation with T_1 of infinity and T_2 of $2/\gamma \cdot \Delta H_{1/2}$ (**11**) (which is a very rough approximation in solid (**12**)), and further assume an exact resonance excitation. Then, the ratio of apparent nuclear signal amplitude just after the first pulse for broad line (long T_2) to that for narrow line (short T_2) becomes $\exp(-t_w/2T_2) \cdot \exp(-t_{dead}/T_2)$ (**13**). Inserting the values $t_w = 5\mu$ sec, $t_{dead} = 15\mu$ sec and $\Delta H_{1/2} = 10$ gauss (typical values for proton in rigid state), we obtain the value of 0.1. So we can roughly consider that y_1 is proportional to the number of moving protons. The accuracy in measuring y_1 is not so good and about $\pm 30\%$, since y_1 critically depends on various factors, such as resonance condition, 90° pulse setting, filling factor of the sample, etc. However, careful measurement of y_1 is very helpful for interpreting the data on T_1, as in the study of the sorbed water (**2**) and in the present case (see below).

3. Study of internal motions of poly-propylene

As an example of the application, we shall report the investigation of the internal motion of poly-propylene (PP) $(-CH_2-CHCH_3-)_n$. This polymer has been already studied by steady state NMR method by several workers (**14**, **15**, **16**, **17**). Their main interests consisted in effects of crystallinity, steric configuration and segmental motion near glass transition temperature on NMR line width. We have studied the internal motion of this polymer, particularly the internal motion of methyl groups. For this kind of study, the NMR pulse method is very powerful, as one of the authors (T. K.) reported concerning the study of internal motions of acryl and methacryl group high polymers (**18**).

The sample used was commercial product of Moplen M-2 manufactured by Montecatini Co. and kindly supplied through Dr. K. Hayashi of Japanese Association of Radiation Research on polymers. The degrees of tacticity and crystallinity of the sample were about 60~70%.

The experimental results of the temperature dependence of T_1 and T_2 of proton of PP are shown in Fig. 5, where plots of the values of T_1 and T_2 *versus*

$1/T$ are given on semi-logarithmic scale. T_2 cannot be measured below 70°C, where no spin echo signal appears. The temperature dependence of y_1 is also shown in Fig. 5 in linear arbitrary scale.

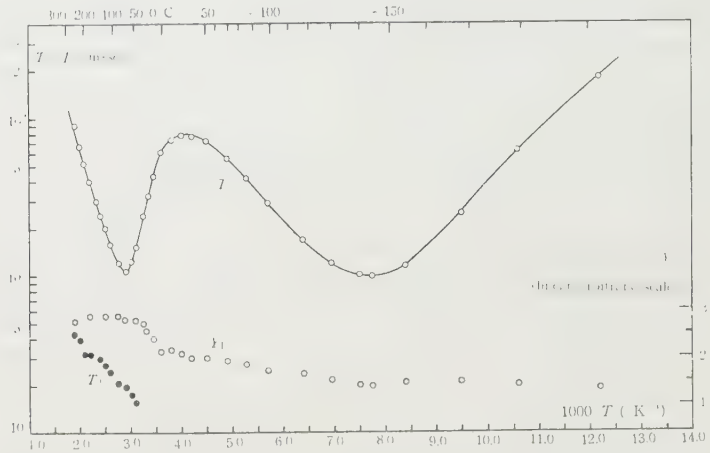

Fig. 5. Experimental data of temperature dependence of T_1, T_2 and y_1 for proton of poly-propylene.

As to T_1, one V-shaped part of T_1 *versus* $1/T$ curve corresponds to one mode of internal motion, according to BPP theory (**19**), even if there would be a distribution of correlation time. In our experimental results, the V shaped part at higher temperatures corresponds to the segmental motion of PP, and that at lower to the internal motion of methyl groups. The data on temperature dependence of y_1 supports this, since the experimental ratio of y_1 at higher temperatures to that at lower was abont 2 : 1, while this ratio is expected to be 6 : 3, considered from the molecular structure of PP. Our qualitative result about the internal motions in PP, which are occurring in each temperature range, is consistent with the results obtained by the steady state NMR method (**14**~**17**).

Now, we shall analyse the experimental result of the temperature dependence of T_1 for internal motion of methyl groups, following BPP formula, based on "single correlation time (τ_c)". According to it (**19**, **20**),

$$\frac{1}{T_1} = \frac{3}{10}\frac{\gamma^4 h^2}{b^6}\left\{\frac{\tau_c}{1+\omega^2\tau_c^2} + \frac{4\tau_c}{1+4\omega^2\tau_c^2}\right\},$$

where b is the "effective" interproton distance. Further we consider the internal motion in high polymers as an activation process, then

$$\tau_c \quad \tau_0 \exp\left(\frac{\Delta E}{RT}\right).$$

Considering b, τ_0 and ΔE as three adjustable parameters, we can analyse the data, that is, the minimum value of T_1 gives b, and the temperature dependence of τ_c gives τ_0 and ΔE. The plots of τ_c *versus* $1/T$ are given in Fig. 6. The results of analysis are: $b=2.2$A, $\tau_0=4\times10^{-12}$ sec and $\Delta E=1.9$ Kcal/mol for the internal motion of methyl groups in PP. These values are of the same order of magnitude as those obtained for alkyl groups in acryl and methacryl group high polymers (**18**).

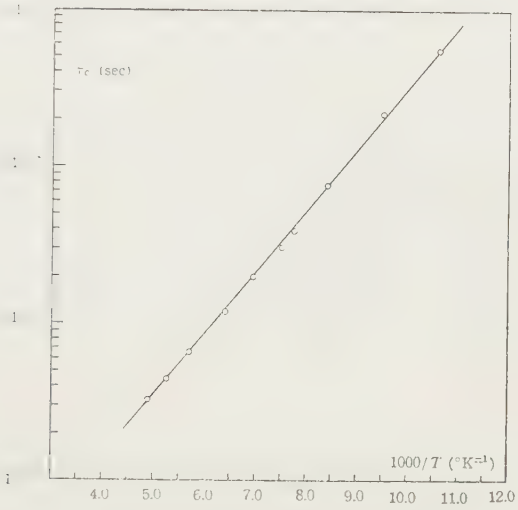

Fig. 6. τ_c (obtained by BPP formula from data of T_1) *versus* $1/T$ for methyl group proton of poly-propylene.

As to T_2, no definite and significant conclusions could be obtained from the data. The data on T_2 would be useful for such studies as on the sorbed water (**2**). It may be noted, however, that the value of T_2 of proton in high polymers is by about one order of magnitude smaller than the value of T_1 as in the case of the sorbed water (**2**).

The effect of crystallinity and steric configuration upon the value of T_1 is not clear from our present study. We are planning to study the effect systematically by performing more accurate measurements on simpler and more refined samples.

Acknowledgements

The authors would like to express their sincere thanks to Prof. I. Takahashi and Prof. T. Hashi for their continual interests and discussions. Their thanks are also due to members of our laboratory for assistances.

REFERENCES

1. T. Hashi, A. Hirai, M. Sasaki and T. Kawai; Memoirs of the College of Science, University of Kyoto, Series **A29** (1959), 205.
2. M. Sasaki, T. Kawai, A. Hirai, T. Hashi and A. Odajima; J. Phys. Soc. Japan **15** (1960), 1652.
3. T. Kawai, M. Sasaki, A. Hirai, T. Hashi and A. Odajima; J. Phys. Soc. Japan **15** (1960), 1700.
4. J. Schwartz; Rev. Sci. Instr. **28** (1957), 780.
5. J. C. Bucha, H. S. Gutowsky and D. E. Woessner; Rev. Sci. Instr. **29** (1958), 55.
6. K. Luszczynski and J. G. Powles; J. Sci. Instr. **36** (1959), 57.
7. E. L. Hahn; Phys. Rev. **80** (1950), 580.
8. See, e.g. J. Millman and H. Taub, *Pulse and Digital Circuits* (McGraw-Hill Book Co., New York, 1956), p. 174 ff.
9. See, e.g. Reference 8, p. 504 ff.
10. H. S. Gutowsky, L. H. Meyer and R. E. McClure; Rev. Sci. Instr. **24** (1953), 644.
11. F. Bloch; Phys. Rev. **70** (1946), 460.
12. K. Tomita; Prog. Theor. Phys. **19** (1958), 541.
13. H. C. Torrey; Phys. Rev. **76** (1949), 1059.
14. M. P. Slichter and E. R. Mandel; J. Chem. Phys. **29** (1958), 232.
15. M. P. Slichter and E. R. Mandel; J. Appl. Phys. **29** (1958), 1438.
16. J. A. Sauer, R. A. Wall, N. Fuschillo and A. E. Woodwards; J. Appl. Phys. **29** (1958), 1385.
17. A. Nishioka, Y. Koike, M. Owaki, T. Naraba and Y. Kato; J. Phys. Soc. Japan **15** (1950), 416.
18. T. Kawai; J. Phys. Soc. Japan (to be published)
19. N. Bloembergen, H. S. Purcell and R. V. Pound; Phys. Rev. **73** (1948), 679.
20. R. Kubo and K. Tomita; J. Phys. Soc. Japan **9** (1954), 888.

Memoirs of the College of Science, University of Kyoto, Series A,
Vol. XXIX, No. 3, Article 6, 1961.

ELECTRON DENSITY MEASUREMENT BY MICROWAVE INTERFEROMETER

BY

Shigetoshi TANAKA

(Received March 17, 1961)

ABSTRACT

The relative phase shift of the electromagnetic wave propagating through a uniform plasma in a waveguide section was derived. By a microwave interferometer which has a waveguide section filled with a stationary gaseous discharge plasma in the test path, the relative phase shift and hence the electron density was measured at 10 *GC/S* as a function of tube current. At the same time, the electron density was measured by using Langmuir probe. The electron density measured by Langmuir probe was always several times larger than that by microwave method. The difference can be explained, assuming a spatial distribution of the electron density in the discharge plasma.

1. Introduction

Microwave techniques have been used for the study of electron loss process in the afterglow of gaseous discharge (**1**, **2**, **3**, **4**). The so-called microwave diagnostics of plasma has prospered recently in connection with the problems of the controlled thermonuclear fusion (**5**, **6**). There are three methods to measure electron density and collision frequency of electron in plasma, that is, cavity method (**7**), reflection method (8) and propagation method. In the propagation method it is common to use the microwave interferometer in which the plasma is either confined in a waveguide section or in a free space (**9**, **10**).

In this paper, we have derived a relation between the electron density and the relative phase shift, as well as that between the collision frequency and the attenuation, when the wave propagates in a waveguide section filled with uniform plasma. Using these relations, we have measured the electron density as a function of tube current. However, the measured values were different from those measured by Langmuir probe. The difference is naturally expected, since by Langmuir probe method the electron density is locally measured, whereas in microwave method the whole plasma space is effective.

Although we could not derive a relation between both values, the difference was explained by considering a spatial electron density distribution in plasma.

2. Theory of experiment

The wave propagating in a guide filled with uniform isotropic plasma is considered. If the cross section of the guide is uniform, the electric vector propagating along the z-axis, which is the guide axis, is given by (**11**):

$$\boldsymbol{E}(x, y) \exp(-j\omega t + jhz),$$

with

$$h^2 = k^2 - k_c^2 = k_0^2 K - k_c^2,$$

where $K = K_{re} + jK_{im}$ is the specific inductive capacity, $k_c = 2\pi/\lambda_c$ and λ_c is the cutoff wavelength. h can be represented in terms of the phase constant β_p and the attenuation constant α_p as:

$$h = \beta_p + j\alpha_p \qquad (\beta_p > 0, \quad \alpha_p \geqq 0), \tag{1}$$

where

$$\beta_p = \frac{k_0}{\sqrt{2}} \left\{ K_{re} - \left(\frac{k_c}{k_0}\right)^2 \right\}^{1/2} \left[1 + \left\{ 1 + \left(\frac{K_{im}}{K_{re} - (k_c/k_0)^2} \right)^2 \right\}^{1/2} \right]^{1/2}, \tag{2}$$

and

$$\alpha_p = \frac{k_0}{\sqrt{2}} \left\{ K_{re} - \left(\frac{k_c}{k_0}\right)^2 \right\}^{1/2} \left[-1 + \left\{ 1 + \left(\frac{K_{im}}{K_{re} - (k_c/k_0)^2} \right)^2 \right\}^{1/2} \right]^{1/2}. \tag{3}$$

Thus, the relative phase shift $\Delta\theta_g$ and the attenuation α_g per λ_g are given by:

$$\Delta\theta_g = 2\pi \left\{ 1 - \frac{1}{\sqrt{2}} \frac{\lambda_g}{\lambda} \left\{ \left(\frac{\lambda}{\lambda_g} \right)^2 - \frac{\eta}{1+\beta^2} \right\}^{1/2} \left[1 + \left\{ 1 + \left(\frac{\eta\beta/(1+\beta^2)}{(\lambda/\lambda_g)^2 - \eta/(1+\beta^2)} \right)^2 \right\}^{1/2} \right]^{1/2} \right\}, \tag{4}$$

and

$$\alpha_g = \frac{2\pi}{\sqrt{2}} \frac{\lambda_g}{\lambda} \left\{ \left(\frac{\lambda}{\lambda_g} \right)^2 - \frac{\eta}{1+\beta^2} \right\}^{1/2} \left[-1 + \left\{ 1 + \left(\frac{\eta\beta/(1+\beta^2)}{(\lambda/\lambda_g)^2 - \eta/(1+\beta^2)} \right)^2 \right\}^{1/2} \right]^{1/2}, \tag{5}$$

where $\eta = (\omega_p/\omega)^2$ and $\beta = \nu_c/\omega$, ω_p is the plasma frequency, ν_c the collision frequency and λ_g the air-filled guide wavelength. (4) and (5) reduce to the free space propagation with $\lambda_c \to \infty$, hence $\lambda_g \to \lambda$.

For $\beta^2 \ll 1$, (4) becomes:

$$\Delta\theta_g = 2\pi \left[1 - \left\{ 1 - (\lambda_g/\lambda)^2 \eta \right\}^{1/2} \right] \qquad (\text{radian}/\lambda_g). \tag{6}$$

Moreover, if $(\lambda_g/\lambda)^2 \eta \ll 1$, (6) can be approximated by:

$$\Delta\theta_g = \pi (\lambda_g/\lambda)^2 \eta. \tag{7}$$

For the free space, the critical condition for wave propagation is given by $\eta = 1$. For the waveguide, the condition becomes:

$$k_0^2 K_{re} - k_c^2 = 0 \quad \text{or} \quad \eta = (\lambda/\lambda_g)^2, \tag{8}$$

which is satisfied for the smaller electron density η, because of $\lambda < \lambda_g$. In addition, if we set the signal frequency and the dimensions of waveguide appropriately in such a way that λ/λ_g takes an arbitrary value smaller than unity, we can principally determine the electron density from the critical condition.

In Fig. 1 are plotted the relative phase shifts $\Delta\theta_g$, assuming the TE_{10}-mode wave propagating in an X-band waveguide, and $\Delta\theta$ for the free space as functions of η. It is evident that in Fig. 1 $\Delta\theta_g$ is larger than $\Delta\theta$, so we can measure the lower electron density by the waveguide propagation than by the free space one, for the same minimum detectable phase shift.

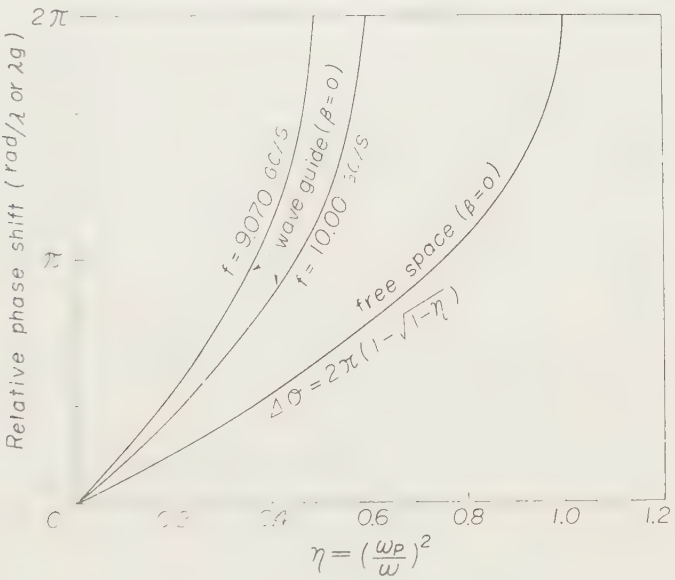

Fig. 1. Relative phase shifts in uniform plasma.

3. Experimental equipment

The block diagram of the microwave interferometer is given in Fig. 2. An experimental discharge tube is inserted in a specially designed square waveguide section, a side length of which is equal to the larger side length of the standard guides, which are connected on both sides through tapered ones. The experimental discharge tube is shown in Fig. 3. The holes of the guide wall, through which the discharge tube is inserted, is desired to be as small as possible, so the tube is made slender in two parts. The tube is also equipped with a Langmuir probe, consisting of wolfgang wire (0.70 mm in diameter and 0.34 mm in length). The filled gases and gas pressures of each tube are given in Table 1.

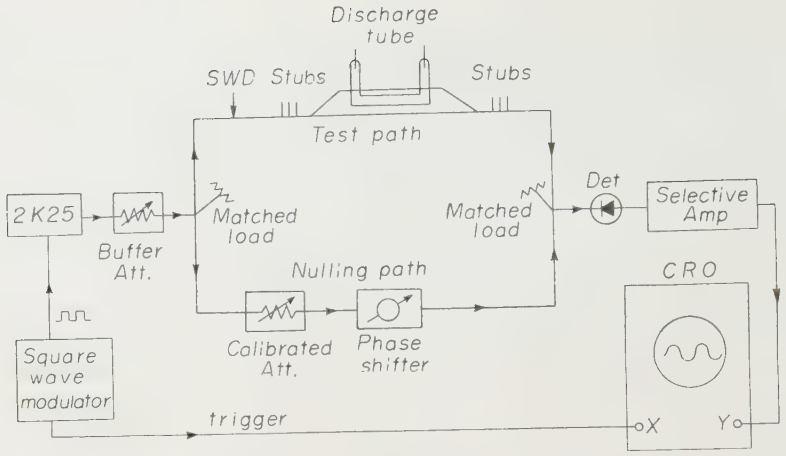

Fig. 2. Block diagram of microwave interferometer.

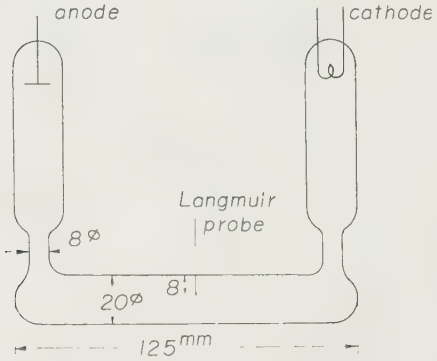

Fig. 3. Discharge tube.

Table 1.

Tube No.	Filled gas and pressure	N_1 (cm^{-3})	N_2 (cm^{-3})	N_2/N_1	$T_e(^0K)$
1	Ar (1 mmHg) + Hg	3.0×10^{11}	—	—	—
2	Ar (0.5) + Hg	2.1×10^{11}	5.4×10^{11}	2.6	2.7×10^4
3	He (0.93)	$8.0\sim12\times10^{10}$	3.6×10^{11}	3.0~4.5	5.2×10^4
4	He (0.27)	$2.0\sim3.3\times10^{10}$	1.0×10^{11}	3~5	6.8×10^4

By adjusting the attenuator and the phase shifter in the nulling path, we measure the microwave attenuation and the phase shift in plasma, then we can calculate η and β, and hence the electron density and the collision frequency by (4) and (5). Further we measure the voltage-current characteristics of Langmuir probe, and calculate the electron density and temperature, for comparison.

4. Experimental results

In calculating the electron density from the phase shift, the attenuation terms are neglected and (6) is used, since the gas pressure is less than one mm Hg in our experiment. Next, in measuring the phase shift, the effect due to the impedance mismatching caused by plasma is estimated as follows. When there is no plasma, the phase shift due to the mismatching in the test path is measured at various VSWR's by adjusting the stubs. The shift due to the mismatching of the plasma-filled guide is estimated from VSWR at various tube currents.

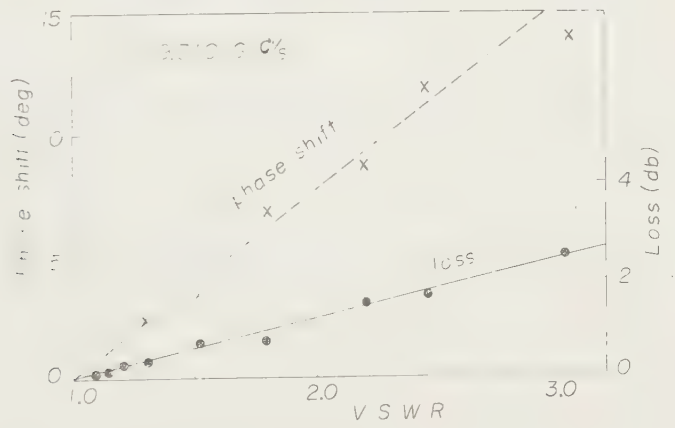

Fig. 4. Phase shift and attenuation due to mismatching in test path (f=9.310 *GC/S*).

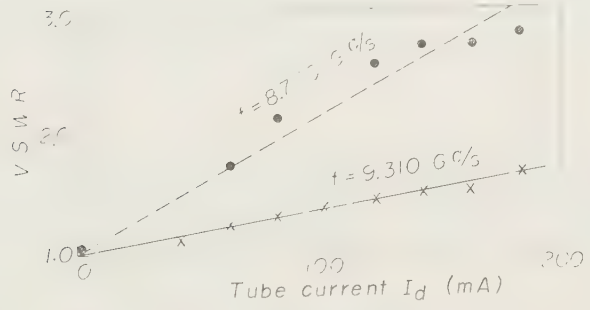

Fig. 5. VSWR *versus* tube current (tube No. 3).

In Fig. 4 are plotted the phase shift and the attenuation due to the mismatching at the frequency $f=9.310$ *GC/S*. The measured VSWR is plotted against the tube current in Fig. 5. In our measurements, however, the phase shifts due to

mismatching are considerably small in comparison with those in plasma, so they have been neglected in measurements of the phase shifts in plasma. In Fig. 6 are plotted the electron densities *versus* the tube current. The values by Langmuir probe are several times larger than those by microwave method. We shall discuss it later. In Table 1 are given the electron density N_1 measured by microwave method, the electron density N_2 measured by Langmuir probe, the ratio N_2/N_1 and the electron temperature T_e at the tube current I_d 200 mA for each discharge tube.

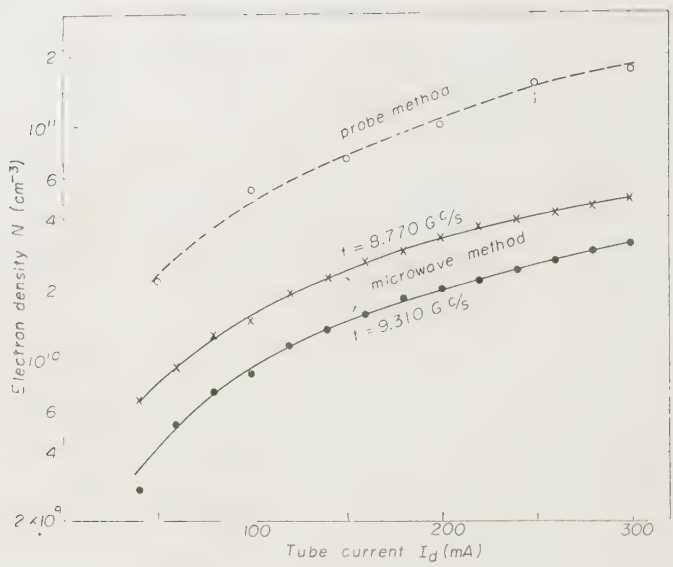

Fig. 6. Electron density *versus* tube current (tube No. 4).

In measurement of the microwave attenuation due to plasma, the apparent loss α_0 in test path measured by adjusting the attenuator in nulling path can be given by the sum:

$$\alpha_0 = \alpha_1 + \alpha_2 + \alpha_3 ,$$

where α_1 is the loss in the plasma, α_2 is the loss due to the reflection by mismatching, and α_3 is the leakage loss through the holes of guide wall. α_2 can be estimated by measuring VSWR, but the leakage can not. The apparent loss α_0 in test path as a function of tube current is plotted in Fig. 7, though the collision frequency of electron cannot be calculated directly from this curve.

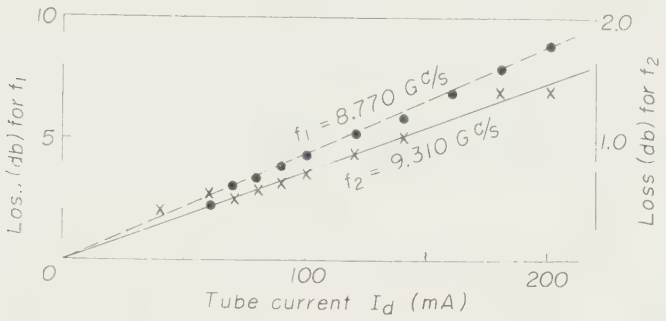

Fig. 7. Apparent loss *versus* tube current (tube No. 3)

5. Discussion

As stated above, the electron density measured by Langmuir probe was always several times larger than that measured by microwave method. The reason for the difference between these two seems to be as follows. In Langmuir probe method, the electron density at the point where the probe is located is measured, while in microwave method, the electron density somehow averaged over the plasma-filled guide space is effective for the total relative phase shift. For example, if the density distribution is three-dimensionally sinusoidal in space, the maximum density N_m is $(\pi/2)^3 \simeq 3.9$ times the averaged density N. On the other hand, if the plasma in a guide is uniform along the axis, but the density distribution is sinusoidal in the cross section, $N_m/N = (\pi/2)^2 \simeq 2.5$. Therefore, the ratio N_2/N_1 - 3~4 of the present experiments is to be expected, since Langmuir probe was inserted near the centre of the plasma column.

In conclusion, the microwave interferometer seems to provide a convenient and easy method for measuring the average electron density in gaseous discharge plasmas.

Acknowledgments

The author wishes to express his sincere thanks to Prof. I. Takahashi for his guidance and to Messrs. R. Itadani and H. Kubo for help in preparing the discharge tubes and the apparatus.

REFERENCES

1. L. Goldstein: *Advances in Electronics and Electron Physics,* edited by L. Marton (Academic Press, Inc., N. Y., 1955), Vol. 7. p. 399.
2. M. A. Biondi and S. C. Brown: Phys. Rev. **75** (1949), 1700.
3. L. J. Varmerin: Phys. Rev. **84** (1951), 563.
4. J. M. Anderson and L. Goldstein: Phys. Rev. **100** (1955), 1037.
5. S. C. Brown: 2nd International Conf. on the Peaceful Uses of Atomic Energy (1958) P/385.

6. C. B. Wharton: UCRL-4836 (Rev.) (1957).
7. S. C. Brown and D. J. Rose: J. Appl. Phys. **23** (1952), 711, 719.
8. L. Goldstein and T. Sekiguchi: Phys. Rev. **109** (1958), 625.
9. R. F. Whitmer: Phys. Rev. **104** (1956), 572.
10. L. Goldstein, *et al.*: Elec. Commun. **29** (1952), 243.
11. J. C. Slater: *Microwave Electronics* (D. Van Nostrand Co., New York, 1950).

Memoirs of the College of Science, University of Kyoto, Series A,
Vol. XXIX, No. 3, Article 7, 1961.

ABSORPTION AT ELECTRON CYCLOTRON RESONANCE IN SLIGHTLY IONIZED GASES (I)*

BY

Shigetoshi TANAKA

(*Received March 17, 1961*)

ABSTRACT

An expression of the absorption at cyclotron resonance was derived by using the specific inductive capacity, for the microwave propagating in a slightly ionized gas along the static magnetic field. It coincided with that derived by Brown *et al.* from the conductivity. It was shown that the cyclotron resonance occurs at $\omega=\omega_c$, the absorption curve is Lorentzian, and the half-width gives a direct measure of the collision frequency.

Approximate expressions of ordinary refractive index and extinction coefficient for the right-handed and the left-handed circularly polarized waves were derived.

1. Introduction

There have been some reports concerning the absorption at electron cyclotron resonance in a slightly ionized gas, both theoretical and experimental (**1, 2, 3, 4**). Solving the Boltzmann equation for the distribution of electrons under the influence of both constant magnetic field and high-frequency electric field, Kelly, Margenau and Brown have shown that the absorption i. e. the real conductivity exhibits a Lorentzian resonance peak and the half-width of this curve gives a direct measure of the collision frequency for the constant mean free time. It was also found that for the constant mean free path, though the absorption curve is complicated, the half-width is practically equal to that for the former case of constant mean free time and the line shape is not very sensitive to the collision cross section depending upon electron velocity (**5**).

In the microwave diagnostics of plasma, however, it is commonly and easily done to measure the phase shift and the insertion loss of the microwave in the plasma, from which one can calculate the electron density and the collision frequency (**6, 7**). Therefore, it is necessary for the experimental study of plasmas to derive the expressions for the attenuation factor and the phase shift at electron cyclotron resonance.

* Reported in Japanese in "Kakuyugo Kenkyu (Nuclear Fusion Research)" **4** (June, 1960), 540.

Drummond (8) has made detailed calculation for the very dense, hot magnetoplasma. However, since his results are extremely complicated, his analysis is not easily used for discussing the experimental results on a slightly ionized gas.

It is the purpose of the present paper to derive approximate expressions for the attenuation factor and the phase shift in the vicinity of the electron cyclotron resonance for the slightly ionized gas, which are useful for the analyses of experimental results.

The electron cyclotron resonance occurs when an electromagnetic wave has a transversal component to a static magnetic field $\boldsymbol{B}$, the behaviour depending on the direction of propagation $\boldsymbol{k}_0$. For the two interesting cases: (i) $\boldsymbol{k}_0 /\!/ \boldsymbol{B}$, (ii) $\boldsymbol{k}_0 \perp \boldsymbol{B}$, the calculations were carried out using the specific inductive capacity. The absorption curve which represents the attenuation factor near the electron cyclotron resonance is Lorentzian for the transversal wave ($\boldsymbol{k}_0 /\!/ \boldsymbol{B}$)*. On the contrary, for the hybrid wave ($\boldsymbol{k}_0 \perp \boldsymbol{B}$) the resonance curve not only appears non-Lorentzian, but also the resonance position shifts. The case of $\boldsymbol{k}_0 /\!/ \boldsymbol{B}$ is considered in the first part, that of $\boldsymbol{k}_0 \perp \boldsymbol{B}$ in the second and the experimental results are given in the third part of the present paper.

2. Dispersion of the right-handed circularly polarized wave

A linearly polarized wave incident on a slab of plasma in a parallel magnetic field is split up into two circularly polarized waves, the right-handed (or extraordinary) and the left-handed (or ordinary) waves propagating with different phase velocities (**11**).

For the right-handed wave in which the electric field vector rotates in the same sense as the electrons gyrate, the specific inductive capacity K is given, using Brown's notations, by (**6, 12**):

$$K_- = 1 - \frac{\eta}{(1-\gamma) + j\beta}, \qquad (1)^{**}$$

where

$$\eta = (\omega_p/\omega)^2, \quad \gamma = \omega_c/\omega, \quad \beta = \nu_c/\omega,$$

with

$\omega_p = \sqrt{\dfrac{e^2 N}{m\varepsilon_0}}$: plasma frequency,

e, m: charge and mass of electron,

ε_0 : permittivity of free space,

* Of course, the absorption curve comes to be very asymmetric with increasing electron density, as shown by Wharton's numerical results (**9**) and experimentally verified by Brown (**10**).

** The sign of the imaginary term is opposite to Brown's one, corresponding to the time factor $\exp(-j\omega t)$ here.

N : number density of electron,

ω : angular frequency of incident wave,

$\omega_c = \dfrac{eB}{m}$: cyclotron frequency,

ν_c : effective collision frequency of electron,

B : magnetic field strength.

On the other hand, the specific inductive capacity K is related with the refractive index n (**13**) :

$$K = K_{\mathrm{re}} + jK_{\mathrm{im}} = n^2 = (n' + jn'')^2 , \tag{2}$$

where n' : ordinary refractive index,

n'' : extinction coefficient.

Therefore,

$$\left.\begin{aligned} n' &= \left\{\frac{1}{2}(|K| + K_{\mathrm{re}})\right\}^{1/2}, \\ \text{and} \qquad n'' &= \left\{\frac{1}{2}(|K| - K_{\mathrm{re}})\right\}^{1/2}. \end{aligned}\right\} \tag{3}$$

Substituting (1) into (3), the curves representing the dispersion $(n'-1)$ and the absorption (n'') can be plotted against γ, taking η and β as parameters. A few curves were given by Wharton (**9**), but it is actually rather troublesome to calculate these curves for each pair of η and β. Moreover, in our experimental cases, the following conditions are fulfilled :

$$\eta \ll 1, \quad \beta^2 \ll 1 ,$$

corresponding to the gaseous discharge plasmas at low pressure. In such cases, the expressions (3) become approximately :

$$n'_- = 1 - \frac{\eta}{2}\frac{1-\gamma}{(1-\gamma)^2+\beta^2} - \frac{\eta^2}{8}\frac{(1-\gamma)^2-\beta^2}{\{(1-\gamma)^2+\beta^2\}^2}, \tag{4}$$

and

$$n''_- = \frac{1}{2}\frac{\eta\beta}{(1-\gamma)^2+\beta^2}\left\{1 + \frac{\eta}{2}\frac{1-\gamma}{(1-\gamma)^2+\beta^2}\right\}. \tag{5}$$

Hence, the relative phase shift $\Delta\theta$ and the attenuation α per one free space wavelength (λ_0) are :

$$\Delta\theta_- = \pi\eta\frac{1-\gamma}{(1-\gamma)^2+\beta^2} + \frac{\pi\eta^2}{4}\frac{(1-\gamma)^2-\beta^2}{\{(1-\gamma)^2+\beta^2\}^2} \quad \text{(radian/wavelength)}, \tag{6}$$

and

$$\alpha = \frac{\pi\eta}{\beta}\frac{\beta^2}{(1-\gamma)^2+\beta^2}\left\{1 + \frac{\eta}{2}\frac{1-\gamma}{(1-\gamma)^2+\beta^2}\right\} \quad \text{(neper/wavelength)}. \tag{7}$$

If the second term in the bracket { } of (7) can be neglected, the attenuation α_- is approximated by:

$$\alpha_- = \alpha_m \frac{\beta^2}{(1-\gamma)^2+\beta^2} \quad \text{(neper/wavelength)}, \tag{8}$$

where

$$\alpha_m = \pi\eta/\beta . \tag{9}$$

In the above approximation, it follows from (8) that the cyclotron resonance occurs at $\gamma=1$, i.e. $\omega=\omega_c$ and the maximum attenuation at resonance is $\alpha_m(\text{nep}/\lambda_0)$. The absorption curve ($\alpha_-$) plotted against γ is symmetrical with respect to the line $\gamma=1$, and the half-width ($\Delta\gamma$) is determined by:

$$\Delta\gamma/2 = \beta . \tag{10}$$

If B_0 is the magnetic field intensity at which cyclotron resonance occurs and the half-width expressed in magnetic field intensity is ΔB, (10) is transformed into:

$$\Delta B/B_0 = 2\beta = 2\nu_c/\omega . \tag{11}$$

It is to be noted that the above approximation in which (8) has been derived is equivalent to $n' \simeq 1$ and thus the absorption curve given by (8) is equivalent to the one given by the real conductivity:

$$\sigma_R = \sigma_0 \frac{\beta^2}{(1-\gamma)^2+\beta^2}, \tag{12}$$

where $\sigma_0 = e^2N/m\nu_c$ is static conductivity (see appendix).

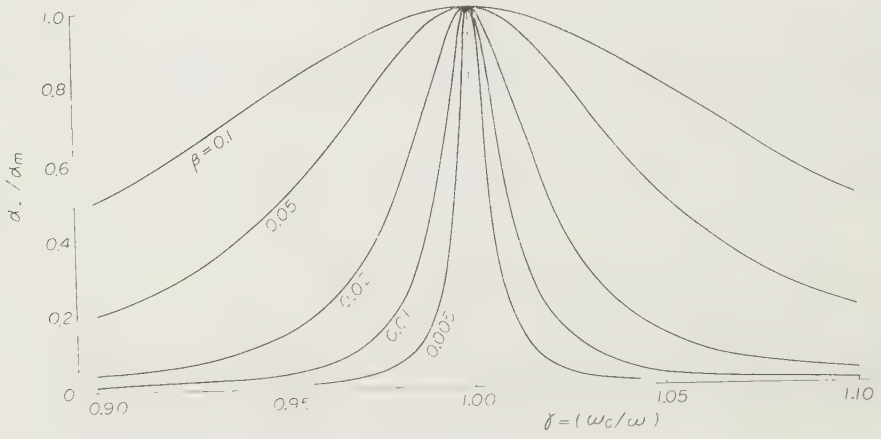

Fig. 1. Absorption curves.

The absorption curves (α_-/α_m) expressed by (8) are plotted against γ, taking β as parameter, in Fig. 1. For comparison, the absorption curves calculated from

(7) and the approximate form (8) are plotted in Fig. 2. In addition, we plot $(n'_{\perp}-1)$ against γ in Fig. 3, where $n'_{\perp}$ is approximated by:

$$n'_{\perp} \simeq 1-\frac{\eta}{2}\frac{1-\gamma}{(1-\gamma)^2+\beta^2}. \tag{4a}$$

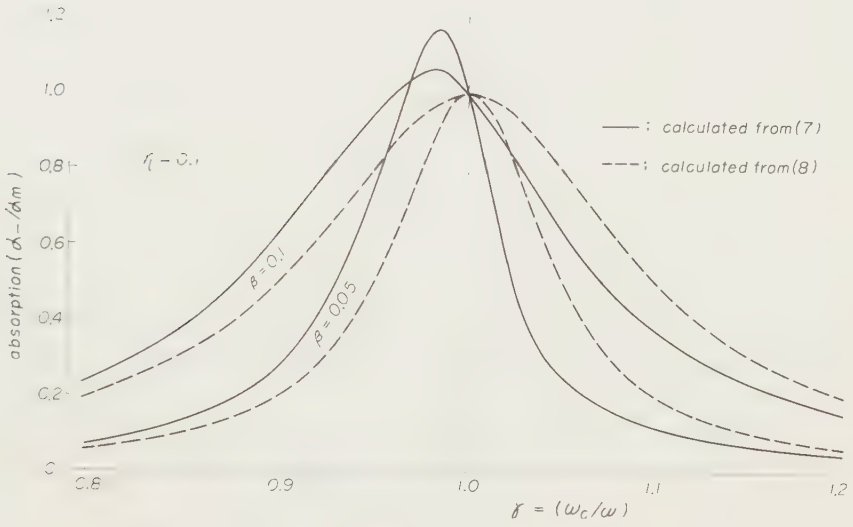

Fig. 2. Comparison between absorption curves calculated by (7) and (8).

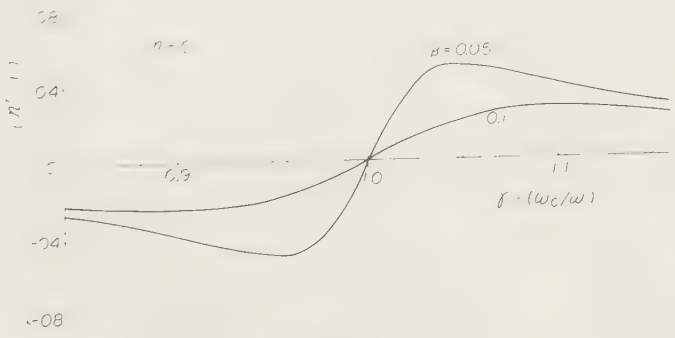

Fig. 3. Dispersion curves.

The maximum absorption α_m is proportional to η and inversely proportional to β. This is natural, since the power absorbed by plasma increases with increasing electron density (η) and with decreasing collision frequency (β). On the contrary, if the collision frequency is so high that the electrons collide before they finish respective orbits of gyrations (i.e. $\nu_c/\omega=\beta>1$), then no cyclotron resonance occurs. In Figs. 4 and 5 the maximum absorption (α_m) is plotted against η and β respectively.

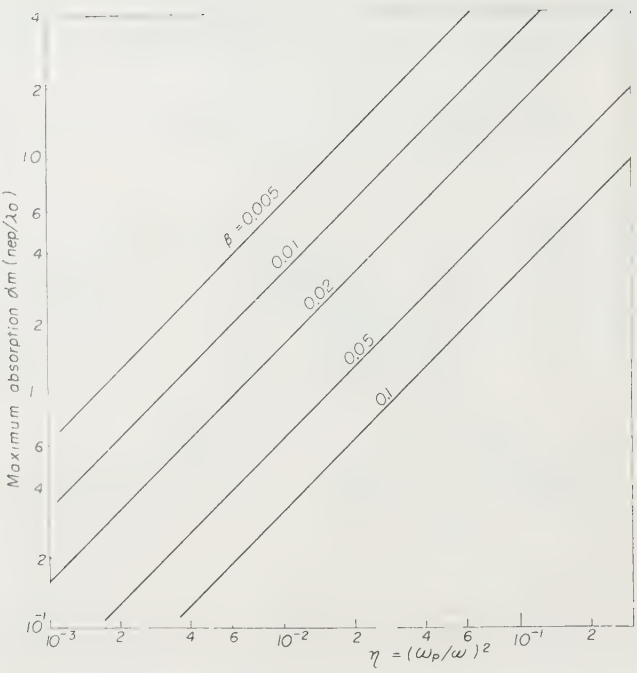

Fig. 4. α_m *versus* η.

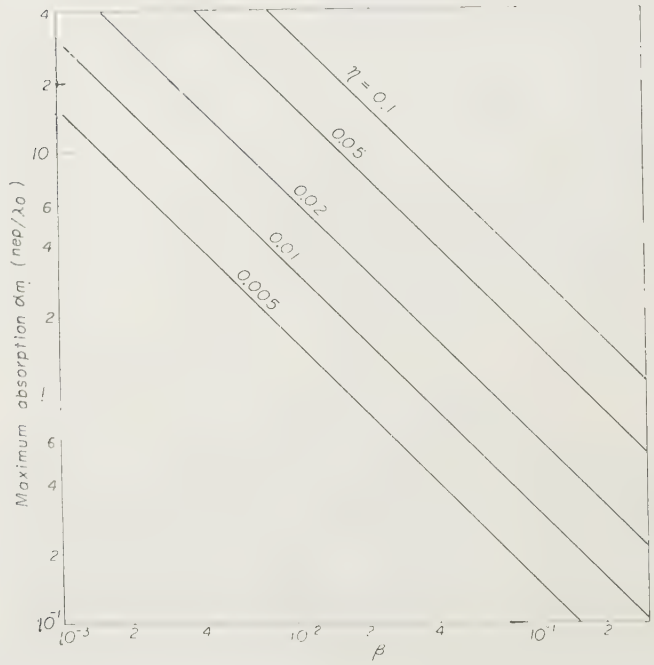

Fig. 5. α_m *versus* β.

3. Dispersion of the left-handed circularly polarized wave

We can obtain an approximate dispersion relation for the left-handed wave in the similar way to the right-handed one.

The specific inductive capacity K_+ for this wave is given by:

$$K_+ = 1 - \frac{\eta}{(1+\gamma)+j\beta}, \tag{13}$$

and thus n'_+ and n''_+ are given by:

$$n'_+ = 1 - \frac{\eta}{2}\frac{1+\gamma}{(1+\gamma)^2+\beta^2} - \frac{\eta^2}{8}\frac{(1+\gamma)^2-\beta^2}{\{(1+\gamma)^2+\beta^2\}^2}, \tag{14}$$

and

$$n''_+ = \frac{1}{2}\frac{\eta\beta}{(1+\gamma)^2+\beta^2}\left\{1+\frac{\eta}{2}\frac{1+\gamma}{(1+\gamma)^2+\beta^2}\right\}. \tag{15}$$

Hence, the relative phase shift $\Delta\theta_+$ and the absorption α_+ of the left-handed wave per one free space wavelength (λ_0) are respectively:

$$\Delta\theta_+ = \pi\eta\frac{1+\gamma}{(1+\gamma)^2+\beta^2} + \frac{\pi\eta^2}{4}\frac{(1+\gamma)^2-\beta^2}{\{(1+\gamma)^2+\beta^2\}^2} \quad \text{(radian/wavelength)}, \tag{16}$$

and

$$\alpha_+ = \alpha_m\frac{\beta^2}{(1+\gamma)^2+\beta^2} \quad \text{(neper/wavelength)}. \tag{17}$$

For the left-handed wave, naturally no resonance phenomena occur, since the electric vector rotates in the opposite sense to the electron gyration.

4. Dispersion of the transversal wave ($k_0 /\!/ B$)

A transversal wave incident on a slab of plasma in a parallel magnetic field is considered. In passing through the plasma, the plane of polarization is rotated by an angle $\Delta\theta_{//}$ per one free space:

$$\Delta\theta_{//} = \pi\eta\left\{\frac{1-\gamma}{(1-\gamma)^2+\beta^2} - \frac{1+\gamma}{(1+\gamma)^2+\beta^2}\right\} \quad \text{(radian/wavelength)}, \tag{18}$$

analogously to the Faraday effect in crystal.

It is evident from the discussions in §§ 2 and 3, that the resonance absorption for the case $\eta \ll 1$ and $\beta^2 \ll 1$ can be approximated by:

$$\alpha_{//} = \frac{\alpha_m}{2}\left[\frac{\beta^2}{(1-\gamma)^2+\beta^2}\left\{1+\frac{\eta}{2}\frac{1-\gamma}{(1-\gamma)^2+\beta^2}\right\} + \frac{\beta^2}{(1+\gamma)^2+\beta^2}\right] \quad \text{(neper/wavelength)}. \tag{19}$$

Moreover, in the extreme approximation, the above equation becomes:

$$\alpha_{//} = \frac{\alpha_m}{2}\left\{\frac{\beta^2}{(1-\gamma)^2+\beta^2} + \frac{\beta^2}{(1+\gamma)^2+\beta^2}\right\} \quad \text{(neper/wavelength)}. \tag{20}$$

This expression agrees with that calculated by Brown *et al.* (5) from the conductivity. Under ordinary experimental conditions of the electron cyclotron resonance, $\beta^2 \ll 1$. Then, as the antiresonance term in (20) is almost constant and negligibly small compared with the resonance term, in the neighbourhood of the resonance, the absorption curve for the transversal wave actually coincides with that for the right-handed one.

Next, we consider the absorption curve including both resonance and antiresonance terms. Since $\beta^2 \ll 1$ and it is considered in the vicinity of the resonance, (20) can be approximated by:

$$\alpha_{//} = \frac{\alpha_m}{2} \frac{(2\beta)^2}{(\gamma_0^2 - \gamma^2)^2 + (2\beta)^2}, \tag{21}$$

where

$$\gamma_0^2 = 1 - \beta^2. \tag{22}$$

Therfore, in the above approximation the cyclotron resonance occurs at $\gamma_0 = (1-\beta^2)^{1/2} \simeq 1 - \beta^2/2$, and the maximum attenuation is $\alpha_m/2$. The absorption $(\alpha_{//})$ plotted against γ^2 is indeed symmetrical, but when plotted against γ it is not symmetical. The half-width of the absorption curve $(\Delta\gamma)$ is:

$$\Delta\gamma = (\Delta\gamma_-/2) + (\Delta\gamma_+/2) \simeq 2\beta, \tag{23}$$

and the measure of asymmetry is given by:

$$(\Delta\gamma_-/2) - (\Delta\gamma_+/2) \simeq \beta^2, \tag{24}$$

(see Fig. 6).

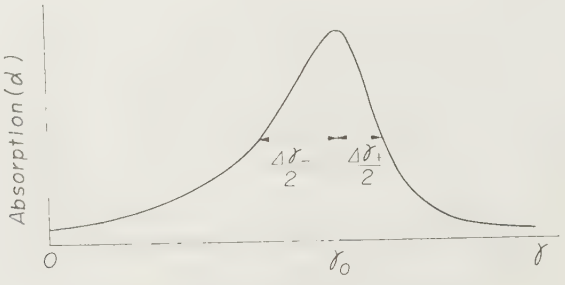

Fig. 6. Asymmetrical absorption curve.

Integrating $\alpha_{//}$ expressed by (20) with respect to γ, we obtain:

$$\int_0^\infty \alpha_{//} d\gamma = \frac{\pi^2}{2}\eta = \frac{\pi^2}{2}\frac{e^2}{m\varepsilon_0\omega^2}N, \tag{25}$$

which implies that the area surrounded by the absorption curve and the γ axis is determined only by the electron density, being independent of the collision frequency.

5. Conclusion

Using the specific inductive capacity, the expressions for the absorption and the relative phase shift at the cyclotron resonance in a slightly ionized gas were derived for the transversal wave ($\boldsymbol{k}_0 \perp \boldsymbol{B}$). The resulting absorption curve, which strictly represents the attenuation factor, is somewhat complicated in comparison with that which represents the real conductivity σ_R, because the extinction coefficient n'' is more complicated than σ_R. As shown, in the extreme approximation, both absorption curves are coincident with each other.

In our present slightly ionized gas in which $\eta \ll 1$ and $\beta^2 \ll 1$, the expression (8) for the right-handed and the expression (20) for the transversal wave are appropriately used for the analyses of the experimental results. If this approximation is not permissible, we must use (4) or (3) which is rather complicated. Wharton calculated n' and n'' from (3) using tentative numerical values and it was shown that the absorption curve becomes more asymmetrical with increasing η (**9**), and experimentally verified by Brown (**10**).

The microwave propagating transversely to the magnetic field will be discussed in the next part.

Acknowledgments

The author wishes to express his sincere thanks to Prof. I. Takahashi for his guidance throughout this work. The author's thanks are also due to Prof. K. Mitani for discussions.

Appendix

The complex conductivity $\sigma_c = \sigma_R - j\sigma_i$ is related with the specific inductive capacity by:

$$K = 1 + j\frac{\sigma_c}{\omega\varepsilon_0} = \left(1 - \frac{\sigma_i}{\omega\varepsilon_0}\right) + j\frac{\sigma_R}{\omega\varepsilon_0}. \tag{26}$$

From this and (3) we have

$$n'^2 = \frac{1}{2}\left\{\sqrt{\left(1 - \frac{\sigma_i}{\omega\varepsilon_0}\right)^2 + \left(\frac{\sigma_R}{\omega\varepsilon_0}\right)^2} + \left(1 - \frac{\sigma_i}{\omega\varepsilon_0}\right)\right\}, \tag{27}$$

and

$$n''^2 = \frac{1}{2}\left\{\sqrt{\left(1 - \frac{\sigma_i}{\omega\varepsilon_0}\right)^2 + \left(\frac{\sigma_R}{\omega\varepsilon_0}\right)^2} - \left(1 - \frac{\sigma_i}{\omega\varepsilon_0}\right)\right\}. \tag{28}$$

If

$$\frac{\sigma_i}{\omega\varepsilon_0} < 1, \quad \frac{\sigma_R}{\omega\varepsilon_0} \ll 1,$$

(27) and (28) can be approximated by:

$$n' = 1 - \frac{1}{2}\frac{\sigma_i}{\omega\varepsilon_0} - \frac{1}{8}\left\{\left(\frac{\sigma_i}{\omega\varepsilon_0}\right)^2 - \left(\frac{\sigma_R}{\omega\varepsilon_0}\right)^2\right\}, \tag{29}$$

and

$$n'' = \frac{1}{2}\frac{\sigma_R}{\omega\varepsilon_0}\left\{1 + \frac{1}{2}\frac{\sigma_i}{\omega\varepsilon_0}\right\}. \tag{30}$$

On the other hand, equating the imaginary part of (26) to that of (2), we have

$$n'' = \frac{1}{2}\frac{\sigma_R}{\omega\varepsilon_0}\frac{1}{n'}. \tag{31}$$

Accordingly,

(i) if $n' \simeq 1$,

$$n'' \simeq \frac{1}{2}\frac{\sigma_R}{\omega\varepsilon_0}, \tag{32}$$

which implies that the variation of n'' *versus* γ is equivalent to that of σ_R; and

(ii) if $n'^2 \simeq 1 - \sigma_i/(\omega\varepsilon_0)$,

$$n'' \simeq \frac{1}{2}\frac{\sigma_R}{\omega\varepsilon_0}\left(1 - \frac{\sigma_i}{\omega\varepsilon_0}\right)^{-1/2} \simeq \frac{1}{2}\frac{\sigma_R}{\omega\varepsilon_0}\left(1 + \frac{1}{2}\frac{\sigma_i}{\omega\varepsilon_0}\right), \tag{33}$$

which agrees with (30).

REFERENCES

1. J. Schneider, F. W. Hofmann: Phys. Rev. **116** (1959), 244.
2. J. L. Hirshfield, S. C. Brown: J. Appl. Phys. **29** (1958), 1749.
3. B. C. Hwa: Phys. Rev. **110** (1958), 307.
4. D. C. Kelly: Phys. Rev. **119** (1960), 27.
5. D. C. Kelly, H. Margenau, and S. C. Brown: Phys. Rev. **108** (1957), 1367.
6. S. C. Brown: Proc. 2nd International Conf. on the Peaceful Uses of Atomic Energy, Geneva (1958) No. P/387.
7. L. Goldstein: *Advances in Electronics and Electron Physics* (Academic Press, Inc., 1955) Vol. **7**, p. 399.
8. J. E. Drummond: Phys. Rev. **110** (1958), 293; **112** (1958), 1460.
9. C. B. Wharton: UCRL-4836 (Rev.) (1957).
10. S. C. Brown: *Proc. of the 4th International Conf. on Ionized Phenomena in Gases*, Uppsala, (Aug., 1959) III C 691.
11. for example, J. G. Linhart: *Plasma Physics* (North Holland Publ. CO., 1960), p. 106.
12. S. K. Mitra: *The Upper Atmosphere* (the Asiatic Society, Calcutta 1952).
13. J. A. Stratton: *Electromagnetic Theory* (McGraw-Hill Co., 1941), p. 321.

Memoirs of the College of Science, University of Kyoto, Series A,
Vol. XXIX, No. 3, Article 8, 1961.

ABSORPTION AT ELECTRON CYCLOTRON RESONANCE IN SLIGHTLY IONIZED GASES (II)*

BY

Shigetoshi TANAKA

(*Received March 17, 1961*)

ABSTRACT

An expression of the absorption at cyclotron resonance was derived for the microwave propagating through a slightly ionized gas, transversally to the static magnetic field. It was shown that the resonance occurs at $\omega_c = \sqrt{\omega^2 - \omega_p^2 - \nu_c^2}$ instead of $\omega_c = \omega$ and the absorption curve is not Lorentzian and the half-width depends not only on collision frequency but also on electron density. Therefore, one can obtain both the electron density and the collision frequency from one measured resonance absorption curve. The same expression was derived by solving the Boltzmann transport equation for the distribution of electrons under the same circumstances.

1. Introduction

In the first part** dealing with the microwave propagating along the static magnetic field ($\boldsymbol{k}_0 /\!/ \boldsymbol{B}$), it was shown that the cyclotron resonance occurs at $\omega = \omega_c$, the absorption curve is Lorentzian and the half-width gives a direct measure of the collision frequency.

In this part, we consider the electron cyclotron resonance in a slightly ionized gas, for the microwave propagating tansversally to $\boldsymbol{B}$ ($\boldsymbol{k}_0 \perp \boldsymbol{B}$). Since the wave becomes a so-called hybrid wave with transversal and longitudinal electric vectors in the case of $\boldsymbol{k}_0 \perp \boldsymbol{B}$, the dispersion relation is more complicated in comparison with the purely transversal wave ($\boldsymbol{k}_0 /\!/ \boldsymbol{B}$) (1).

In a similar way to the case of purely transversal wave, approximate expressions for the attenuation factor and the relative phase shift near the cyclotron resonance were derived from the specific inductive capacity for the hybrid wave. The same absorption expression was obtained by solving the Boltzmann transport equation for the distribution function of electrons and it was shown that there is no power dissipation for the longitudinal electrical component of the hybrid wave.

* Reported in Japanese in "Kakuyugo Kenkyu (Nuclear Fusion Research)" **4** (June, 1960), 550.
** The preceding paper, hereafter referred to as I.

2. Dispersion of the hybrid wave

We consider a microwave propagating through a slightly ionized gas in the direction of $\boldsymbol{k}_0$ transversal to the static magnetic field $\boldsymbol{B}$.

The electron motion parallel to $\boldsymbol{B}$ is unaffected by $\boldsymbol{B}$, so the wave with the electric vector initially parallel to $\boldsymbol{B}$ can remain as purely transversal wave, and the dispersion relation is the same as in the case of no magnetic field. Such a case is left out of consideration. The interesting case to be considered is that in which $\boldsymbol{E}$ is initially perpendicular to $\boldsymbol{B}$. Taking the z-axis parallel to $\boldsymbol{B}$ and the x axis to $\boldsymbol{k}_0$, the wave, incident with E_y component only on the plasma slab, comes to have both E_x and E_y components inside the plasma. Such a wave is so-called hybrid transversal and longitudinal wave (**1, 2**).

For the hybrid wave, the effective specific inductive capacity $K_\perp$ is given by (**3, 4**):

$$K_\perp = 1 - \frac{\eta(1-\eta+j\beta)}{(1-\eta-\gamma^2-\beta^2)+j\beta(2-\eta)}, \tag{1}$$

using the notations given in I. We proceed in a similar way.

If $\eta \ll 1$ and $\beta^2 \ll 1$, by expanding (1) with respect to η, the refractive index $(n_\perp = n'_\perp + jn''_\perp)$ can be approximated by:

$$n'_\perp = 1 - \frac{\eta}{2}\frac{(1-\eta)(1-\eta-\gamma^2)+\beta^2}{(1-\eta-\gamma^2-\beta^2)^2+\beta^2(2-\eta)^2} - \frac{\eta^2}{8}\frac{\{(1-\eta)(1-\eta-\gamma^2)+\beta^2\}^2-\beta^2\{(1-\eta)^2+\gamma^2+\beta^2\}^2}{\{(1-\eta-\gamma^2-\beta^2)^2+\beta^2(2-\eta)^2\}^2}, \tag{2}$$

and

$$n''_\perp = \frac{\beta\eta}{2}\frac{(1-\eta)^2+\gamma^2+\beta^2}{(1-\eta-\gamma^2-\beta^2)^2+\beta^2(2-\eta)^2} \times\left[1+\frac{\eta}{2}\frac{(1-\eta)(1-\eta-\gamma^2)+\beta^2}{(1-\eta-\gamma^2-\beta^2)^2+\beta^2(2-\eta)^2}\right]. \tag{3}$$

If the last terms in (2) and (3) can be neglected, the relative phase shift $\Delta\theta_\perp$ and the attenuation $\alpha_\perp$ per one free space wavelength λ_0 are:

$$\Delta\theta_\perp = \pi\eta\frac{(1-\eta)(1-\eta-\gamma^2)+\beta^2}{(1-\eta-\gamma^2-\beta^2)^2+\beta^2(2-\eta)^2}\,(\mathrm{rad}/\lambda_0), \tag{4}$$

and

$$\alpha_\perp = \pi\eta\beta\frac{(1-\eta)^2+\gamma^2+\beta^2}{(1-\eta-\gamma^2-\beta^2)^2+\beta^2(2-\eta)^2}\,(\mathrm{nep}/\lambda_0). \tag{5}$$

3. Resonance position and maximum absorption

The cyclotron resonance occurs near the value at which the first term of the denominator of (5) is equal to zero. In the neighbourhood of resonance, $\alpha_\perp$ becomes approximately:

$$\alpha_{\perp} = \alpha_{\perp m} \frac{\beta^2(2-\eta)^2}{(\gamma^2-\gamma_0^2)^2 + \beta^2(2-\eta)^2}, \tag{6}$$

where

$$\alpha_{\perp m} = \frac{1-\eta}{2-\eta}\frac{\pi\eta}{\beta}, \tag{7}$$

and

$$\gamma_0^2 = 1-\eta-\beta^2, \tag{8}$$

or

$$\omega_c^2 = \omega^2 - \omega_p^2 - \nu_c^2. \tag{8a}$$

Thus, from (6) in the above approximation, the cyclotron resonance occurs at $\gamma=\gamma_0$ which is on the low magnetic field side where $\gamma_0=\omega_c/\omega$ is smaller than unity and the maximum attenuation is $\alpha_{\perp m}(\mathrm{nep}/\lambda_0)$. This is characteristic of the hybrid wave.

Next, we investigate to what extent the approximation of (6) is permissible. The exact resonance position (γ_R) of (5) can be determined by $\partial\alpha_{\perp}/\partial\gamma=0$, from which follows:

$$\gamma_R^2 = (1-\eta)\left\{1+\frac{\eta}{2}\left(\frac{\beta}{1-\eta}\right)^2\right\}+O(\beta^4), \tag{9}$$

where $O(\beta^4)$ is of the order of magnitude of β^4. Therefore,

$$\gamma_R^2-\gamma_0^2 = \frac{\beta^2}{2}\frac{2-\eta}{1-\eta}+O(\beta^4) > 0, \tag{10}$$

which implies that we can regard the position of cyclotron resonance as γ_0, corresponding to the neglect of β^2 against unity.

Substituting (9) into (5), we can obtain the following expression for the exact attenuation at cyclotron resonance ($\alpha_{\perp R}$):

$$\frac{\alpha_{\perp R}}{\alpha_{\perp m}} = 1+\frac{1}{4}\left(\frac{\beta}{1-\eta}\right)^2 + O(\beta^4) > 1, \tag{11}$$

from which we can regard the maximum attenuation as $\alpha_{\perp m}$, in accordance with the neglect of β^2 against unity.

In Fig. 1, γ_0^2 is plotted against η. In Figs. 2 and 3 $\alpha_{\perp m}$ is plotted against η and β respectively.

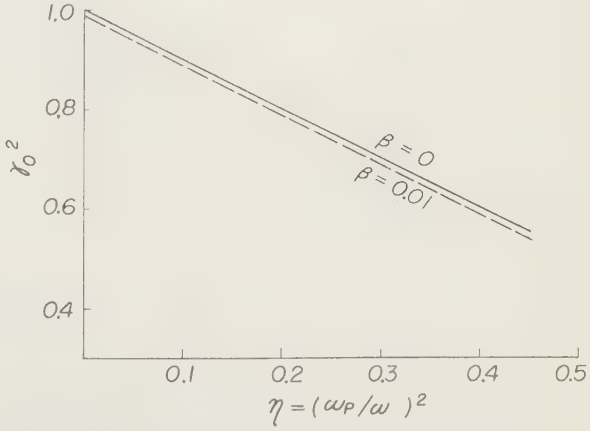

Fig. 1. Resonance position (γ_0^2) *versus* η.

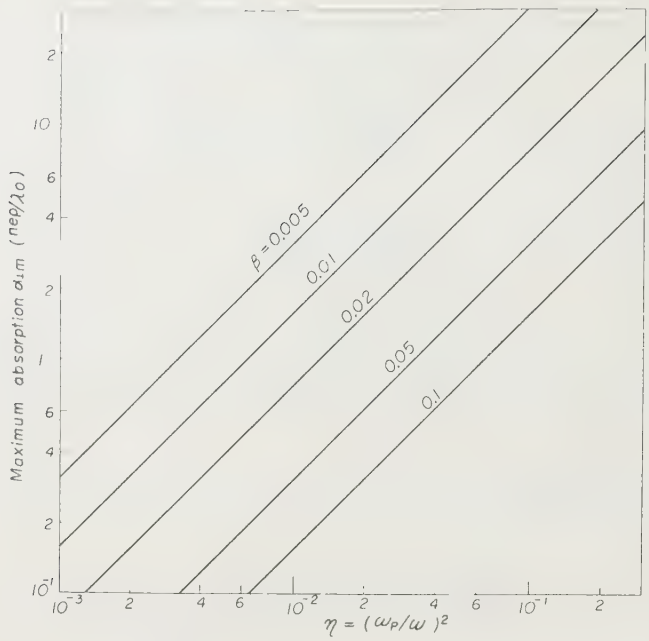

Fig. 2. $\alpha_{\perp m}$ *versus* η.

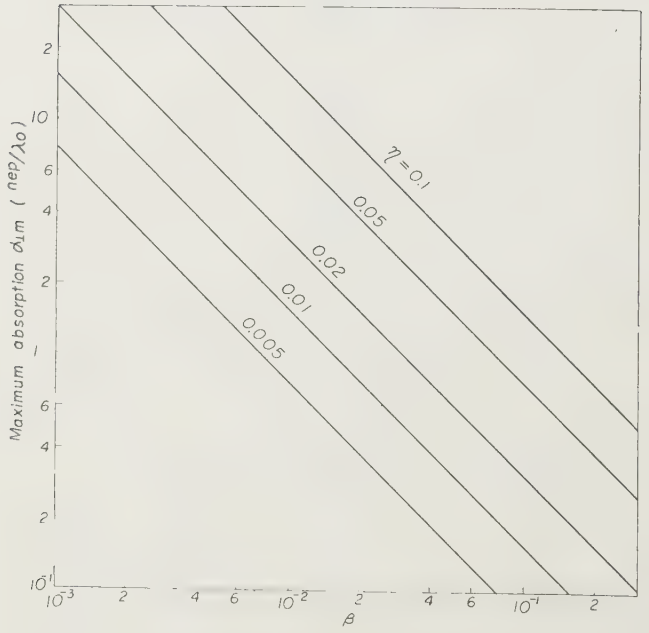

Fig. 3. $\alpha_{\perp m}$ *versus* β.

4. Absorption curve and half-width

It will be seen from (6) that, although the absorption curve plotted against γ^2 is symmetrical with respect to the line $\gamma^2=\gamma_0^2$, the curve plotted against γ is not symmetrical and somewhat steeper on the side of $\gamma>\gamma_0$.

From (6), the half-width ($\Delta\gamma$) of the absorption curve against γ is:

$$\Delta\gamma = \beta\frac{2-\eta}{(1-\eta)^{1/2}}+O(\beta^3)\,, \tag{12}$$

and the measure of asymmetry is given by:

$$\frac{\Delta\gamma_-}{2}-\frac{\Delta\gamma_+}{2} = \frac{\beta^2}{4}\frac{(2-\eta)^2}{(1-\eta)^{3/2}}\,, \tag{13}$$

which implies that the curve is more asymmetric with increasing β. If B_0 and ΔB denote the magnetic field intensity at which cyclotron resonance occurs and the half-width respectively,

$$\frac{\Delta B}{B_0} = \frac{\Delta\gamma}{\gamma_0} = \beta\frac{2-\eta}{1-\eta}+O(\beta^2) \simeq \frac{\nu_c}{\omega}\frac{2-\eta}{1-\eta}\,, \tag{14}$$

which is useful for determining ν_c from the experimental data, since we can determine B_0 and ΔB by experiments.

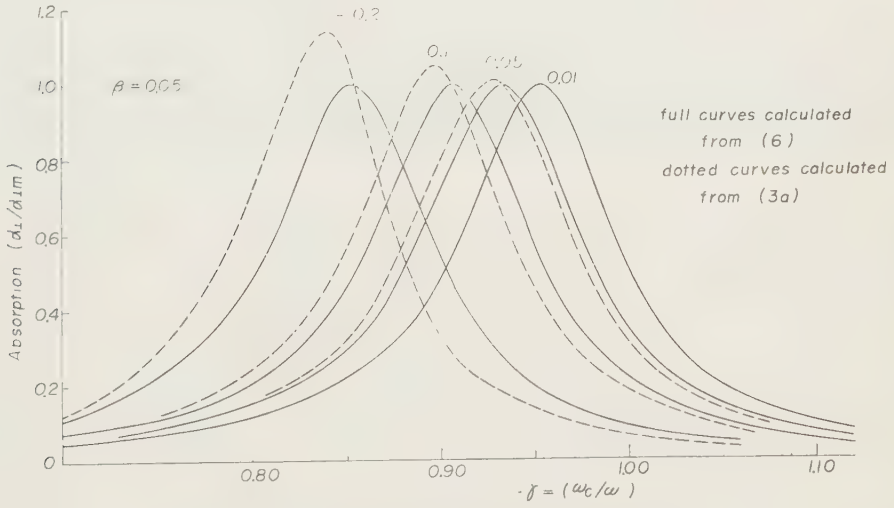

Fig. 4. Absorption curves *versus* γ for various η.

In Figs. 4 and 5 several absorption curves ($\alpha_\perp/\alpha_{\perp m}$) are plotted against γ. In these figures, full curves are calculated by (6), and dotted curves by the following expression, which is derived from (3) and (6):

$$\frac{\alpha_{\perp}}{\alpha_{\perp m}} = \frac{\beta^2(2-\eta)^2}{(\gamma_0^2-\gamma^2)^2+\beta^2(2-\eta)^2}(2-n'_{\perp}), \tag{3a}$$

with $n'_{\perp}$ approximated from (2) by:

$$n'_{\perp} \simeq 1-\frac{\eta}{2}\frac{(1-\eta)(1-\eta-\gamma^2)+\beta^2}{(\gamma_0^2-\gamma^2)^2+\beta^2(2-\eta)^2}. \tag{2a}$$

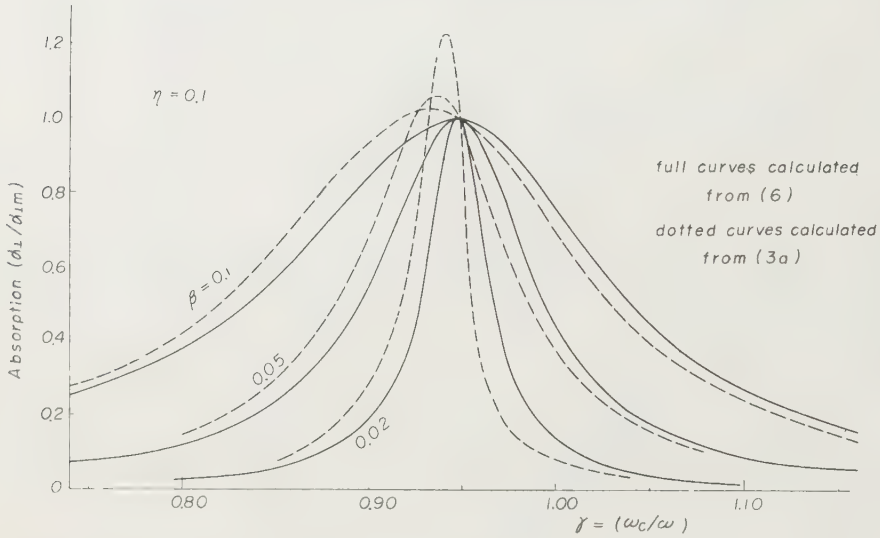

Fig. 5. Absorption curves *versus* γ for various β.

It is to be noted that the dotted curves are more exact than the full curves and that the resonance positions of the former are on the slightly smaller side of γ and the maximum absorptions are slightly larger than those of the latter.

In Fig. 6, $(n'_{\perp}-1)$ calculated by (2a) is plotted against γ.

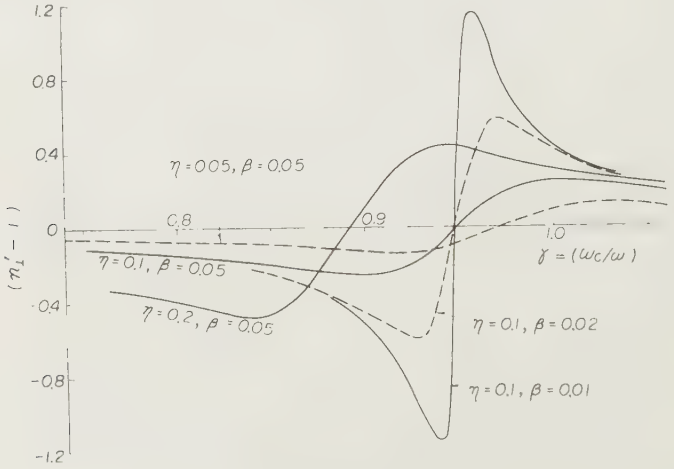

Fig. 6. Dispersion curves *versus* γ.

5. Comparison of cyclotron resonances between various waves

The behaviours of cyclotron resonances are quite different according to the wave types. The characteristics are tabulated in the following table:

Table. Characteristics of cyclotron resonance.

	Right-handed wave	Transversal wave ($\boldsymbol{k}_0 /\!/ \boldsymbol{B}$)	Hybrid wave ($\boldsymbol{k}_0 \perp \boldsymbol{B}$)
Resonance position	$\gamma=1$ independent of N_e, ν_c	$\gamma_0^2=1-\beta^2$ independent of N_e	$\gamma_0^2=1-\eta-\beta^2$ dependent on N_e, ν_c
Maximum attenuation	$\frac{\pi\eta}{\beta}$	$\frac{1}{2}\frac{\pi\eta}{\beta}$	$\frac{1-\eta}{2-\eta}\frac{\pi\eta}{\beta}$
Half-width	2β	2β	$(2-\eta)\beta$
Absorption curve	symmetrical	Lorentzian	non-Lorentzian
Approximate expression	(8) in I	(20) in I	(6) in the present part

6. Derivation by Boltzmann equation

We can derive the same expression for the absorption curve at cyclotron resonance by solving the Boltzmann equation.

Desloge, Matthysse and Margenau (**5**) have shown that if one assumes that the effect of high frequency electric field upon an electron in a slightly ionized gas is on the average an addition, in the direction of the field, of a velocity component, the magnitude of which is dependent on the electron velocity, then it is possible to derive very simply the expression for conductivity. Expanding their method in the presence of the magnetic field, Dodo (**6**) has obtained a tensor specific inductive capacity which is coincident with that derived about uniform distribution of electrons.

Following these methods, we derive the cyclotron resonance absorption curve. The Boltzmann transport equation for a plasma in a high frequency electric field $\boldsymbol{E}$ $\boldsymbol{E}_0 \exp(-j\omega t)$ and a static magnetic field $\boldsymbol{B}$ may be written, using well-known notations:

$$\frac{\partial f}{\partial t}+\boldsymbol{F}\nabla_v f=\frac{D_c f}{Dt}, \tag{15}$$

where

$$\boldsymbol{F}=\frac{e\boldsymbol{E}}{m}+\frac{e}{m}(\boldsymbol{v}\times\boldsymbol{B}), \tag{16}$$

$$\frac{D_c f}{Dt}=\int f(\boldsymbol{v}', t)W(\boldsymbol{v}', \boldsymbol{v})d\boldsymbol{v}'-f(\boldsymbol{v}, t)\int W(\boldsymbol{v}, \boldsymbol{v}')d\boldsymbol{v}', \tag{17}$$

$$W(\boldsymbol{v}', \boldsymbol{v}) = W(\boldsymbol{v}', -\boldsymbol{v}) \tag{18}$$

and

$$\int W(\boldsymbol{v}, \boldsymbol{v}')d\boldsymbol{v}' = \nu(\boldsymbol{v}).$$

Next, if we assume that all of the electrons which are in a given velocity range in the equilibrium distribution are shifted by the Lorentz force to a new range in which the velocity differs from the original velocity by an amount $\boldsymbol{g}$,

$$f(\boldsymbol{v}, t) = f_0(\boldsymbol{v}-\boldsymbol{g})\left(1-\frac{\partial g_x}{\partial v_x}\right)\left(1-\frac{\partial g_y}{\partial v_y}\right)\left(1-\frac{\partial g_z}{\partial v_z}\right), \tag{19}$$

where $f_0(\boldsymbol{v})$ is the equilibrium distribution function and $g_i = g_i(\boldsymbol{v}, t)$ $(i = x, y, z)$. If $f(\boldsymbol{v}, t)$ of (19) is expanded in powers of g_i and one assumes rapid convergence of the resulting series,

$$f(\boldsymbol{v}, t) = f_0 - \boldsymbol{v}\cdot\boldsymbol{G}, \tag{20}$$

where

$$\boldsymbol{G} = \frac{1}{v}\frac{\partial}{\partial v}(f_0\boldsymbol{g}), \tag{21}$$

which is even with respect to $\boldsymbol{v}$, assuming $\boldsymbol{g} = \boldsymbol{g}(v, t)$.

Substituting (20) and (16) into (15), we obtain:

$$\begin{aligned}\boldsymbol{v}\left\{\frac{\partial \boldsymbol{G}}{\partial t} - \frac{e\boldsymbol{E}}{m}\frac{1}{v}\frac{\partial f_0}{\partial v} - \frac{e}{m}(\boldsymbol{G}\times\boldsymbol{B})\right\} + \frac{e\boldsymbol{E}}{m}\left(\boldsymbol{G} + v\frac{\partial \boldsymbol{G}}{\partial v}\right) \\ = \nu f(\boldsymbol{v}, t) - \int f(\boldsymbol{v}', t)\, W(\boldsymbol{v}', \boldsymbol{v})\, d\boldsymbol{v}'.\end{aligned} \tag{22}$$

Replacing $\boldsymbol{v}$ by $-\boldsymbol{v}$ in (22) and subtracting the resulting equation from (22), one finds

$$\frac{\partial \boldsymbol{G}}{\partial t} = \frac{e\boldsymbol{E}}{m}\frac{1}{v}\frac{\partial f_0}{\partial v} + \frac{e}{m}(\boldsymbol{G}\times\boldsymbol{B}) - \nu\boldsymbol{G}, \tag{23}$$

which is coincident with Eq. (14) in Kelly-Margenau-Brown's paper (7), in which $f(\boldsymbol{v}, t)$ is expanded in spherical harmonics and $\boldsymbol{b}$ is used such as:

$$\boldsymbol{b} = -v\boldsymbol{G}. \tag{24}$$

If $\boldsymbol{G}$ is obtained by (23), the current density $\boldsymbol{J}$ is given by:

$$\boldsymbol{J} = Ne\int \boldsymbol{v} f(\boldsymbol{v}, t)\, d\boldsymbol{v} = -Ne\int \boldsymbol{v}(\boldsymbol{v}\cdot\boldsymbol{G})\, d\boldsymbol{v} \tag{25}$$

and the average power $(\bar{P})$ absorbed by electrons per unit volume is

$$\bar{P} = \frac{1}{2}\,\mathrm{Re}\,(\boldsymbol{J}\cdot\boldsymbol{E}^*). \tag{26}$$

Now we calculate for the two interesting cases.

(i) Transversal wave

Since the wave is purely transversal, in the above-mentioned coordinates $\boldsymbol{J}$ exists only in the xy plane. In quite the same way as Brown *et al.* we obtain for the constant mean free time:

$$P = \frac{E_0^2 \varepsilon_0 \omega \eta}{4\beta}\left\{\frac{\beta^2}{(1-\gamma)^2+\beta^2}+\frac{\beta^2}{(1+\gamma)^2+\beta^2}\right\}, \tag{27}$$

which is identical with (22) in I.

(ii) Hybrid wave

$\boldsymbol{E}$ and $\boldsymbol{J}$ have the x- and y- components. Solving (23), we obtain:

$$\begin{pmatrix} G_x \\ G_y \end{pmatrix} = -\frac{e}{m}\frac{1}{v}\frac{\partial f_0}{\partial v}\frac{1}{(j\omega-\nu)^2+\omega_c^2}\begin{pmatrix} j\omega-\nu & \omega_c \\ -\omega_c & j\omega-\nu \end{pmatrix}\begin{pmatrix} E_x \\ E_y \end{pmatrix}. \tag{28}$$

Therefore, from (25) J_x is given by:

$$J_x = \frac{e^2 N}{3m}\int \frac{(j\omega-\nu)E_x+\omega_c E_y}{(j\omega-\nu)^2+\omega_c^2} 4\pi v^3 \frac{\partial f_0}{\partial v} dv. \tag{29}$$

Integration is easily carried out for the constant mean free time and J_x, J_y are given by:

$$\begin{pmatrix} J_x \\ J_y \end{pmatrix} = \frac{\eta\omega}{4\pi}\frac{1}{(1+j\beta)^2-\gamma^2}\begin{pmatrix} j(1+j\beta) & \gamma \\ -\gamma & j(1+j\beta) \end{pmatrix}\begin{pmatrix} E_x \\ E_y \end{pmatrix}. \tag{30}$$

On the other hand, using the specific inductive capacity tensor (K) for this configuration, the electric field vector should fulfil the following equation:

$$\nabla^2 \boldsymbol{E} - \nabla\nabla\cdot\boldsymbol{E} = \frac{1}{c^2}(K)\frac{\partial \boldsymbol{E}}{\partial t}. \tag{31}$$

Therefore, the longitudinal component E_x can be expressed by E_y as:

$$E_x = \frac{K_{xy}}{K_{xx}}E_y = -\frac{j\eta\gamma}{(1-\eta-\gamma^2-\beta^2)+j\beta(2-\eta)}E_y. \tag{32}$$

The average power absorbed from this hybrid wave $(\bar{P})$ is the sum of the powers absorbed from the longitudinal wave $(\bar{P}_x)$ and from the transversal wave $(\bar{P}_y)$. Substituting (30) and (32) into (26), we obtain:

$$\bar{P}_x = \frac{1}{2}\mathrm{Re}\,(J_x E_x^*) = 0,$$

and

$$\bar{P}_y = \frac{|E_y|^2 \omega\eta}{8\pi}\frac{\beta^2\{(1-\eta)^2+\gamma^2+\beta^2\}}{\beta\{(1-\eta-\gamma^2-\beta^2)^2+\beta^2(2-\eta)^2\}} = \bar{P}, \tag{33}$$

which is coincident with (5). It is concluded from (33) that as there is no power dissipation in the longitudinal component, the current component J_x is out-of-phase with the field E_x.

It has been shown by Watanabe (8) that the effect of the longitudinal component of our hybrid wave can be neglected, and K is expressed by (1) to a good approximation under the following condition:

$$\frac{\gamma_e \kappa T_e}{mc^2} \ll 1, \tag{34}$$

where γ_e is the ratio of specific heat at constant pressure to that at constant volume of electron gas. The above condition is fully permissible in the cold plasma.

If we express the ratio of the longitudinal field component to the transversal one as:

$$E_x/E_y = A\exp(j\theta), \tag{35}$$

we obtain, by (32),

$$A = \eta\gamma/\{(1-\eta-\gamma^2-\beta^2)^2+\beta^2(2-\eta)^2\}^{1/2}, \tag{36}$$

and

$$\theta = \tan^{-1}\left\{\frac{1-\eta-\gamma^2-\beta^2}{\beta(2-\eta)}\right\}. \tag{36a}$$

Therefore, at cyclotron resonance,

$$A = \eta\gamma_0/\beta(2-\eta), \quad \theta = 0. \tag{37}$$

7. Conclusion

Using the specific inductive capacity, we have derived the expression for the absorption curve at the electron cyclotron resonance of a slightly ionized gas for the hybrid wave. It was shown from the analyses that the behaviour of the resonance absorption by the hybrid wave is very different from that by the transversal wave.

The main features are as follows:

(1) The resonance occurs not at $\omega_c=\omega$ but at $\omega_c=\sqrt{\omega^2-\omega_p^2-\nu_c^2}$;
(2) The absorption curve is not Lorentzian;
(3) The half-width depends not only on collision frequency but also on electron density.

Although the expression for the absorption is more complicated, there is the following advantage in this case. As shown above, one can calculate both the electron density and the collision frequency from the resonance position and the half-width, by measuring one resonance absorption curve. In addition an experimental apparatus becomes simpler. We shall report the experimental data and analyses based on the above discussion in the next part.

Acknowledgments

The author wishes to express his sincere thanks to Prof. I. Takahashi for his guidance throughout this work. The author's thanks are also due to Prof. K. Mitani for discussions.

REFERENCES

1. J. G. Linhart: *Plasma Physics* (North-Holland Publ. Co., 1960), p. 106.
2. L. Spitzer: *Physics of Fully Ionized Gases* (Interscience Publ. Inc., 1956), p. 55.
3. S. K. Mitra: *The Upper Atomosphere* (the Asiatic Society, Calcutta, 1952).
4. M. A. Heald: MATT 17 (1959) Princeton University.
5. E. A. Desloge, S. W. Matthysse & H. Margenau: Phys. Rev. **112** (1958), 1437.
6. T. Dodo: (to be published).
7. D. C. Kelly, H. Margenau & S. C. Brown: Phys. Rev. **108** (1957), 1367.
8. K. Watanabe: Kakuyugo Kenkyu (Nuclear Fusion Research) **5** (1960), 594 (in Japanese).

Memoirs of the College of Science, University of Kyoto, Series A,
Vol. XXIX, No. 3, Article 9, 1961.

ABSORPTION AT ELECTRON CYCLOTRON RESONANCE IN SLIGHTLY IONIZED GASES (III)*

BY

Shigetoshi TANAKA

(*Received March 17, 1961*)

ABSTRACT

It was verified by measuring the loss in a slightly ionized gas ($\eta \lesssim 0.2$) that the absorption curve at electron cyclotron resonance for the hybrid wave ($\boldsymbol{k}_0 \perp \boldsymbol{B}$) is well represented by the expression which was previously derived. It was shown that the electron density and the collision frequency are determined from the resonance position and the half-width of one measured absorption curve. The collision probabilities in neon, argon and helium plasmas were determined from the pressure dependence of the collision frequency which was somewhat larger than those reported by other authors.

1. Introduction

In the second part of this paper**, an expression representing the cyclotron resonance absorption of electrons in a slightly ionized gas was derived for the hybrid wave ($\boldsymbol{k}_0 \perp \boldsymbol{B}$). And it was shown that the resonance occurs at $\omega_c = \sqrt{\omega^2 - \omega_p^2 - \nu_c^2}$ and the absorption curve is not Lorentzian and the half-width depends on the collision frequency and the electron density.

In this part, it has been verified from the experimental studies that the absorption curve for the hybrid wave in dilute plasmas ($\eta \lesssim 0.2$) is given by (6) of II. Accordingly, the electron density and the collision frequency are determined from the resonance position and the half-width of one measured absorption curve***. In addition, collision probabilities in neon, argon and helium plasmas were determined from the pressure dependence of the collision frequency.

For the purely transversal wave ($\boldsymbol{k}_0 /\!/ \boldsymbol{B}$), the theoretical and the experimental studies on the absorption at the electron cyclotron resonance were reported by Brown *et al.* (**2**, **3**) and Goldstein *et al.* (**4**). For the hybrid wave ($\boldsymbol{k}_0 \perp \boldsymbol{B}$), however, there have been very few reports on the resonance absorption. Schneider

* Reported in Japanese in "Kakuyugo Kenkyu (Nuclear Fusion Research)" **5** (Sept. 1960), 283.

** The preceding paper (Part II), referred to as II.

*** This procedure is very similar to the effective mass and the collision frequency being determined from the resonance position and the half-width of the cyclotron resonance of electron and hole in semiconductor (**1**). It is to be noted, however, that the similarity is superficial and the effective mass is not considered in the gaseous plasma.

et al. (5) carried out such experiments on the acetylene flame plasma, but they gave no comment on the shift of the resonance position. Recently, Mitani *et al.* (6), Dodo (7) and Yabumoto (8) have respectively found that the resonance position shifts with increasing electron density.

2. Experimental apparatus

The microwave power absorbed by a slightly ionized gas in a static magnetic field was measured with the apparatus shown in Fig. 1. The gaseous discharge plasma is maintained by D. C. power supply. The micowave (frequency f_s – 9,820 *mc/s*) modulated by 5 *kc/s* square wave, after passing through the plasma-filled guide and a calibrated attenuator, is detected by a crystal detector. The detected signal is amplified by a selective amplifier and then displayed on an oscillograph. The insertion loss of the plasma is substituted by the calibrated attenuator being adjusted. At the fixed signal frequency, the attenuation factor αD at arbitrary tube current and magnetic field is measured, where α is the attenuation constant and D the effective path length of plasma for the microwave. In order to exclude

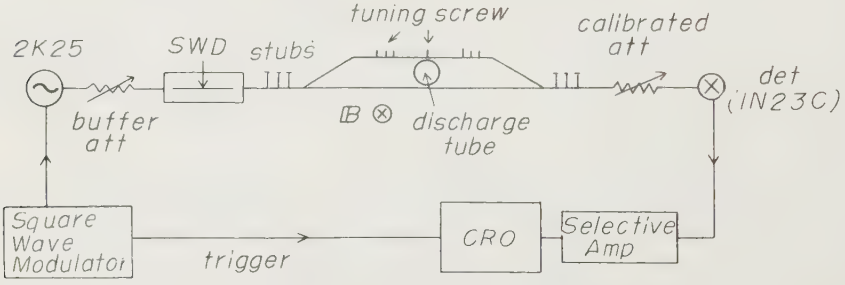

Fig. 1. Block diagram of the apparatus.

the disturbance due to Hall effect, the discharge current is set to be parallel to the magnetic field. In Fig. 2 is shown the magnet. The pole pieces have holes to get a discharge tube inserted, and are so shaped as to collect magnetic flux uniformly in the discharge tube. The discharge tube is in part within a waveguide running perpendicular to it. The waveguide is square and has a side equal to the longer side of standard X-band guides, which are connected through tapered parts to it. The details of the discharge tube relative to a vacuum and gas filling system are given in Fig. 3. A double probe is attached to the tube, outside the magnet. It is to be noted that the electron temperature and density measured by the probe are those in the case of no magnetic field.

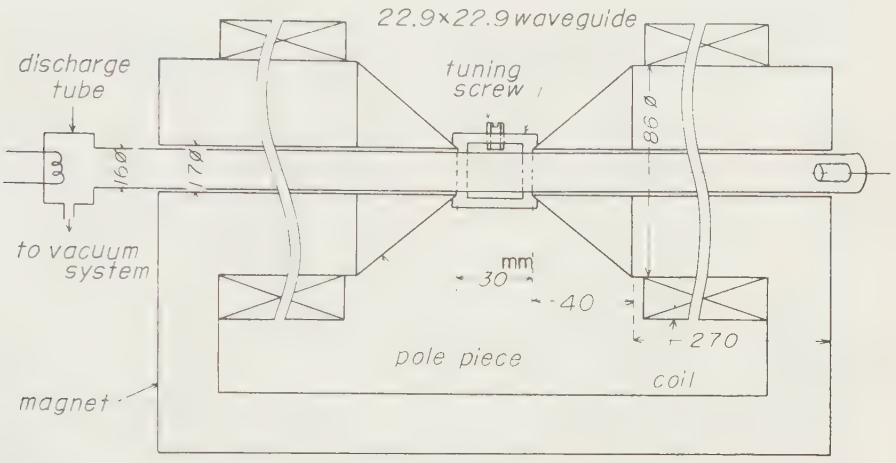

Fig. 2. Waveguide connected with gaseous discharge tube and magnet.

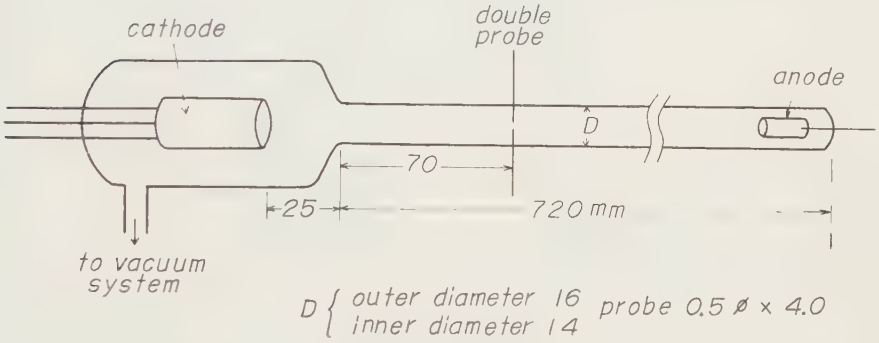

Fig. 3. Discharge tube.

3. Experimental results

Experiments were made on the cyclotron resonance in gaseous discharge plasmas of neon, argon and helium. The neon plasma exhibited a sharp and typical resonance absorption in comparison with other plasmas. Therefore the experiments were performed mainly on the neon plasmas.

In Fig. 4 are shown the absorption (α) curves for the various discharge currents at constant pressure, plotted against magnetic field intensity B and $\gamma \equiv \omega_c/\omega$, assuming the effective plasma length to be constant and the loss zero at far off-resonance positions, since it is negligibly small there. The values of $\eta=(\omega_p/\omega)^2$ and $\beta=\nu_c/\omega$ calculated from the absorption curves are given (see §4). Since p, hence ν_c is kept constant (assuming that collisions between electrons and neutral particles are dominant), these curves show how the resonance absorption varies

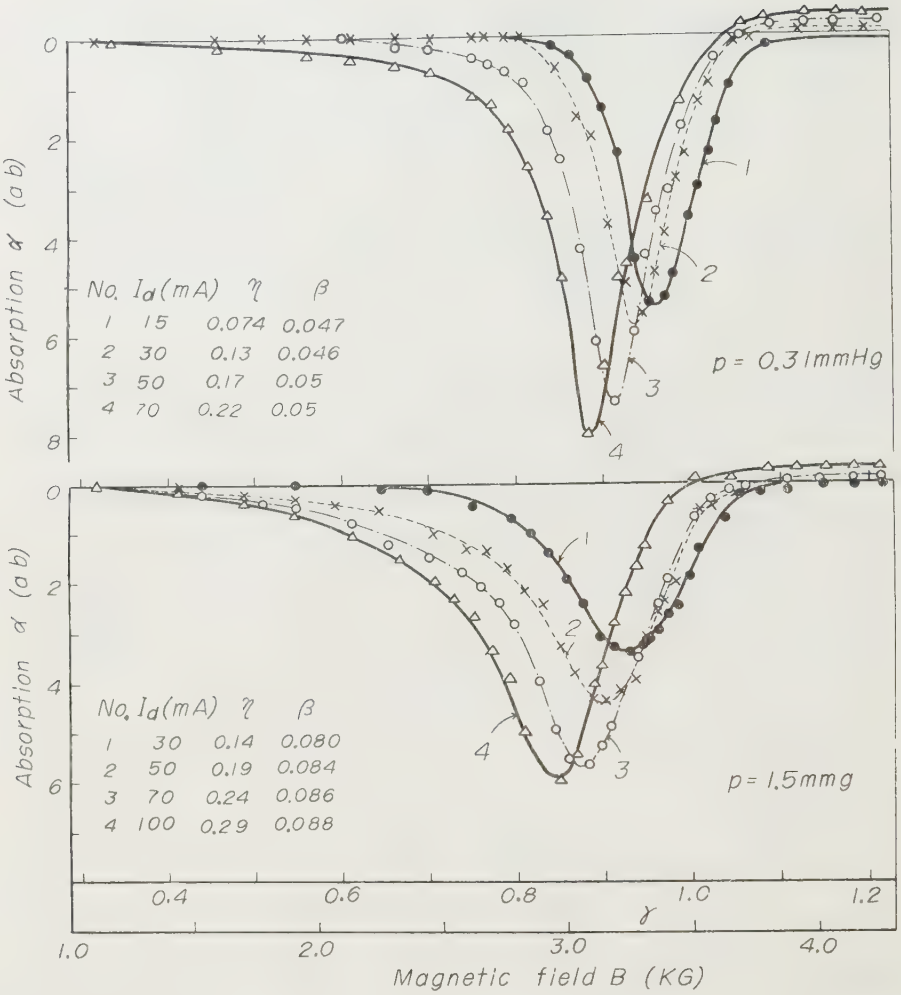

Fig. 4. Absorption curves for neon at constant pressure.

with increasing η and β const.. Accordingly, these experimental curves directly correspond to the theoretical curves given in Fig. 4 of II. In contrast to the previous curves, the absoption curves are shown in Fig. 5 for various values of p or β and I_d= const.. These curves show how the resonance absorption varies with increasing β and η const.. Therefore, these experimental curves correspond to the theoretical ones given in Fig. 5 of II.

Before discussing the results in detail, we shall consider the problems accompanying the experiment.

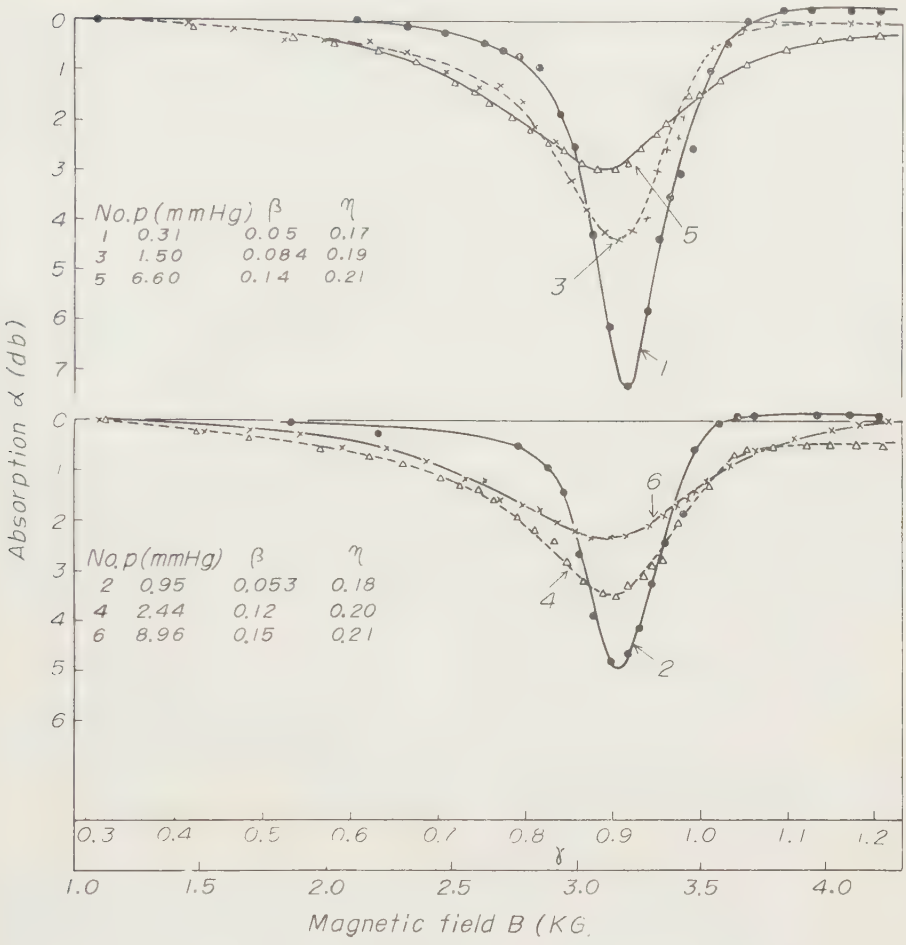

Fig. 5. Absorption curves for neon of constant discharge current (I_d=50 mA.)

(1) *Leakage of microwave power*

If there is leakage of microwave power from two holes on guide walls, in which the discharge tube is set, the leaking wave will propagate in H_{11} mode through the holes in poles of magnet, as circular waveguides. On the other hand, the cutoff wavelength λ_c for such wave is given in the form (**9**):

$$\lambda_c = 2\pi a\sqrt{K_e}/\chi'_{11} = 2.9\nu\sqrt{K_e} \quad (\text{cm}),$$

for the present case. Thus the signal wave (λ=3.05 cm) is beyond the cutoff even if K_e is unity ($K_e<1$ in a plasma), no leakage resulting.

(2) *Reflection of microwave from plasma*

Since the microwave power is measured after passing through the plasma, if

a large variation in reflection power from the plasma occurs in the vicinity of resonance, we shall observe an incorrect large absorption. Actually, the apparent absorption due to reflection at the resonance amounted to about 1 *db*, when the peak absorption due to plasma was 7.5 *db*. In order to avoid such errors, it is better that the matching to the plasma column is a little off, because a constant small reflection rather does not lead to error in our experiments.

(3) *Deformation of plasma column by magnetic field*

Setting discharge current parallel to magnetic field, we can exclude the disturbance due to Hall effect. However, the plasma is concentrated about the axis of the tube with magnetic field intensity being increased, due to the decrease in diffusion loss of electrons to the wall. In our experiments, the diameter of the intensely bright part became about one third of the inner diameter of the tube in the vicinity of resonance ($B \sim 3.5\,KG$). Although the effective path length of plasma for microwave varies by the deformation of plasma column, the experimental data cannot make correction for deformation.

(4) *Uniformity of magnetic field*

The magnetic field between the tapered pole pieces shown in Fig. 2 is not uniform, but the spatial variation of B within the plasma region is below about 3 percent, which may be negligible in our experiments.

(5) *Setting of zero-level of absorption curve*

We took the absorption to be zero at far off-resonance positions. Therefore, strictly the correct zero-level must be somewhat above those shown in Figs. 4 and 5. Moreover, the zelo-level at far off-resonance where $\gamma \ll \gamma_0$ does not correctly coincide with that where $\gamma \gg \gamma_0$. For convenience' sake, we took α to be zero at $\gamma \ll \gamma_0$.

(6) *Impurity gases*

In our experiments, impurity gases such as CO_2, CO, H_2O and N_2 which are emitted from oxide cathode, anode and tube wall at heating will broaden the absorption curve, since their collision probabilities are very large in comparison with sample gases*. So, they present a most troublesome problem.

* Under our experimental conditions in which the electron temperature is estimated to be $2\sim4\times10^4$ (°K), the collision probabilities of these gases are such as follows (**10**):
Ne: 7~8 (cm-mmHg)$^{-1}$, Ar: 10~30, He: 20, CO_2: 20~50, CO: 50~120, H_2O: 60~90, N_2: 40~90.

4. Discussion on experimental results

It was shown in II that for $\eta \ll 1$ the absorption curve can be approximated by:

$$\alpha_{\perp} = \alpha_{\perp m} \frac{\beta^2(2-\eta)^2}{(\gamma_0^2-\gamma^2)^2 + \beta^2(2-\eta)^2}, \tag{1}$$

with $\alpha_{\perp m} = \frac{\pi\eta}{\beta}\frac{1-\eta}{2-\eta}$.

(1) *Shift of resonance position and calculation of electron density*

The resonance takes place at $\gamma=\gamma_0$, where

$$\gamma_0^2 = 1-\eta-\beta^2. \tag{2}$$

In our experiments, β is 0.2 at most, so β^2 in (2) can be neglected against η. γ_0 is determined directly from the absorption curve and η by double probe respectively for various values of discharge current I_d. The experimental results together with the calculated values from (2) are shown in Fig. 6, where the experimental points are contained in respective blocks corresponding to different

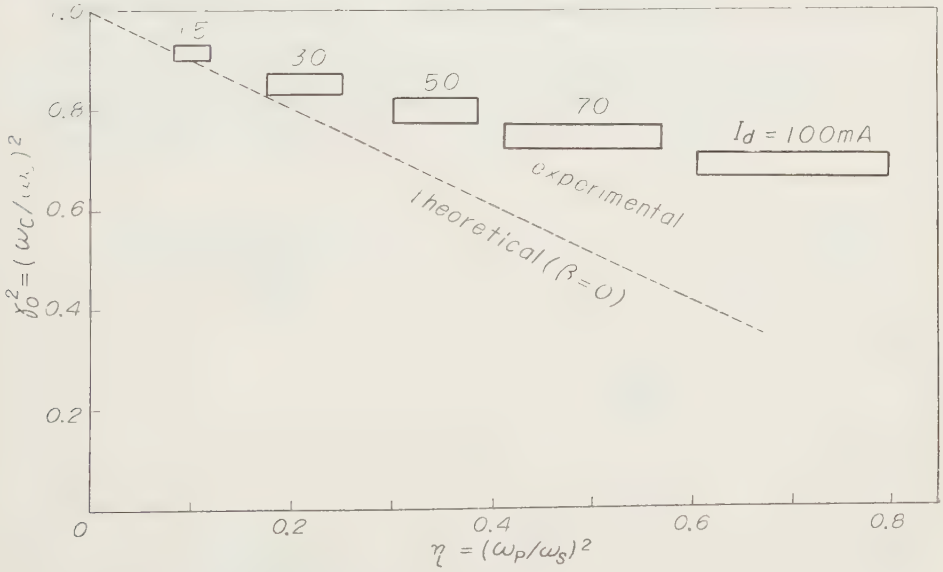

Fig. 6. Variation of reconance position γ_0^2 *versus* electron density η.

values of I_d. It seems to come from the circumstance that the electron density η may increase with increasing pressure as shown in Fig. 8, owing to the decrease of electron mobility. Obviously in Fig. 6, the experimental results agree with the theoretical ones in the domain $\eta \lesssim 0.2$ and $I_d \lesssim 30$ mA. A discrepancy occurs for

larger η, which is natural, since our theory given in (2) is correct only for small η. Thus, for small η, if γ_0 or the shift of the resonance position is measured,

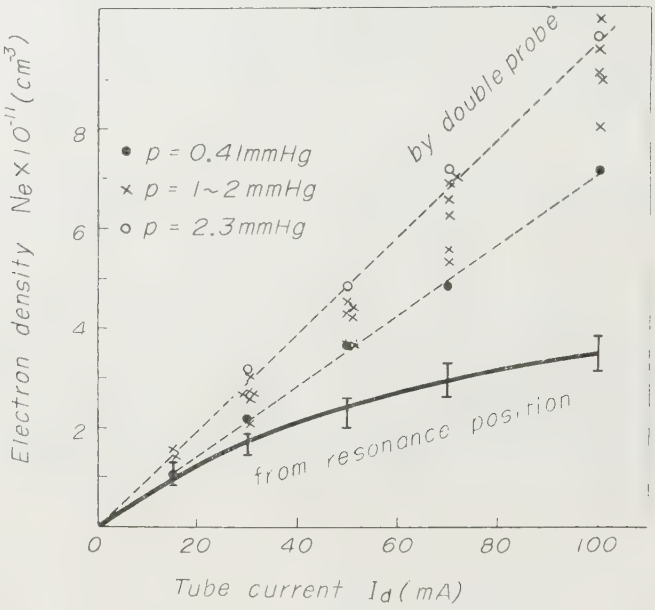

Fig. 7. Comparison between electron densities measured from resonance position and by double probe *versus* tube current.

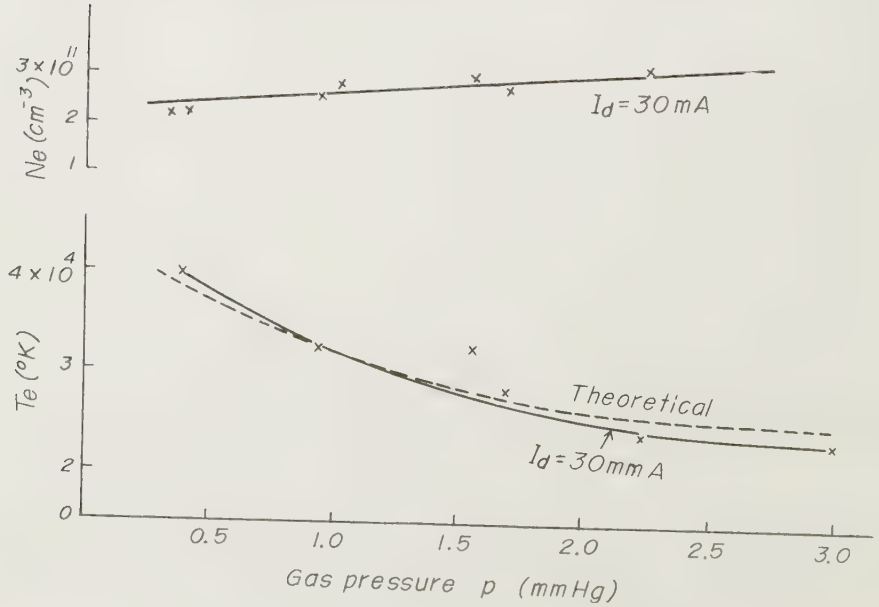

Fig. 8. Variation of T_e and N_e with p for neon.

we can easily calculate γ_i, hence the electron density. In Fig. 7 are shown the electron densities (N_e) measured from resonance position and by double probe *versus* tube current. It is noted here that the electron density measured by probe is that in the case of no magnetic field.

In Fig. 8 are shown the electron density and the temperature (T_e) *versus* pressure which are calculated from double probe measurement according to Johnson-Malter (**11**) assuming $T_i = 400°K$.

(2) *Asymmetry of absorption curves*

The absorption curve plotted against γ is not symmetrical and a measure of asymmetry is given by:

$$\frac{\Delta\gamma}{2} \quad \frac{\Delta\gamma}{2} \quad \beta^2\left(1 \quad \frac{\eta}{2}\right), \tag{3}$$

as shown in II. Therefore, the absorption curve becomes more asymmetrical with increasing β than with increasing η, as it can in fact be seen from the experimental curves in Figs. 4 and 5.

According to (1), however, the absorption curves *versus* γ^2 is symmetrical. In Fig. 9 are plotted the experimental points together with the theoretical curves. Both agree well within the half-width but does not outside and this may be due to the way of setting the zero-level of absorption curve as stated in §3 (5).

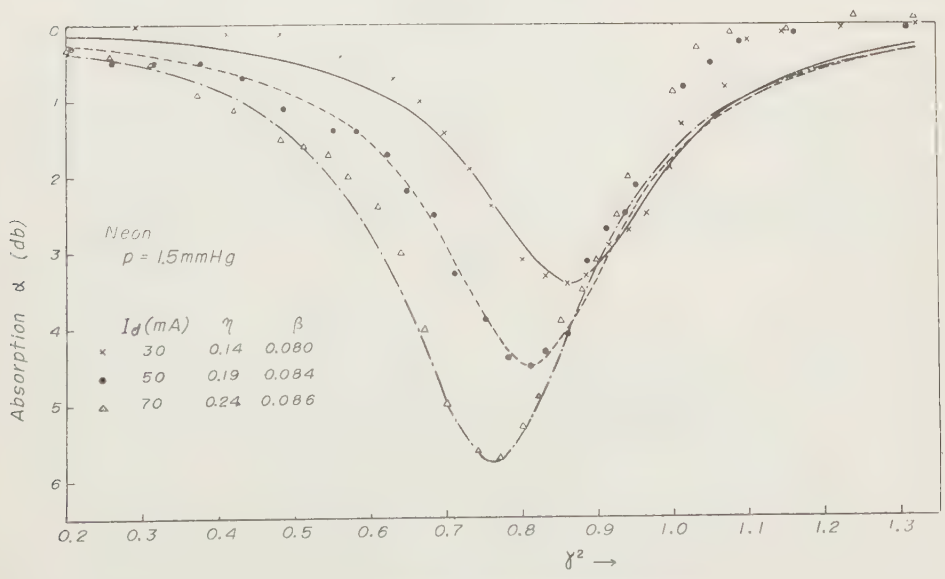

Fig. 9. Comparison between theory and experiment of resonance absorption *versus* γ^2.

(3) *Maximum absorption*

(a) Since $\alpha_{\perp m}=\{(1-\eta)/(2-\eta)\}\pi\eta/\beta$, we have

$$\alpha_{\perp m}\beta = \pi\eta(1-\eta)/(2-\eta) = \text{const.}, \tag{4}$$

if $\eta=$const.. Therefore, $\alpha_{\perp m}$ is inversely proportional to β. Thus, as the pressure is increased with $I_d=$ const., the absorption peaks are lowered. From the experimental data at $I_d=50$ mA given in Fig. 5, $\alpha_{\perp m}\beta$ are obtained as:

0.37, 0.27, 0.37, 0.42, 0.36.

(b) If β const., then

$$\frac{\alpha_{\perp m}}{\eta}\frac{2-\eta}{1-\eta} = \frac{\pi}{\beta} = \text{const.}, \tag{5}$$

which implies that $\alpha_{\perp m}$ is very proportional to η. From the experimental data at $p=1.5$ mm Hg given in Fig. 4, the values given on the left-hand side of (5) are 53, 53, 55, 50.

(4) *Half-width and collision probability*

The relation between the half-width and β is:

$$\Delta\gamma \simeq \left(2+\frac{\eta^2}{4}\right)\beta \quad \text{or} \quad \beta = \frac{1-\eta}{2-\eta}\frac{\Delta B}{B_0}, \tag{6}$$

as shown in II. In Fig. 10 are shown the experimental data on β and ν_c *versus* p, which are obtained from the half-width.

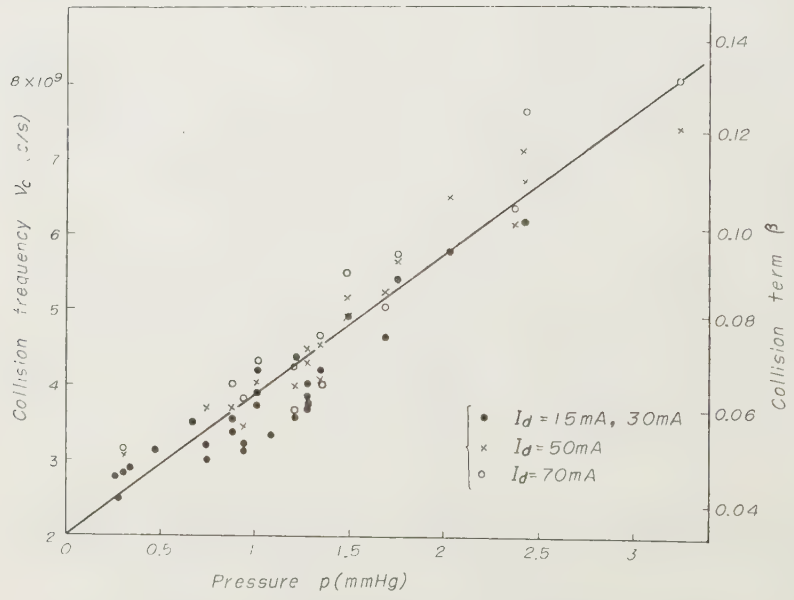

Fig. 10. Variation of collision frequency with pressure for neon,

On the other hand, ν_c is given by (**12**):

$$\nu_c \quad p_0 P_c V , \tag{7}$$

where P_c is the collision probability, $p_0 \quad 273\, p \; T_g$ the reduced pressure in mm Hg and V the average velocity of electron.

For neon, Ramsauer effect is very small and actually P_c can be taken as constant under our experimental conditions, in which the electron temperature varies from $4 \cdot 10^4$ to $2.3 \cdot 10^4$ °K, according to the pressure increase from 0.4 to 3 mm Hg as shown in Fig. 8. V varies by the factor $\sqrt{4/2.3} = 1.32$ in the above pressure range. If this variation of V can be neglected, ν_c depends only on p. From the experimental data in Fig. 10, this relation can be expressed approximately as:

$$\nu_c = 1.9 \times 10^9 p + 2.0 \times 10^9 \quad (c/s) . \tag{8}$$

The constant term independent of p in (8) is very difficult to be interpreted. However, in this case, the electron collisions with tube wall have been neglected in comparison with those with neutral particles, since the gyration radius of electron is about 2×10^{-2} mm even at $B = 3000$ gauss. The impurity gases emitted from electrode and wall, which are independent of p, may be responsible for this term. Such a constant term is seen in Whitmer's report (**13**), in which he has studied the electron loss process in hydrogen gas discharge with the microwave techniques.

From the pressure dependent term in (8), P_c is calculated as:

$$P_c = 25 \text{ cm}^2/\text{cm}^3 \text{ mm Hg} ,$$

where $T_g = 350$ °K and $T_e = 3 \times 10^4$ °K have been taken. This value of P_c is about three times larger than that reported (**10**). One of the reasons why such a large P_c is obtained is that the cyclotron resonance occurs at $\gamma_0^2 = 1 - \eta$, hence the spatial distribution of electron density of our experimental plasma causes naturally the absorption curves to be broadened. Also impurity gases may be responsible for such a large P_c.

5. Experimental results for argon

The experimental results of agron plasmas are similar to those of neon plasmas, except that the collision frequency is somewhat larger and the absorption curves broader. In Fig. 11 are plotted the experimental data on β and ν_c against p. Ramsauer effect of argon gas is very large and the collision probability varies from 12 to 5 cm^2/cm^3 mm Hg (**10**) as the electron temperature decreases from 2×10^4 °K to 1.25×10^4 °K, while the increase of the pressure from 0.5 to 5 mm Hg is accompanied by such a variation of electron temperature. But, neglecting the

Ramsauer effect and the variation of T_e, we assume that ν_c depends only on p, and ν_c can be expressed approximately from Fig. 11 as:

$$\nu_c = 1.4\times10^9 p + 4.0\times10^9 \quad (c/s). \tag{9}$$

Then, taking $T_g = 350\,^\circ\mathrm{K}$ and $T_e = 1.5\times10^4\,^\circ\mathrm{K}$, P_c is calculated as:

$$P_c \simeq 27\ \mathrm{cm^2/cm^3\ mm\ Hg},$$

which is rather larger than that reported (**10**).

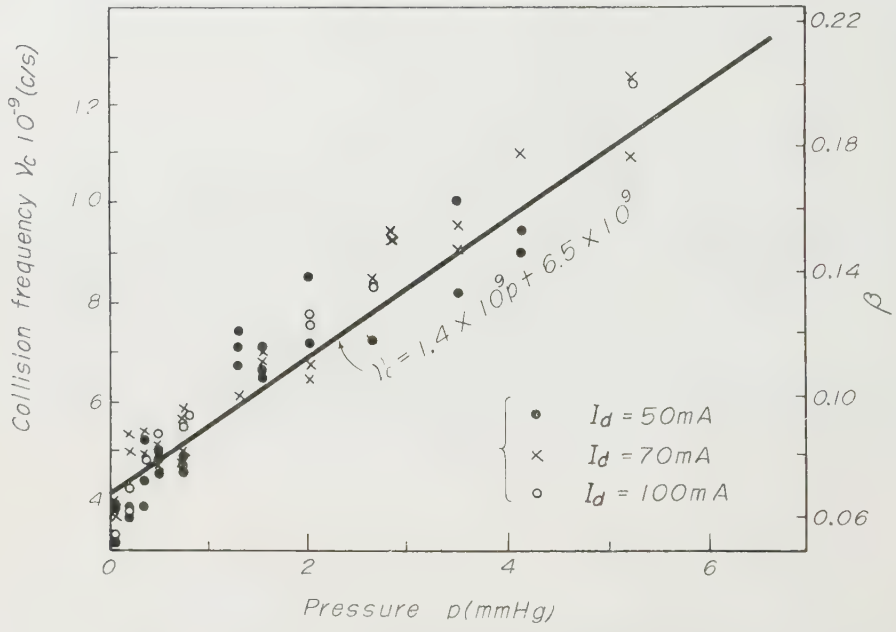

Fig. 11. Variation of collision frequency with pressure for argon.

6. Experimental results for helium

The absorption curves of helium plasma are similar to those of neon and argon, but they are very broad, since the electron temperature is high and the collision probability is large in helium gas. In Fig. 12 are plotted the experimental data on ν_c against p, which can be expressed as:

$$\nu_c = 1.4\times10^9 p + 6.5\times10^9 \quad (c/s). \tag{10}$$

Neglecting the variation of T_e from 4×10^4 to $3\times10^4\,^\circ\mathrm{K}$ as the pressure increases from 2.5 to 6 mm Hg, we can calculate P_c from (10), obtaining

$$P_c \simeq 18\ \mathrm{cm^2/cm^3\ mm\ Hg},$$

where $T_g = 350\,^{\circ}\mathrm{K}$ and $T_e = 3.5 \times 10^4\,^{\circ}\mathrm{K}$ have been taken. This value of P_c is consistent with that reported (**10**) ($P_c = 20$).

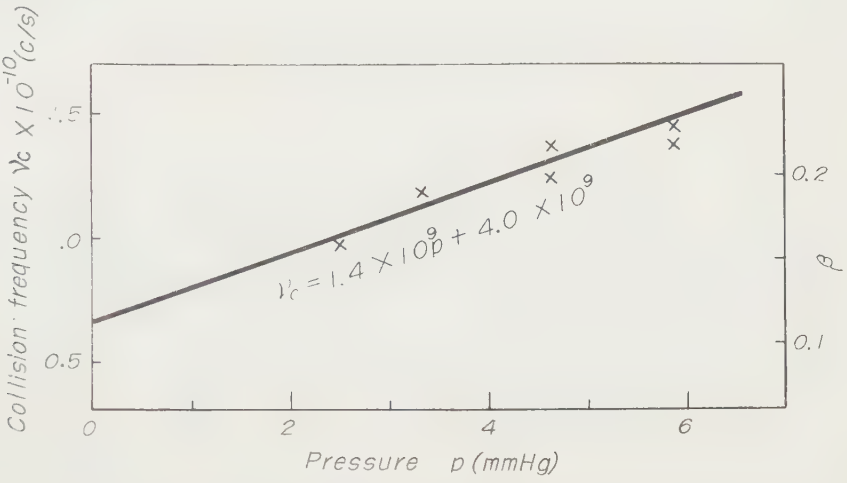

Fig. 12. Variation of collision frequency with pressure for helium.

7. Conclusion

It causes disadvantage for the hybrid wave to be used, that the absorption curve becomes rather complicated in comparison with that for the purely transversal wave, but it is meritorious that the electron density and the collision frequency are determined from the resonance position and the half-width. This circumstance can be applicable as microwave diagnostics to the studies of gaseous discharge plasmas.

Recently, Brown (**3**) has carried out the measurements on the cyclotron resonance radiation for the case of $\boldsymbol{k}_0 \perp \boldsymbol{B}$, and has shown that the resonance position shifts with increasing electron density. His result is consistent with ours if based on Kirchhoff's law. Schneider *et al.* (**5**) have carried out the measurements on the cyclotron resonance absorption for the case of $\boldsymbol{k}_0 \perp \boldsymbol{B}$, but wrongly discussed the result, using the absorption factor for $\boldsymbol{k}_0 /\!/ \boldsymbol{B}$. Practically, however, their results are not incorrect fortunately, because their measurements were made on very dilute plasmas ($\eta \approx 0.002$).

Finally, since there are boundaries to the test plasma generated in our laboratories, the effect of boundary must be considered, as considered in another report (**14**). Also, it will be necessary to consider the effect of long range Coulomb interaction (*e-i* and *e-e* collisions) and the effect of thermal energy of electrons and ions upon the electron cyclotron resonance.

Acknowledgments

In conclusion, the author wishes to express his sincere thanks to Prof. I. Takahashi for his guidance and to Prof. K. Mitani for his discussions. Thanks are also due to Prof. Y. Uchida and Dr. K. Fukuda for the convenience given to use electromagnet.

REFERENCES

1. G. Dresselhaus, A. F. Kip and C. Kittel: Phys. Rev. **90** (1955), 368.
2. D. C. Kelly, H. Margenau and S. C. Brown: Phys. Rev. **108** (1957), 1367.
3. S. C. Brown: *Proc. of the 4th Intern. Conf. on Ionized Phenomena in Gases*, Uppsala, Aug., 1959 (IIIC 691).
4. L. Goldstein *et al.*: Technical Report No. **3** (1954) and Scientific Report No. **2** (1957), (University of Illinois).
5. J. Schneider and F. W. Hoffman: Phys. Rev. **116** (1959), 244.
6. K. Mitani and H. Kubo: (private communication).
7. T. Dodo: (private communication).
8. T. Yabumoto: (private communication).
9. N. Marcuvitz: *Waveguide Handbook* (McGraw-Hill Co., Inc., 1951), p. 70.
10. S. C. Brown: *Basic Data of Plasma Physics* (John Wiley & Sons, Inc., 1959) pp. 7~17.
11. E. O. Johnson and L. Malter: Phys. Rev. **80** (1950), 58.
12. S. C. Brown: ibid. p. 3.
13. R. F. Whitmer: Phys. Rev. **104** (1956), 572.
14. S. Tanaka: Kakuyugo Kenkyu (Nuclear Fusion Research) **5** (1960), 604 (in Japanese).

Memoirs of the College of Science, University of Kyoto, Series A,
Vol. XXIX, No. 3, Article 10, 1961.

MICROWAVE CONDUCTIVITY OF BOUNDED PLASMA*

BY

Shigetoshi TANAKA

(*Received March 17, 1961*)

ABSTRACT

An expression for microwave conductivity of bounded plasma was derived in the absence of magnetic field and then another similar expression in the presence of it, introducing the depolarization effect in each case. It was shown that this effect is to replace ω in specific inductive capacity for unbounded plasma by $\omega' - \omega\{1 - L(\omega_p/\omega)^2\}$. The results were as follows: (i) plasma resonance occurs at $\omega = \sqrt{L}\,\omega_p$, (ii) magneto-plasma resonance occurs at two positions of electron density at each magnetic field, both for the transversal wave ($\boldsymbol{k}_0 // \boldsymbol{B}$) and for the hybrid wave ($\boldsymbol{k}_0 \perp \boldsymbol{B}$).

1. Introduction

Microwave conductivities of plasma in the absence of or in the presence of magnetic field have been studied by various workers (**1, 2**), since Margenau's first report was published (**3**). The expressions for conductivity have so far been derived by solving the Boltzmann transport equation for distribution function of electrons moving under the Lorentz force. The experimental results on the interaction between plasma and microwave have been analysed in the theories (**4, 5**).

In these theories, the plasma was considered to extend through infinite space (unbounded plasma). It is not only theoretically interesting but also experimentally important to study the interaction of bounded plasma with microwave, since the experimental plasma generated in our laboratories is actually bounded.

Investigation on bounded plasmas with no magnetic field was made first by Tonks (**6**) and he reported "plasma resonance" which depends on both electron density and geometrical configuration of plasma. Thereafter, the plasma resonance for the cylindrical plasma has been studied theoretically and experimentally by many researchers (**7**~**11**). Moreover, the plasma resonance for plasma confined between parallel plates was theoretically investigated in detail by Wolff (**12**), by solving the Boltzmann transport equation for spatial distribution of electron density.

In studies on cyclotron resonance of electron and hole in semiconductor, Kittel *et al.* (**13**) considered the influence of boundaries, and introducing the

* Reported in Japanese in "Kakuyugo Kenkyu (Nuclear Fusion Research)" **5** (1960), 604.

depolarization effect they discussed "magnetoplasma resonance" which depends on both electron density and geometrical configuration.

In this report, the microwave conductivity of bounded plasma in the absence of as well as in the presence of magnetic field was studied by introducing the depolarization effect, similarly to the research on semiconductor by C. Kittel *et al.*

2. Depolarization effect of bounded plasma

For simplicity we consider the plasma of uniform electron density with axial symmetry whose axis, when it is in the presence of magnetic field ($\boldsymbol{B}$), should coincide with the direction of $\boldsymbol{B}$. Thus, a spherical or a circular cylindrical plasma is considered (see Fig. 1), in which the electric vector of electromagnetic wave lies and is uniform in transversal plane to $\boldsymbol{B}$, and the frequency is so high that ions can be assumed to be at rest. Then, the electron gas is subject

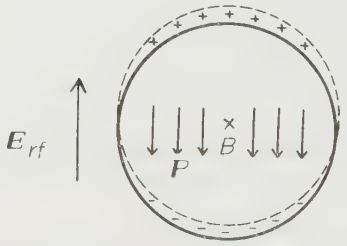

Fig. 1. Depolarization of bounded plasma.

to rigid-body displacement in transversal plane from equilibrium position and surface charges appear on boundary surfaces of bounded plasma. The induced field opposite to the external field exerts the force upon the electron gas, tending to return it to its original position. The effect of this restoring force of plasma may be taken into account by introducing a depolarizing field, $(-\boldsymbol{LP}/\varepsilon_0)$, which is uniform in transversal plane. Then, the internal electric field is:

$$\boldsymbol{E}_i = \boldsymbol{E} - \boldsymbol{LP}/\varepsilon_0 , \tag{1}$$

where L is the depolarizing factor associated with the plasma shape and given by:

$$L \quad \begin{cases} 1/3 \text{ for spherical plasma,} \\ 1/2 \text{ for circular cylindrical plasma.} \end{cases}$$

The polarization $\boldsymbol{P}$ due to displacement of electrons is:

$$\boldsymbol{P} = eN\boldsymbol{x} = eN\int \boldsymbol{v}dt = jeN\boldsymbol{v}/\omega , \tag{2}$$

where x, v are displacement and velocity of respective electron and N is electron density, taking the time dependence as $\exp(-j\omega t)$. Substituting (2) into (1), the internal field is:

$$\boldsymbol{E}_i = \boldsymbol{E} - j\frac{LeN}{\varepsilon_0\omega}\boldsymbol{v}\,. \tag{3}$$

The equation of motion for an electron in unbounded infinite plasma under the influence of constant magnetic field and rf electric field is given by:

$$m(-j\omega+\nu)\boldsymbol{v} = e(\boldsymbol{E}+\boldsymbol{v}\times\boldsymbol{B})\,, \tag{4}$$

where ν is the effective collision frequency. On the other hand, for the bounded plasma the equation of motion is:

$$m\left\{-j\omega\left(1-L\frac{\omega_p^2}{\omega^2}\right)+\nu\right\}\boldsymbol{v} = e(\boldsymbol{E}+\boldsymbol{v}\times\boldsymbol{B})\,, \tag{5}$$

where ω_p is the plasma frequency. Thus, the effect of depolarization is to replace ω by ω', which is:

$$\omega' = \omega\left\{1-L(\omega_p/\omega)^2\right\} = \omega(1-L\eta)\,. \tag{6}$$

It is noted that the uniformity of the depolarizing electric field in the transversal plane is necessary for the above conclusion, as it is satisfied in this case.

3. Plasma resonance in absence of magnetic field

By substituting ω' for ω in the specific inductive capacity K for the unbounded plasma, K for the bounded plasma is given by:

$$K = 1-\frac{1}{\{1-L(\omega_p/\omega)^2\}}\,\frac{(\omega_p/\omega)^2}{\{1-L(\omega_p/\omega)^2\}+j\nu/\omega}\,, \tag{7}$$

or using Brown's notations (5),

$$K = 1-\frac{1}{1-L\eta}\,\frac{\eta}{(1-L\eta)+j\beta}\,. \tag{8}$$

(a) Refractive index n

From (8), n at zero collision limit is given by:

$$n^2 = 1-\frac{\eta}{(1-L\eta)^2}\,. \tag{9}$$

In Fig. 2 n^2 is plotted against η for $L=1/2$. In this figure, the dotted curve presents the dispersion curve for unbounded plasma ($L=0$).

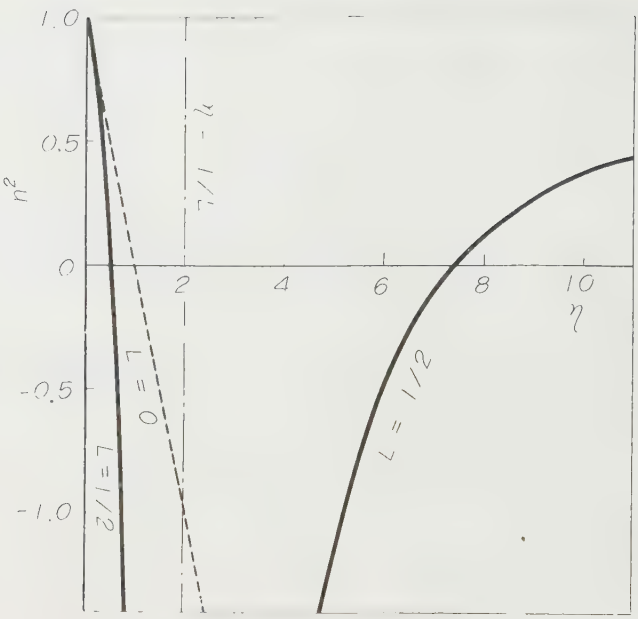

Fig. 2. Dispersion curves for bounded plasma.

(*b*) *Conductivity*

From (8), the real conductivity (σ_R) is given by:

$$\frac{\sigma_R}{\sigma_0} = \frac{\beta^2}{(1-L\eta)^2+\beta^2}, \tag{10}$$

where $\sigma_0 = e^2N/m\nu$ is the static conductivity. According to (10), plasma resonance occurs at

$$1-L\eta = 0 \quad \text{or} \quad \omega = \sqrt{L}\,\omega_p, \tag{11}$$

as shown in Fig. 3.

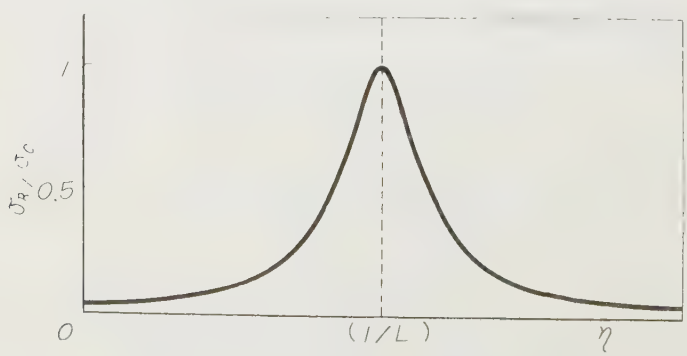

Fig. 3. Resonance absorption curve for bounded plasma.

Especially, the plasma resonance of circular cylindrical plasma ($L = 1/2$) occurs at:

$$\omega = \omega_p/\sqrt{2} \ , \tag{11a}$$

which was called the transverse resonance of plasma column by Gould (**14**). This plasma resonance has been studied by various workers (**6~11**). Solving the electric fields inside and outside the circular cylindrical plasma, Herlofson obtained the result (11a) (**11**).

4. Magnetoplasma resonance for transversal wave ($k_0 /\!/ B$)

A linearly polarized wave incident on an infinite slab of plasma in a parallel magnetic field is split up into two circularly polarized waves, the right-handed and the left-handed waves with different phase velocities (**15, 16**). We consider a wave propagating through a circular cylindrical plasma, along the magnetic field, parallel to the cylinder axis.

(*a*) *Right-handed circularly polarized wave*

The specific inductive capacity K_- for the bounded plasma is:

$$K_- = 1 - \frac{1}{(1-L\eta)} \frac{\eta}{(1-L\eta-\gamma)+j\beta} \cdot \tag{12}$$

Accordingly, n_- at zero collision limit is given by:

$$n^2 = 1 - \frac{\eta}{(1-L\eta)(1-L\eta-\gamma)} \cdot \tag{13}$$

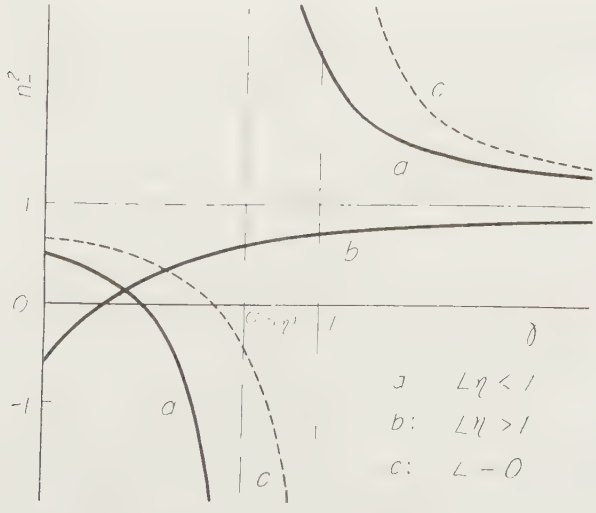

Fig. 4. Dispersion curves for right-handed wave.

n_-^2 is plotted against γ with η const. in Fig. 4, which shows that n_-^2 increases to infinity at $\gamma=1-L\eta$ for the case of $L\eta<1$. As n_-^2 increases to infinity at $\gamma=1$ for infinite plasma ($L=0$), as is represented by a dotted curve, the effect of depolarization results in the displacement of n_-^2-axis by $(-L\eta)$.

On the other hand, σ_R is given by:

$$\frac{\sigma_R}{\sigma_0}=\frac{\beta^2}{(1-L\eta-\gamma)^2+\beta^2}. \tag{14}$$

From (14), the cyclotron resonance for the bounded plasma ($\sigma_{R\max}$), which is called magnetoplasma resonance, occurs at

$$\gamma_0=1-L\eta. \tag{15}$$

The resonance position γ_0 *versus* η is shown in Fig. 5, which implies that the magnetic field γ_0 at resonance decreases with increasing electron density η. For $\eta>1/L$, the resonance does not occur, as γ_0 becomes negative. The resonance absorption curve represented by (14) has the half-width $\Delta\gamma=2\beta$. It is to be noted that for the unbounded plasma, $\gamma_0=1$ independently of η.

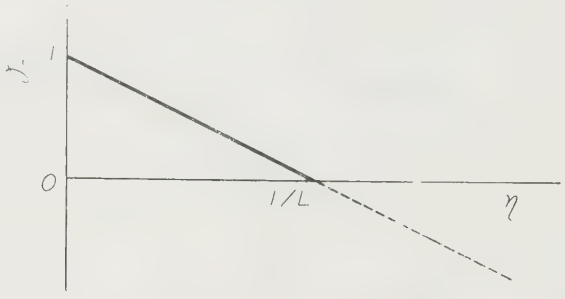

Fig. 5. γ_0 *versus* η for right-handed wave.

(*b*) *Left-handed circularly polarized wave*

Similarly K_+ of the left-handed wave is:

$$K_+=1-\frac{1}{(1-L\eta)}\frac{\eta}{(1-L\eta+\gamma)+j\beta}. \tag{16}$$

Accordingly, n_+ at zero collision limit is given by:

$$n_+^2=1-\frac{\eta}{(L\eta-1)(L\eta-1-\gamma)}. \tag{17}$$

n_+^2 *versus* γ with $\eta=$const. is plotted in Fig. 6, which shows that n_+^2 increases to infinity at $\gamma=L\eta-1$ for the case of $L\eta>1$, but it monotonously increases to unity for the case of $L\eta<1$, in contrast to the infinite plasma ($L=0$), in which n_+^2

monotonously increases to unity as showh by a dotted curve in Fig. 6.

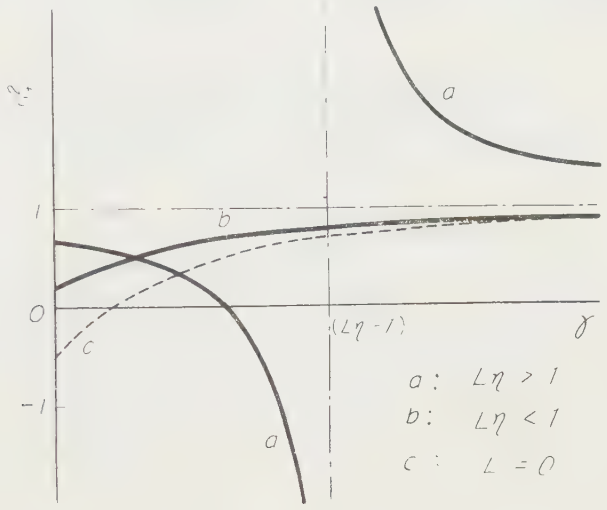

Fig. 6. Dispersion curves for left-handed wave.

Next, σ_R is given by:

$$\frac{\sigma_R}{\sigma_0} = \frac{\beta^2}{(L\eta - 1 - \gamma)^2 + \beta^2}, \tag{18}$$

which implies that the magnetoplasma resonance occurs at

$$\gamma_0 = L\eta - 1. \tag{19}$$

Therefore, although the cyclotron resonance does not occur for the infinite plasma, the magnetoplasma resonance occurs at γ_0 for the bounded plasma in the range $L\eta > 1$. In Fig. 7 the resonance position γ_0 is plotted against η.

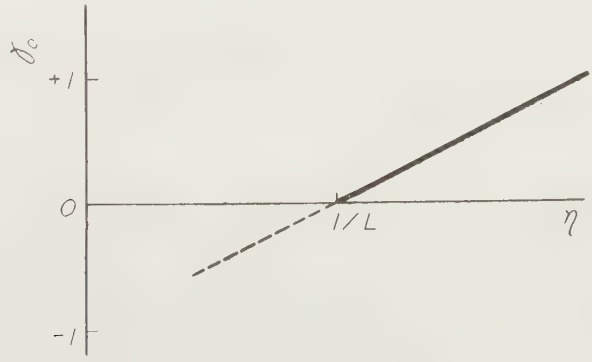

Fig. 7. γ_0 *versus* η for left-handed wave.

(c) Linearly polarized wave

Combining the right-handed and the left-handed waves, σ_R for the linearly polarized wave is given by:

$$\frac{\sigma_R}{\sigma_0} = \beta^2 \frac{(1-L\eta)^2+\gamma^2+\beta^2}{\{(1-L\eta)^2-\gamma^2-\beta^2\}^2+4\beta^2(1-L\eta)^2}\,. \tag{20}$$

Accordingly, the magnetoplasma resonance occurs approximately at γ_0 given by:

$$\gamma_0^2 = (1-L\eta)^2-\beta^2\,. \tag{21}$$

In Fig. 8 the resonance position γ_0 is plotted against η. It is evident from this figure that the resonance occurs at two positions of η, when the electron density η is varied with the magnetic field fixed. This is characteristic of the bounded plasma. It is to be noted that the resonance at the smaller η is due to the right-handed wave and that at the larger η to the left-handed.

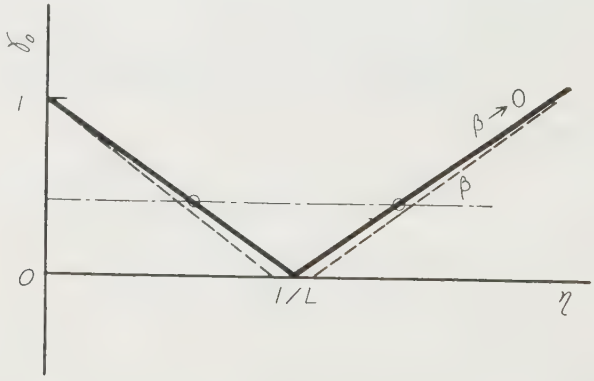

Fig. 8. γ_0 *versus* η for transversal wave ($\boldsymbol{k}_0 /\!/ \boldsymbol{B}$).

The absorption curve(σ_R *versus* γ) is asymmetric and its half-width ($\Delta\gamma$) is:

$$\frac{1}{\gamma_0}\frac{\Delta\gamma_+}{2} = \left|-1+\sqrt{1\mp 2\beta\frac{1}{\gamma_0^2}L\eta}\right|. \tag{22}$$

For $\beta^2 \ll 1$, $\Delta\gamma$ is approximated by:

$$\Delta\gamma \simeq 2\beta\,, \tag{22a}$$

with the exception of $\gamma_0^2 \simeq 0$.

McGrath *et al.* (**17**) derived (20) in a similar way, but they made error in taking L 1. From the experimental studies on the cyclotron resonance of the afterglow, they reported that there may be two resonance positions for each magnetic field actually.

5. Magnetoplasma resonance for hybrid wave ($k_0 \perp B$)

We consider a wave propagating perpendicularly to the cylinder axis. $K_\perp$ for the hybrid wave is given by:

$$K_\perp = 1-\frac{\eta}{1-L\eta}\,\frac{(1-L\eta)^2-\eta+j\beta(1-L\eta)}{(1-L\eta)\{(1-L\eta)^2-\eta-\gamma^2-\beta^2\}+j\beta\{2(1-L\eta)^2-\eta\}}. \tag{23}$$

Accordingly, $n_\perp$ at zero collision limit is given by:

$$n_\perp^2 = 1-\eta\,\frac{(1-L\eta)^2-\eta}{(1-L\eta)^2\{(1-L\eta)^2-\eta-\gamma^2\}}. \tag{24}$$

The dispersion occurs as follows:

[A-I] $1-L\eta=0$

(a) $\gamma_0^2=1-L\eta^2-\eta=0$

$n_\perp^2$ increases to infinity at $\gamma^2=\gamma_0^2$, as shown in Fig. 9, in which $n_\perp^2$ is plotted against γ^2 with $\eta=$const..

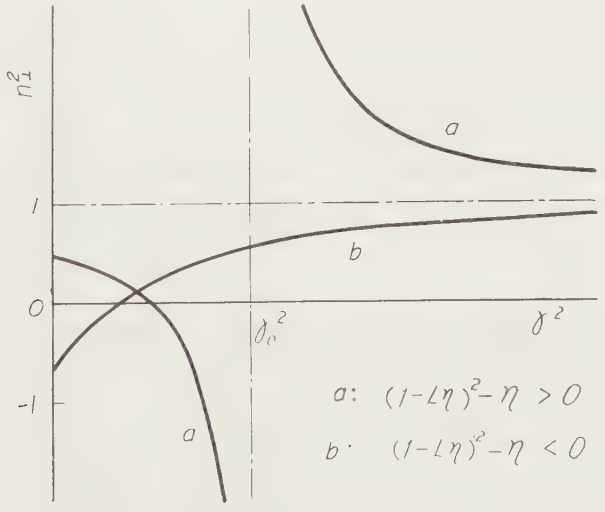

Fig. 9. Dispersion curves for hybrid wave ($k_0 \perp B$).

(b) $\gamma_0^2=(1-L\eta)^2-\eta<0$

$n_\perp^2$ increases monotonously to unity as γ^2 increases. The dispersion is similar to that for the infinite plasma, for which $\gamma_0^2=1-\eta$ is taken. It is to be noted, however, that there are two η-regions where $\gamma_0^2>0$ for the bounded plasma, while there is one η-region where $\gamma_0^2>0$ for the unbounded plasma (as discussed later).

[A-II] $1-L\eta=0$

According to (24), $n_{\perp}^2 = -\infty$ for any γ, and this is the same condition that was discussed in § 3.

Next, σ_R is given by:

$$\frac{\sigma_R}{\sigma_0} = \beta^2 \frac{\{(1-L\eta)^2-\eta\}^2+(1-L\eta)^2(\gamma^2+\beta^2)}{(1-L\eta)^2\{(1-L\eta)^2-\eta-\gamma^2-\beta^2\}^2+\beta^2\{2(1-L\eta)^2-\eta\}^2}. \tag{25}$$

Therefore, the magnetoplasma resonance occurs approximately at γ_0 obtained from the following equation:

$$(1-L\eta)^2\left\{(1-L\eta)^2-\eta-\gamma_0^2-\beta^2\right\}^2 = 0. \tag{26}$$

[B-I] $1 \quad L\eta < 0$

The resonance position γ_0 is given approximately by

$$\gamma_0^2 = (1-L\eta)^2-\eta-\beta^2 = \left\{L\eta-\left(1+\frac{1}{2L}\right)\right\}^2-\left(\frac{1}{L}+\frac{1}{4L^2}\right)-\beta^2, \tag{27}$$

which is plotted against η in Fig. 10.

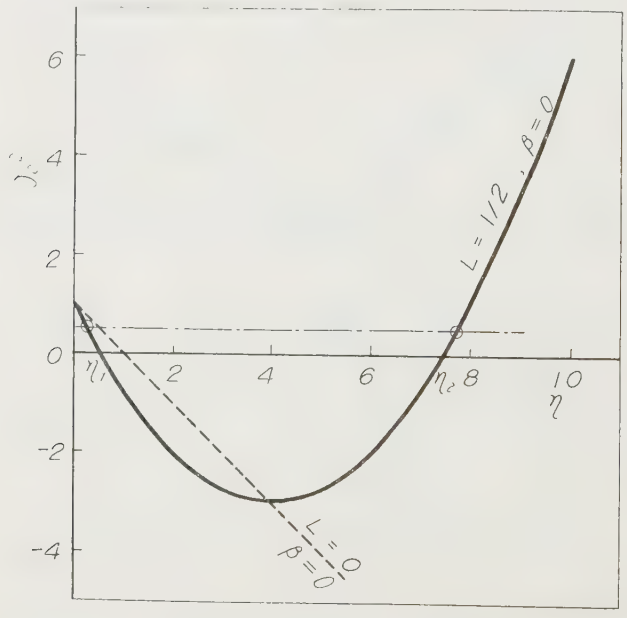

Fig. 10. γ_0^2 *versus* η for hybrid wave ($\boldsymbol{k}_0 \perp \boldsymbol{B}$).

Since the inequality $\gamma_0^2 > 0$ must be satisfied, the resonance occurs only in the following two η-regions:

$$0 < \eta < \eta_1 \quad \text{and} \quad \eta > \eta_2, \tag{28}$$

where

$$\left.\begin{matrix}\eta_1\\ \eta_2\end{matrix}\right\} = \frac{(2L+1)\mp\sqrt{4L(1+L\beta^2)+1}}{2L^2}, \quad (\eta_1<\eta_2). \tag{29}$$

On the contrary, for the unbounded plasma the resonance position is given by:

$$\gamma_0^2 = 1-\eta-\beta^2,$$

which implies that the resonance occurs in the region $\eta<1-\beta^2$ only, as shown in Fig. 10. Therefore, it is characteristic to the bounded plasmas that the resonance occurs at two positions of η at a fixed magnetic field γ.

The absorption curve (σ_R *versus* γ) is asymmetric and its half-width ($\Delta\gamma$) is:

$$\frac{1}{\gamma_0}\frac{\Delta\gamma}{2} = \left|-1+\sqrt{1\mp\frac{\beta}{\gamma_0^2}\left\{2(1-L\eta)-\frac{\eta}{1-L\eta}\right\}}\right|. \tag{30}$$

For $\beta^2\ll 1$, $\Delta\gamma$ is approximated by:

$$\frac{\Delta\gamma}{2} = \frac{\beta}{\gamma}\left\{(1-L\eta)-\frac{\eta}{2(1-L\eta)}\right\}, \tag{30a}$$

with the exception of $\gamma_0^2\simeq 0$.

[B-II] $1-L\eta=0$

From (25), $\sigma_R/\sigma_0=1$ is obtained for any γ. The resonance is the same as discussed in § 3. The plasma resonance appears independently of a magnetic field. According to Dattner's experiments (9), this conclusion may be true, although the resonance absorption curve becomes complicated with increasing magnetic field.

6. Conclusion

Introducing the depolarization effect, the expressions for microwave conductivity for the bounded plasma in the absence of as well as in the presence of magnetic field were derived. It was shown that this effect is to replace ω in the specific inductive capacity for the unbounded plasma by $\omega'=\omega\{1-L(\omega_p/\omega)^2\}$.

The characteristic properties of the bounded plasma are summerized as follows:

(i) Plasma resonance occurs at $\omega=\sqrt{L}\,\omega_p$ both in the absence of and in the presence of magnetic field.

(ii) Magnetoplasma resonance occurs for both the left-handed wave and the right-handed and therefore, there are two resonance positions of electron density η at each magnetic field γ both for the transversal wave ($\boldsymbol{k}_0/\!/\boldsymbol{B}$) and for the hybrid wave ($\boldsymbol{k}_0\perp\boldsymbol{B}$).

It has been assumed in these derivations that the electron density and the polarization induced are spatially uniform in the transversal plane. For the

actual plasma, however, the electron density is not uniform in the plasma. Also, the surface charge induced, if the plasma is inserted within a waveguide, on the guide wall has been neglected above.

Acknowledgments

The author wishes to express his sincere thanks to Prof. I. Takahashi for his guidance throughout this work. The author's thanks are also due to Prof. K. Mitani, to Prof. S. Takeda of Nagoya University and to Mr. H. Ikegami of Electrical Communication Laboratory for their discussions.

REFERENCES

1. H. Margenau *et al.*: Phys. Rev. **109** (1958), 6; **112** (1958), 1437.
2. D. C. Kelly: Phys. Rev. **119** (1960), 27.
3. H. Margenau: Phys. Rev. **69** (1946), 508.
4. for example, J. M. Anderson & L. Goldstein: Phys. Rev. **100** (1955), 1037.
5. S. C. Brown: Proc. 2nd. International Conf. on the Peaceful Uses of Atomic Energy, Geneva. No. P/387 (1958).
6. L. Tonks: Phys. Rev. **37** (1931), 1458; **38** (1931), 1219.
7. N. Herlofson: Arkiv. Fysik **3** (1951), 247.
8. D. Rommel: Nature **167** (1951), 243.
9. A. Dattner: Ericsson Technics **2** (1957), 309.
10. G. B. Boyd: Technical Report No. **11** (1959), California Institute of Technology.
11. W. D. Hershberger: J. Appl. Phys. **31** (1960), 417.
12. P. A. Wolff: Phys. Rev. **103** (1956), 845.
13. G. Dresselhaus, A. F. Kip & C. Kittel: Phys. Rev. **98** (1955), 368.
14. F. H. Clauser: *Symposium of Plasma Dynamics* (Addison-Wesley Publ. Co. 1960), p. 111.
15. for example, J. G. Linhart: *Plasma Physics* (North-Holland Publ. Co. 1960), p. 106.
16. S. Tanaka: Memoirs of the College of Science, University of Kyoto (to be published).
17. L. P. McGrath, A. F. Chatterjee & J. P. Monier: Scientific Report No. **2** (1957), University of Illinois.

INDEX OF AUTHORS TO VOLUME XXIX

PAGE

Fujiki, Y.—A New Compound in Au–Pd Alloy System. 197

Fukunaga, K. (see **Nakamura, T., Fukunaga, K., Takamatsu, K.** and **Yasumi, S.**) 141

Hashi, T., Hirai, A., Sasaki, M. and **Kawai, T.**—Nuclear Magnetic Resonance Pulse Apparatus. 205

Hattori, A. and **Yada, B.**—Optical Observations of the Second Russian Earth Satellite. 107

Hirai, A. (see **Hashi, T., Hirai, A., Sasaki, M.** and **Kawai, T.**). 205

Hirai, A.—Temperature Dependence of Spin Lattice Relaxation Time of Cl^{35} in Pure Quadrupole Resonance. 257

Hirai, A. and **Kawai, T.**—NMR Pulse Apparatus and its Application to the Investigation of Internal Motion of High Polymer (Poly-propylene). 345

Ishida, Y.—Ultrasonic Velocity and Adiabatic Compressibility of Mixture of Sulfuric Acid and Water. 91

Ishida, Y.—Adiabatic Compressibility of Aqueous Solution of Inorganic Acid. . . . 187

Itoh, H. (see **Ogata, H., Itoh, H., Masuda, Y., Takamatsu, K., Kawashima, M., Masaike, A.** and **Kumabe, I.**). 267

Kamitsuki, A.—On the Seismic Waves reflected at the Mohorovičić Discontinuity (II). 19

Kamitsuki, A.—On Local Character of Poisson's Ratio in the Earth's Crust. . . . 163

Kamitsuki, A.—On Azimuthal Distribution of the Crustal Poisson's Ratio in case of Earthquake Occurrence. 213

Kawai, T. (see **Hashi, T., Hirai, A., Sasaki, M.** and **Kawai, T.**). 205

Kawai, T. (see **Hirai, A.** and **Kawai, T.**). 345

Kawashima, M. (see **Ogata, H., Itoh, H., Masuda, Y., Takamatsu, K., Kawashima, M., Masaike, A.** and **Kumabe, I.**). 267

Kumabe, I. (see **Ogata, H., Itoh, H., Masuda, Y., Takamatsu, K., Kawashima, M., Masaike, A.** and **Kumabe, I.**). 267

Masaike, A. (see **Ogata, H., Itoh, H., Masuda, Y., Takamatsu, K., Kawashima, M., Masaike, A.** and **Kumabe, I.**). 267

Masuda, Y. (see **Ogata, H., Itoh, H., Masuda, Y., Takamatsu, K., Kawashima, M., Masaike, A.** and **Kumabe, I.**). 267

Mikumo, T.—On the Periods of Seismic Waves observed in Local Earthquakes. . . 1

Mikumo, T.—A Consideration on Generation Mechanism of Local Earthquake. . . . 221

Nakamura, T. Fukunaga, K., Takamatsu, K. and **Yasumi, S.**—Absolute Measurement of γ-quanta. 141

Nakau, T.—Magnetic Resonance in $Ti_mMg_nFe_{3-m-n}O_4$ Ferrites and their Magnetization. 241

Nishitake, T.—On the Materials in the Earth's Mantle. 37

Nishitake, T.—Elasticity of Solids at High Pressure and the Earth's Mantle. . . . 47

INDEX OF AUTHORS TO VOLUME XXIX

PAGE

Ogata, H., Itoh, H., Masuda, Y., Takamatsu, K., Kawashima, M., Masaike, A. and **Kumabe, I.**—Numerical Differential Cross Sections of the (p, α) Reactions on Al^{27}, Mn^{55} and Co^{59}. 267

Sasaki, M. (see **Hashi, T., Hirai, A., Sasaki, M.** and **Kawai, T.**) 205

Takamatsu, K. (see **Nakamura, T., Fukunaga, K., Takamatsu, K.** and **Yasumi, S.**) 141

Takamatsu, K. (see **Ogata, H., Itoh, H., Masuda, Y., Takamatsu, K., Kawashima, M., Masaike, A.** and **Kumabe, I.**) 267

Takemoto, S.—Ferromagnetic Resonance in Ni-Cd Ferrite System at Microwave Frequencies. 153

Tanaka, S.—Electron Density Measurement by Microwave Interferometer. 353

Tanaka, S.—Absorption at Electron Cyclotron Resonance in Slightly Ionized Gases (I) 36

Tanaka, S.—Absorption at Electron Cyclotron Resonance in Slightly Ionized Gases (II) 371

Tanaka, S.—Absorption at Electron Cyclotron Resonance in Slightly Ionized Gases (III) 381

Tanaka, S.—Microwave Conductivity of Bounded Plasma. 395

Toba, Y.—Drop Production by Bursting of Air Bubbles on the Sea Surface (III). Study by Use of a Wind Flume. 313

Tomotika, T.—On the Influence of Oxygen Gas upon the Optical Absorption Bands of Evaporated Barium Oxides in the Ultraviolet Region. 75

Yada, B. (see **Hattori, A.**). 107

Yamano, M.—Precise Measurement of Frequency Shift of Ammonia Inversion Spectrum. 57

Yamano, M.—Center Frequency of Ammonia Inversion Spectrum in Low Pressure Region. 67

Yasumi, S. (**Nakamura, T., Fukunaga, K., Takamatsu, K.,** and **Yasumi, S.**) . . 141

Yuhara, K.—Hydrological Study of Atami Hot Springs. 283

CONTENTS

Temperature Dependence of Spin Lattice Relaxation Time of Cl^{35} in Pure Quadrupole Resonance.

By *Akira Hirai* 257

Numerical Differential Cross Section of the (p, α) Reactions on Al^{27}, Mn^{55} and Co^{59}.

By *Hiroshi Ogata, Hidehiko Itoh, Yoshiko Masuda, Kunio Takamatsu, Maumi Kawashima, Akira Masaike* and *Isao Kumabe* 267

Hydrological Study of Atami Hot Springs.

By *Kōzō Yuhara* 283

Drop Production by Bursting of Air Bubbles on the Sea Surface (III). Study by use of a Wind Flume.

By *Yoshiaki Toba* 313

NMR Pulse Apparatus and its Application to the Investigation of Internal Motion of High Polymer (Poly-propylene).

By *Akira Hirai* and *Takao Kawai* 345

Electron Density Measurement by Microwave Interferometer.

By *Shigetoshi Tanaka* 353

Absorption at Electron Cyclotron Resonance in Slightly Ionized Gases (I).

By *Shigetoshi Tanaka* 361

Absorption at Electron Cyclotron Resonance in Slightly Ionized Gases (II).

By *Shigetoshi Tanaka* 371

Absorption at Electron Cyclotron Resonance in Slightly Ionized Gases (III).

By *Shigetoshi Tanaka* 381

Microwave Conductivity of Bounded Plasma.

By *Shigetoshi Tanaka* 395

Printed by NIPPON INSATSU SHUPPAN

Fukushima, Osaka